TURUN
YLIOPISTO
UNIVERSITY
OF TURKU

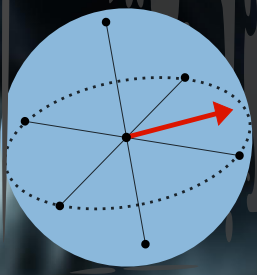

DECOHERENCE AND RESERVOIR ENGINEERING IN LINEAR OPTICAL SYSTEMS

Olli Siltanen

TURUN YLIOPISTON JULKAISUJA – ANNALES UNIVERSITATIS TURKUENSIS
SARJA – SER. AI OSA – TOM. 692 | ASTRONOMICA – CHEMICA – PHYSICA – MATHEMATICA | TURKU 2023

TURUN
YLIOPISTO
UNIVERSITY
OF TURKU

DECOHERENCE AND RESERVOIR ENGINEERING IN LINEAR OPTICAL SYSTEMS

Olli Siltanen

TURUN YLIOPISTON JULKAISUJA – ANNALES UNIVERSITATIS TURKUENSIS
SARJA – SER. AI OSA – TOM. 692 | ASTRONOMICA – CHEMICA – PHYSICA – MATHEMATICA | TURKU 2023

University of Turku

Faculty of Science
Department of Physics and Astronomy
Theoretical physics
Doctoral Programme in Exact Sciences (EXACTUS)

Supervised by

Professor Jyrki Piilo
Department of Physics and Astronomy
University of Turku
Finland

Docent Tom Kuusela
Department of Physics and Astronomy
University of Turku
Finland

Reviewed by

Associate Professor Bassano Vacchini
Dipartimento di Fisica Aldo Pontremoli
Università degli Studi di Milano
Italy

Professor Gunnar Björk
Department of Applied Physics
KTH Royal Institute of Technology
Sweden

Opponent

Doctor Rosario Lo Franco
Dipartimento di Ingegneria
Università degli Studi di Palermo
Italy

ISBN 978-951-29-9281-2 (PRINT)
ISBN 978-951-29-9282-9 (PDF)
ISSN 0082-7002 (PRINT)
ISSN 2343-3175 (ONLINE)
Painosalama, Turku, Finland, 2023

To my Family and Teachers.

UNIVERSITY OF TURKU
Faculty of Science
Department of Physics and Astronomy
Theoretical physics
SILTANEN, OLLI: Decoherence and reservoir engineering in linear optical systems
Doctoral dissertation, 173 pp.
Doctoral Programme in Exact Sciences (EXACTUS)
April 2023

ABSTRACT

Realistic quantum systems interact with their environment and, as a consequence, may lose their quantum properties. This phenomenon is known as decoherence, and it keeps the many oddities of quantum mechanics at the level of elementary particles. But while doing so, decoherence constitutes one of the biggest hindrances to efficient technologies fueled by quantum mechanics. Hence, it is essential to understand the different mechanisms of decoherence and how to control them.

Recently, reservoir engineering, i.e., manipulating the environmental degrees of freedom and their initial correlations, has attracted a lot of attention as a means to control decoherence. Reservoir engineering allows, e.g., to restore information previously leaked into environment back to open quantum systems—a phenomenon often associated with memory and non-Markovianity.

In this Thesis, we study decoherence and reservoir engineering in the context of linear optical systems, where the polarization degree of freedom of single photons is the open quantum system. We begin with a short introduction to the very basics of quantum theory, from which we gradually proceed to the dynamics of open quantum systems.

The rest of the Thesis is dedicated to the main results of Publications **I**–**VII**. We derive the decoherence functions of a biphoton system and show how to control them independently of each other. Using the same methods, we can even reverse the direction of decoherence. This allows us to realize quantum teleportation without the resource qubits being entangled, which we demonstrate also experimentally.

We also consider decoherence occurring in interferometric setups, revealing the interesting effects of which-path-information in Mach-Zehnder interference and photon bunching in Hong-Ou-Mandel interference. Monitoring the open-system dynamics in these setups allows us to estimate different parameters outside the interferometers' more common working region. As for the interferometric region, we present numerical results implying the possibility of breaking the so-called quantum Cramér-Rao bound, a fundamental lower bound for the sensitivity of parameter estimation.

Finally, we consider parameter estimation from the opposite point of view, i.e., when the decoherence model is not known and we cannot monitor it. We implement our alternative protocol in two experiments and apply the results in snapshot verification of non-Markovianity—a task typically requiring monitoring the open-system dynamics.

TURUN YLIOPISTO
Matemaattisluonnontieteellinen tiedekunta
Fysiikan ja tähtitieteen laitos
Teoreettinen fysiikka
SILTANEN, OLLI: Decoherence and reservoir engineering in linear optical systems
Väitöskirja, 173 s.
Eksaktien tieteiden tohtoriohjelma (EXACTUS)
Huhtikuu 2023

TIIVISTELMÄ

Realistiset kvanttisysteemit vuorovaikuttavat ympäristönsä kanssa, minkä seurauksena ne voivat menettää kvanttiominaisuutensa. Tämä ilmiö tunnetaan dekoherenssina, ja se rajaa kvanttimekaniikan kummallisuudet alkeishiukkasten tasolle. Samaan aikaan dekoherenssi kuitenkin muodostaa yhden suurimmista haitoista hyödyllisille kvanttiteknologioille. Tästä syystä on erittäin tärkeää ymmärtää erilaisia dekoherenssimalleja ja kuinka hallita niitä.

Viime aikoina huomiota herättänyt reservimuuntelu on yksi tapa hallita dekoherenssia. Reservimuuntelulla tarkoitetaan ympäristön vapausasteiden ja niiden korrelaatioiden manipuloimista. Kyseisen tekniikan avulla voidaan muun muassa palauttaa ympäristöön vuotanutta informaatiota takaisin avoimiin kvanttisysteemeihin. Tämä ilmiö yhdistetään usein avointen kvanttisysteemien muistiin ja niiden dynamiikan epämarkovisuuteen.

Tässä väitöskirjassa tutkitaan dekoherenssia ja reservimuuntelua lineaarisen optiikan viitekehyksessä. Tässä yhteydessä yksittäisten fotonien polarisaatiovapausaste muodostaa avoimen kvanttisysteemin. Aloitamme lyhyellä johdatuksella kvanttimekaniikan perusteisiin ja siirrymme vähitellen avointen kvanttisysteemien dynamiikkaan.

Loput väitöskirjasta perustuu tieteellisiin alkuperäisjulkaisuihin **I**–**VII**. Johdamme kahden fotonin dekoherenssifunktiot ja osoitamme kuinka hallita näitä toisistaan riippumatta. Samoja menetelmiä soveltamalla kykenemme jopa kääntämään dekoherenssin suunnan. Tämä sallii kvanttiteleportaation ilman kietoutunutta kubittiparia, minkä osoitamme myös kokeellisesti.

Tutkimme myös interferometreissä tapahtuvaa dekoherenssia kiinnittäen erityishuomiota fotonin reittitietoon Mach-Zehnder-interferometrissä ja fotonien ryhmittymiseen Hong-Ou-Mandel-interferometrissä. Monitoroimalla polarisaation käyttäytymistä voimme estimoida erilaisia parametreja näiden interferometrien tavanomaisen toiminta-alueen ulkopuolella. Interferenssialueella esitämme puolestaan numeerisia tuloksia, jotka viittaavat mahdollisuuteen rikkoa niin sanottu kvantti-Cramér-Rao-raja, vastaavanlaisiin arviointitehtäviin liittyvä herkkyysalaraja.

Lopuksi tutkimme tällaisia dekoherenssiin perustuvia parametrien arviointitehtäviä vastakkaisesta näkökulmasta, eli kun dekoherenssimalli ei ole tunnettu, eikä sitä voi monitoroida. Implementoimme vaihtoehtoisen arviointiprotokollamme kahdessa kokeessa ja sovellamme tuloksiamme epämarkovisuuden todentamisessa yhtenä ajan-

hetkenä. Tyypillisesti tämä tehtävä vaatisi nimenomaan dynamiikan monitorointia.

Acknowledgements

Postgraduate studies often resemble the time evolution of an open quantum system. If you are not careful enough, they might be affected by the noise coming from your environment—an environment consisting of colleagues, friends, and family. But unlike with delicate quantum devices, here the environmental interactions turn out to be *vital*; This Thesis owes everything to such "noise"!

First, I would like to express my humblest gratitude to Gunnar Björk and Bassano Vacchini for reviewing this Thesis and Rosario Lo Franco, my esteemed opponent. And thank you Kalle-Antti, my research director, for all your guidance. This work was funded by the Magnus Ehrnrooth Foundation and the University of Turku Graduate School, to which I am sincerely grateful. I would also like to thank Ailea for helping me in the very beginning.

I would not have been able to finish, let alone begin, my PhD studies without the help of my extraordinary supervisors. Thank you, Jyrki, for sharing your wisdom on open quantum systems and quantum information, as well as all the sparring. And thank you, Tom, for introducing me to the luminous (yet often so dark) world of quantum optics all those years ago. Thank you, both, for believing in me and pushing me forward. I have learned so much from you; I can only hope that the information flow between us has been at least somewhat bidirectional.

A theoretical physicist's predictions are only as good as the experimental results. Therefore, I'm in huge debt to Tom, again, and the experimental group at USTC, Hefei. I especially appreciate the favorable results. Thank you, Zhao-Di and Chuan-Feng, also for the hospitality during our visit.

Whether it was the captivating lectures, scientific collaboration, or just briefly crossing paths, I thank all the people I have been fortunate enough to meet during my studies. So thank you Iiro, Juha-Pekka, Teiko, Sabrina, Subhashish, Robert, the people at Trani, and all the students that had the patience to sit through *my* lectures.

I collectively thank all my friends and colleagues both *of* and *off* the Corridor. Be it a coffee break, lunch, pub quiz, a round of Rocket League, training, vlog, a training vlog, or a competition trip I could share with you, I truly feel privileged having been surrounded by people like you. A special thank is in place to Henri. I like to consider you my third supervisor, looking after my well-being and teaching that the "p" in "physics" stands for "pun". Exactly... Moreover, it was a great pleasure working with you, and I look forward to future collaboration.

Having a doctor mother and an engineer father, I guess I was destined to become a doctor of (reservoir) engineering. But on a more serious note, despite the risk of sounding cheesy, one could not ask for better parents. This Thesis owes its existence to you, Mom and Dad, as do I.

Aapo, Johannes, Jaakko, Akseli, and Oskari. I am proud to call you my brothers. Having grown up with you has taught me a number of things, one of which seems to puzzle many, that is, the ability to concentrate (or *appear concentrated*) anywhere, even in the notorious "noisy room" at the Corridor. So thank you for all the years and all the support.

Finally, I would like to thank my wife Tanja for the constant support I have been blessed to enjoy, through thick and thin, and our daughters Venla, Elli, and "Alice" for bringing immeasurable joy to our lives.

25.4.2023
Olli Siltanen

Contents

List of papers

This dissertation is based on the following original publications, which are referred to in the text by their Roman numerals:

I **Distributing memory effects in an open two-qubit system**,
O. Siltanen, T. Kuusela, and J. Piilo, Phys. Rev. A **102**, 022225 (2020).

II **Efficient quantum teleportation under noise with hybrid entanglement and reverse decoherence**,
Z.-D. Liu, *O. Siltanen*, T. Kuusela, R.-H. Miao, C.-X. Ning, C.-F. Li, G.-C. Guo, and J. Piilo, arXiv:2210.14935 (2022).

III **Interferometric approach to open quantum systems and non-Markovian dynamics**,
O. Siltanen, T. Kuusela, and J. Piilo, Phys. Rev. A **103**, 032223 (2021).

IV **Breaking the quantum Cramér-Rao bound with non-Markovian memory effects**,
O. Siltanen, arXiv:2211.05142 (2022).

V **Engineering of Hong-Ou-Mandel interference with effective noise**,
O. Siltanen, T. Kuusela, and J. Piilo, Phys. Rev. A **104**, 042201 (2021).

VI **Experimental quantum probing measurements with no knowledge of the system-probe interaction**,
H. Lyyra, *O. Siltanen*, J. Piilo, S. Banerjee, and T. Kuusela, Phys. Rev. A **102**, 022232 (2020).

VII **Experimental snapshot verification of non-Markovianity by quantum probing of convex coefficients**,
H. Lyyra, *O. Siltanen*, J. Piilo, S. Banerjee, and T. Kuusela, Phys. Rev. A **106**, 032603 (2022).

Other published material

This is a list of the publications produced which have not been chosen as a part of this doctoral thesis:

- **Entanglement protection via periodic environment resetting in continuous-time quantum-dynamical processes**,
  T. Bullock, F. Cosco, M. Haddara, S. Hamedani Raja, O. Kerppo, L. Leppäjärvi, *O. Siltanen*, N. W. Talarico, A. De Pasquale, V. Giovannetti, and S. Maniscalco, Phys. Rev. A **98**, 042301 (2018).

1 Introduction

Quantum mechanics describes Nature at its most fundamental level—at the level of elementary particles such as atoms, electrons, and photons, where the classical laws of physics describing macroscopic phenomena become insufficient. Quantum mechanics is inherently probabilistic, which shows, e.g., as quantum systems being able to occupy multiple states at the same time. This is known as the superposition principle. Another oddity of quantum mechanics is the concept of quantum entanglement: Measurement results in the Andromeda Galaxy can instantaneously affect measurement results in Buenos Aires. Einstein famously described entanglement as "spooky action at a distance".

Despite its random nature, the quirks of quantum theory lay the foundation for numerous applications including lasers, transistors, and magnetic resonance imaging (MRI) [1]. Furthermore, encoding information to superposition states of "0" and "1", i.e., qubits, promises exponential speed-up over classical computation, accelerating crucial tasks such as drug development in the future [2]. But it is not just the man-made applications that get to enjoy the fruits of quantum mechanics. For example, it has been proposed that photosynthesis is based on superposition [3].

Now, two questions should arise: How come quantum mechanics only holds at the microscopic level? Why do we not see the bizarre quantum phenomena in larger scales, e.g., cars simultaneously turning left and right? Cars are, after all, made of the very atoms governed by the rules of quantum theory. Secondly, although quantum supremacy has been experimentally demonstrated [4], where are the commercial quantum computers solving actually meaningful problems? The theory of open quantum systems and decoherence provide one explanation to both questions.

As quantum systems are exposed to their surroundings, they tend to lose their quantum properties, i.e., experience decoherence [5]. Such systems are called open quantum systems [6; 7; 8]. Understanding open quantum systems and decoherence is important for both fundamental and technological reasons; While decoherence keeps the quantum mechanical phenomena at the microscopic level, controlling it—and in the best-case scenario, preventing or canceling it—is essential, e.g., for useful, large-scale quantum computers to work [9].

The problem with decoherence can be approached from two complementary viewpoints. On one hand, there is resisting it. Some popular methods to fight decoherence include dynamical decoupling [10; 11; 12], decoherence-free subspaces

(DFSs) [13; 14; 15], delayed quantum feedback [16; 17; 18], quantum error-correcting codes [19; 20; 21], indefinite causal orders [22; 23], and reservoir engineering [24; 25; 26; 27]. Reservoir engineering essentially means modifying the state of the environment prior to the system-environment interaction [28]. Such modifications can lead to partial revivals of the open system's quantum properties, which is often associated with memory effects—or "non-Markovianity" [29; 30; 31; 32; 33]. While all of these methods are highly developed, even more efficient ones are still needed. Could we, for example, reverse decoherence?

On the other hand, we could embrace decoherence and study the benefits of it. It seems that this viewpoint is rarely explored. Taking such a point of view, it becomes useful being able to controllably produce, or emulate, decoherence. Linear optics provides the perfect platform for just that.

In linear optics, the polarization of photons is often interpreted as the open system, while the same photons' frequency serves as the environment [34; 35; 36; 37; 38; 39; 40; 41; 42; 43; 44]. The two can be coupled in a birefringent medium, where different polarization components propagate at different velocities. Consequently, the polarization degree of freedom experiences special kind of decoherence, i.e., dephasing. Dephasing is responsible for the pure quantum-to-classical transition naturally appearing in multiple physical systems, e.g., qubits disturbed by thermal fluctuations [45]. Previous works related to linear optical open-system simulators include the realization of DFSs [13], controlled transition between Markovian and non-Markovian dynamics [46], full control of single-photon dephasing [47], quantum teleportation with nonlocal memory effects [48; 49], and superdense coding [50; 51]. With linear optics, one can also simulate open-system dynamics by incoherently mixing different unitary dynamics caused by wave plates [52; 53; 54; 55; 56], and when combined with beam splitters, form versatile collision models [57; 58; 59]. However, these methods are not in the focal point of this Thesis.

This Thesis is a comprehensive study on the aforedescribed polarization-frequency model. We go beyond prior works by considering more photons, interferometric effects, and quantum probing. In Chapters 2 and 3, we go through the theoretical background of quantum mechanics and open quantum systems necessary to understand the rest of the Thesis. We pay special attention to states and entanglement; The quantum-to-classical transition of open quantum systems follows directly from system-environment entanglement. We will also cover some experimental aspects concerning this Thesis, describe the single-photon dephasing model in full detail, and present two widely used definitions of quantum non-Markovianity.

The main results of this Thesis, originally reported in Publications **I**–**VII**, are presented in Chapters 4–6. We begin Chapter 4 by deriving the dephasing model of two polarization qubits. Then, we show how to control biphoton dephasing with initial system-environment correlations, extending the results of Ref. [47]. Our technique allows to select the open-system subspaces experiencing non-Markovian memory

effects and completely reverse the direction of dephasing; Memory partitions and reverse decoherence were originally introduced in Publications **I** and **II**, respectively. We end Chapter 4 by describing noisy quantum teleportation with reverse decoherence, which was also experimentally demonstrated in Publication **II**.

Chapter 5 is based on Publications **III**–**V**. Here, we expand the environment of polarization by considering the photons' path degree of freedom as well, introducing the concept of open system interference. We concentrate on the interferometric effects often overlooked in similar setups (see, e.g., Refs. [52; 56]). As two paradigmatic examples, we consider the Mach-Zehnder (MZ [60; 61; 62]) and Hong-Ou-Mandel (HOM [63; 64]) interferometers. We solve the open-system dynamics in both cases, conditioned on which-path-information with the MZ interferometer and photon bunching with the HOM interferometer. In the first case, we briefly discuss non-Markovian memory effects with completely positive and trace-nonincreasing (CPTNI) maps. In the latter, we also solve the single-qubit dynamics, which allows us to outline some interesting, local applications, i.e., applications free of comparing photon counts. The open system MZ interferometer was originally introduced in Publication **III** and the open system HOM interferometer in Publication **V**.

In Chapter 5, we shift our focus from controlling the open-system dynamics to using it, especially in parameter estimation. We show how decoherence can give estimates for parameters outside the interferometers' more common working regions. With the open system MZ interferometer, we also discuss the possibility of breaking the quantum Cramér-Rao bound (QCRB [65; 66]). The simulation results supporting this were originally reported in Publication **IV**.

While the two open system interferometers introduced in Chapter 5 give rise to novel parameter estimation methods, they are based on the interaction model being known and highly controllable—both being quite drastic assumptions outside the linear optical framework. In practice, this shows as sequential state tomographies performed at different lengths of the birefringent medium. In Chapter 6, we take the opposite point of view and ponder the question: With an unknown interaction model at an unknown time, can we deduce something about a parameter of interest? Or in layman's terms, can we trust the readout of a measurement apparatus without knowing how the readout was obtained? The answer is, perhaps counterintuitively, yes. Chapter 6 is based on the generalized data processing inequalities originally introduced in Refs. [67; 68] and later applied in Publications **VI** and **VII**.

We conclude this Thesis in Chapter 7 by summarizing the main results and discussing possible directions of future research.

2 Rudiments of quantum theory

Let us begin by introducing some key concepts of quantum theory. We go through quantum states, entanglement, and measurements, paying special attention to two-level systems and their physical manifestations. Furthermore, we briefly discuss some aspects related to single-photon experiments and end by characterizing closed quantum systems and their dynamics. With all the basic definitions, we refer to [69].

2.1 States and qubits

In quantum mechanics, the measurement statistics of physical systems are described by *states*, usually denoted by ρ. Mathematically, the state of a d-dimensional system can be written as a $d \times d$-dimensional *density matrix*, $\rho = \sum_{j,k=0}^{d-1} \rho_{jk} |j\rangle\langle k|$, where the vectors $|j\rangle$ form an orthonormal basis for the *Hilbert space* $\mathcal{H}_d$. Hilbert spaces are complex-vector spaces equipped with the inner product $\langle\cdot|\cdot\rangle$ and norm $\|\cdot\| := \sqrt{\langle\cdot|\cdot\rangle}$, and orthonormal vectors satisfy $\langle j|k\rangle = \delta_{j,k}$. Typically, one associates the "ket-vector" $|0\rangle$ with the column vector $(1, 0, 0, ...)^T$, $|1\rangle$ with $(0, 1, 0, ...)^T$, and so on, whereas the "bra-vectors" $\langle j|$ are the Hermitian conjugates of $|j\rangle$.

The diagonal elements of the density matrix, $\langle j|\rho|j\rangle$, are the probabilities for an experimentalist working in the same basis to obtain outcome j, when the system of interest is in the state ρ. They (and the eigenvalues of the density matrix) are therefore nonnegative real numbers satisfying the normalization condition $\mathrm{tr}[\rho] = \sum_{j=0}^{d-1} \langle j|\rho|j\rangle = \sum_{j=0}^{d-1} \rho_{jj} = 1$. The sum of a matrix's diagonal elements is called its *trace*.

There is nothing particulary "quantum" here. We could, for example, write the density matrix for a fair coin toss as

$$\rho_{\text{coin}} = \begin{pmatrix} 1/2 & 0 \\ 0 & 1/2 \end{pmatrix} \tag{2.1}$$

with the diagonal elements giving the probabilities of heads and tails. However, the off-diagonal elements $\langle j|\rho|k\rangle$, $j \neq k$, need not be zero in general. We call these elements the *coherences* of a system, and they describe how "quantum" our system of interest is, e.g., if the system can be simultaneously in multiple states. Unlike the probabilities, the coherences can be negative and even complex-valued, but their absolute values are bounded from above so that $|\rho_{jk}|^2 \leq \rho_{jj}\rho_{kk}$. Furthermore, we

require that $\rho = \rho^\dagger$, meaning that $\rho_{jk} = \rho^*_{kj}$. In short, a valid density matrix is Hermitian, positive, and of trace one.

One could naïvely argue that, until observing heads or tails, the coin is in both states at the same time, and *all* the entries of ρ_{coin} should be 1/2 of magnitude. However, if we knew all the initial conditions of the coin toss, we could *in principle* determine if the result was heads or tails with certainty. Then, taking the momentary liberty to describe classical states with Hilbert-space vectors, we could actually describe a *single* coin toss with either $\rho_{\text{heads}} = |0\rangle\langle 0|$ or $\rho_{\text{tails}} = |1\rangle\langle 1|$. Hence, as a balanced mixture of ρ_{heads} and ρ_{tails}, Eq. (2.1) actually describes multiple tosses of an identical, fair coin, i.e., measurement statistics. Describing a single coin toss with Eq. (2.1) would just reflect our ignorance of the initial conditions[1].

So, the coherences determine if the system behaves in a *genuinely* probabilistic manner; They differ from zero if we have no chance, even in principle, to perfectly predict the measurement outcome. With maximum coherences, the state of a system can be written in the vector form $|\psi\rangle = \sum_{j=0}^{d-1} C_j|j\rangle$, and we talk about a *pure* state. If the state cannot be written as a vector, it is *mixed*. Moreover, if more than one *probability amplitude* C_j differ from zero, we say that the system is in *superposition* (in the $\{|j\rangle\}$-basis). The corresponding density matrix simply reads

$$\rho = |\psi\rangle\langle\psi| = \begin{pmatrix} |C_0|^2 & C_0C_1^* & \dots & C_0C_{d-1}^* \\ C_0^*C_1 & |C_1|^2 & \dots & C_1C_{d-1}^* \\ \vdots & \vdots & \ddots & \vdots \\ C_0^*C_{d-1} & C_1^*C_{d-1} & \dots & |C_{d-1}|^2 \end{pmatrix}. \tag{2.2}$$

A photon in a beam splitter serves as a paradigmatic example of the genuine probabilistic nature of quantum theory, the superposition principle, and *interference*. Let us describe the initial path of a single photon with the state $|\psi\rangle = (1,0)^T$ and a balanced, lossless beam splitter with the *Hadamard operator* $H = \frac{1}{\sqrt{2}}\begin{pmatrix} 1 & 1 \\ 1 & -1 \end{pmatrix}$. The action of the beam splitter on the photon reads $H|\psi\rangle = \frac{1}{\sqrt{2}}(1,1)^T$; An experimentalist can expect to find the photon on the transmitted or reflected path with equal probability. Nothing peculiar here, but now we go as far as to claim that, until detected, the photon *both* passes through *and* reflects from the beam splitter. The claim contradicts common sense, but the following argument supports it.

Say, the two paths enter *another* beam splitter from different sides. The final state of the photon is then $HH|\psi\rangle = |\psi\rangle$, i.e, the photon has returned to its initial path. If the photon had *either* passed through *or* reflected from both of the beam splitters, it would have ended up on either path with equal probability. But experimental evidence says otherwise. On the final path, the photon experiences constructive in-

[1] Actually, one should use *probability vectors* $(p_0, p_1, ..., p_{d-1})$ to describe classical states, but the density matrix ρ_{coin} still provides the true statistics of a fair coin.

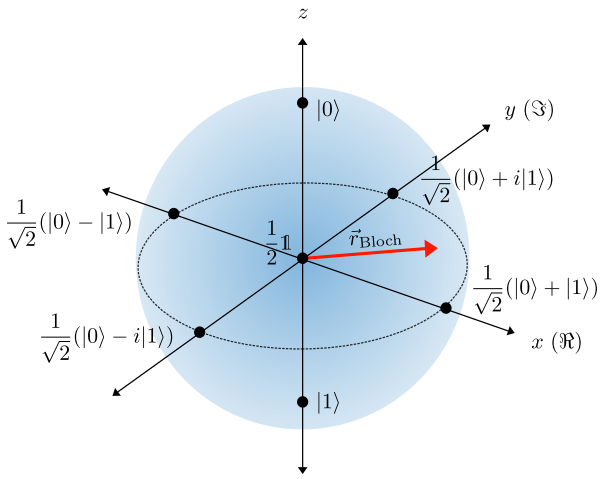

Figure 2.1. The Bloch ball. Pure states live on the ball's surface, the *Bloch sphere*. In particular, balanced superpositions lie on the ball's equator, i.e., the unit circle of the complex plane defined by the x- and y-axises. States on the z-axis have classical counterparts, since they have zero coherences. Thus, when given just a probability distribution in a fixed basis, one cannot distinguish between quantum and classical. The origin of the Bloch ball represents the maximally mixed state. An arbitrary qubit state is fully determined by $\vec{r}_{\text{Bloch}}$.

terference *with itself*, and on the other, destructive interference. This would not be possible, had the photon not traveled both paths.

The Hadamard operator H used above belongs to a special class of quantum operators called the *unitary operators*, and we will come back to such operators shortly. Furthermore, the setup consisting of two beam splitters is known as the *Mach-Zehnder (MZ) interferometer* [60; 61], and it will play a central role in Chapter 5.

The systems we have considered so far are two-level systems—a coin with the options heads/tails and a photon with the options transmit/reflect. The coin is an example of a classical bit, and the photon is an example of a quantum bit—or *qubit*. For qubits, there exists a particularly nice geometric representation, namely, the *Bloch representation*. Without loss of generality, we can write any qubit state as

$$\rho = \frac{1}{2}\begin{pmatrix} 1+z & x-iy \\ x+iy & 1-z \end{pmatrix}. \tag{2.3}$$

Since the eigenvalues of ρ need to be in the interval $[0, 1]$, we arrive at $\|\vec{r}_{\text{Bloch}}\|^2 \leq 1$, where $\vec{r}_{\text{Bloch}} = (x, y, z)$ is the *Bloch vector* and $\|\cdot\|$ is the Euclidean norm. With its norm being bounded, the Bloch vector determines a ball of unit radius, i.e., the *Bloch ball* (see Fig. 2.1). The pure qubit states lay on the surface of the Bloch ball, i.e., $\|\vec{r}_{\text{Bloch}}\| = 1$, and the smaller the norm, the more mixed (or classical) the state is.

The *purity* $\mathcal{P}$ provides a convenient way to quantify the degree of mixedness of d-dimensional systems—not only qubits—and it is given by $\mathcal{P}(\rho) = \mathrm{tr}[\rho^2]$ with 1 meaning a pure state and 1/d the fully mixed state, $\frac{1}{d}\mathbb{1}$. In the case of a qubit, we have $\mathcal{P}(\rho) = (1 + \|\vec{r}_{\mathrm{Bloch}}\|^2)/2$. However, it is important to notice that the purity does not necessarily tell anything about the coherences. For example, the closer a pure qubit state is to the poles of the Bloch ball, $|0\rangle$ or $|1\rangle$, the smaller its coherences are in the $\{|0\rangle, |1\rangle\}$-basis, i.e., the *computational basis*, which we will focus on in the rest of the Thesis. But why is the computational basis of special interest? After all, the states $|0\rangle$ and $|1\rangle$ have *maximum* coherences in all the bases spanned by orthogonal vectors in the Bloch ball's xy-plane.

In quantum information, the computational basis turns out to be very natural choice. Here, for example, the superposition principle allows one to simultaneously encode all the 2^N permutations of N bits (i.e., 0s and 1s) into the same number of qubits. This enables *parallel computing* with exponential speed-up over classical algorithms [70]. Furthermore, in many quantum algorithms the state preparation and final measurement occur in the same basis, which means that other bases can often be disregarded.

In addition to fast quantum algorithms, coherences fuel many other quantum information protocols, e.g., the famous *BB84 quantum key distribution protocol* [71]. *Nonlocal* coherences, on the other hand, give rise to *quantum entanglement*, the basis of high-sensitive parameter estimation [72], *superdense coding* [50; 51], and *quantum teleportation* [73], just to name a few examples. Quantum teleportation is handled in Chapter 4. Before that, we need to take a closer look at bipartite systems and entanglement.

2.2 Bipartite systems and entanglement

If we have two quantum systems—often shared by two parties called Alice and Bob—we may describe them with a joint state ρ_{AB}. The corresponding Hilbert space is $\mathcal{H}_A \otimes \mathcal{H}_B$. If the systems are uncorrelated, the state factorizes and it can be written in the tensor product form $\rho_{AB} = \rho_A \otimes \rho_B$; The measurement result of Alice does not affect the measurement result of Bob and vice versa. A state ρ_{AB} that cannot be written as a convex combination of product states $\rho_A \otimes \rho_B$ is *entangled*. Hence, an entangled *pure* state cannot be written in the form $|\psi_{AB}\rangle = \sum_{j_A} C_{j_A} |j_A\rangle \otimes \sum_{j_B} C_{j_B} |j_B\rangle$.

Entangled quantum states exhibit strong nonlocal correlations, meaning that whatever happens on Alice's side *immediately* affects what happens on Bob's side, regardless of their distance. Let us illustrate this more clearly with pure *polarization qubits* $|\psi\rangle = C_H|H\rangle + C_V|V\rangle$, where C_H and C_V are the probability amplitudes for a single photon to be horizontally and vertically polarized, respectively[2]. Any

[2] H is used for both the Hadamard operator and horizontal polarization, but its meaning should be clear from the context.

pure, bipartite polarization state can be written in the form $|\psi_{AB}\rangle = C_{H_AH_B}|H_A\rangle \otimes |H_B\rangle + C_{H_AV_B}|H_A\rangle \otimes |V_B\rangle + C_{V_AH_B}|V_A\rangle \otimes |H_B\rangle + C_{V_AV_B}|V_A\rangle \otimes |V_B\rangle$, where $C_{\lambda_A\lambda_B}$ is the probability amplitude for Alice and Bob's photons to be λ_A- and λ_B-polarized, respectively ($\lambda_A, \lambda_B = H, V$). If $|\psi_{AB}\rangle$ was uncorrelated (i.e., a product state), we would have $C_{\lambda_A\lambda_B} = C_{\lambda_A}C_{\lambda_B}$, and we could write $|\psi_{AB}\rangle = (C_{H_A}|H_A\rangle + C_{V_A}|V_A\rangle) \otimes (C_{H_B}|H_B\rangle + C_{V_B}|V_B\rangle)$.

By denoting $C_{H_AV_B} = C_{V_AH_B} = 1/\sqrt{2}$ and $C_{H_AH_B} = C_{V_AV_B} = 0$, we get the state $|\psi_{AB}\rangle = (|H_A\rangle \otimes |V_B\rangle + |V_A\rangle \otimes |H_B\rangle)/\sqrt{2}$. If we try to write this state as a product state, we need to solve the following system of equations

$$\begin{cases} C_{H_A}C_{V_B} = C_{V_A}C_{H_B} = \frac{1}{\sqrt{2}}, \\ C_{H_A}C_{H_B} = C_{V_A}C_{V_B} = 0. \end{cases} \tag{2.4}$$

Clearly, the system of equations is unsolvable, and we conclude that the state $|\psi_{AB}\rangle = (|H_A\rangle \otimes |V_B\rangle + |V_A\rangle \otimes |H_B\rangle)/\sqrt{2}$ is entangled. If Alice measures the polarization of her photon, she obtains the result H or V with equal probability. However, whichever outcome Alice gets, it immediately determines that of Bob; If Alice detects a horizontally (vertically) polarized photon, she knows that Bob's polarization will be vertical (horizontal) in the same measurement basis. We will deal with measurements soon in more detail.

We sometimes drop the lower indices and the tensor product symbols and simply write $|\psi_{AB}\rangle = (|HV\rangle + |VH\rangle)/\sqrt{2}$. In fact, this state is maximally entangled, and it is typically written as $|\Psi^+\rangle$ and called a *Bell state*. There are four Bell states altogether, and they read [70]

$$\begin{cases} |\Phi^\pm\rangle = \frac{1}{\sqrt{2}}(|HH\rangle \pm |VV\rangle), \\ |\Psi^\pm\rangle = \frac{1}{\sqrt{2}}(|HV\rangle \pm |VH\rangle). \end{cases} \tag{2.5}$$

Of course, the degree of freedom can be whatever, not only polarization.

One might wonder what is so special in the example above. Say, a pair of gloves is distributed to Alice and Bob. If Alice receives a left-handed glove, she immediately knows that Bob's glove is right-handed. However, one must remember that the coherences mean genuine probability that manifests as the physical system being in both states simultaneously. In the case of our example and with the choices $|H\rangle = (1,0)^T$ and $|V\rangle = (0,1)^T$, the density matrix reads

$$\rho_{AB} = |\Psi^+\rangle\langle\Psi^+| = \frac{1}{2}\begin{pmatrix} 0 & 0 & 0 & 0 \\ 0 & 1 & 1 & 0 \\ 0 & 1 & 1 & 0 \\ 0 & 0 & 0 & 0 \end{pmatrix}. \tag{2.6}$$

The entanglement of a bipartite system can be quantified with *concurrence*, which is inversely proportional to the purity of the local, reduced states. With pure states

$\rho_{AB} = |\psi_{AB}\rangle\langle\psi_{AB}|$, the concurrence can be written as [74]

$$\mathcal{C}(\rho_{AB}) = \sqrt{2[1 - \mathcal{P}(\rho_A)]} = \sqrt{2[1 - \mathcal{P}(\rho_B)]}. \tag{2.7}$$

Here, $\rho_{A(B)}$ is Alice's (Bob's) local state, defined as the *partial trace* over Bob's (Alice's) Hilbert space: $\rho_{A(B)} = \mathrm{tr}_{B(A)}[\rho_{AB}] = \sum_{j_{B(A)}} \langle j_{B(A)}|\rho_{AB}|j_{B(A)}\rangle$, where the vectors $|j_{B(A)}\rangle$ form an orthonormal basis for the Hilbert space $\mathcal{H}_{B(A)}$. Partial trace is a frequently used tool in this Thesis. It essentially gives a lower dimensional state, where correlations appearing in the higher-dimensional parent state have been ignored by averaging. For example, taking partial trace of any of the Bell states yields $\rho_A = \rho_B = \frac{1}{2}\mathbb{1}$; For Alice and Bob, the local states ρ_A and ρ_B appear maximally mixed even though the underlying total state is pure and maximally entangled. Note that the coherences in Eq. (2.6) do not appear in the partial traces. In general, the antidiagonal elements of a density matrix are inaccessible by partial trace and called nonlocal coherences.

Entanglement manifesting as mixed reduced states has overarching consequences for the rest of this Thesis.

2.3 Measurements

Measurements lie at the heart of any natural science. In macroscopic theories, measurable quantities are properties of some system of interest alone, existing even if they were not measured—but once measured, the result can be trusted; A measurement event itself did not affect the system, giving a corrupted reading. This is *not* the case with quantum theory. In quantum mechanics, states are disturbed and changed by measurements, and we can only receive partial information of the system [75; 76; 77].

Quantum measurement is an extensively studied field of research (see, e.g., [78; 79]), but here we restrict our attention to *projective measurements*. Projective measurements are described by complete sets of *projections* $\{\Pi_j\}$, where the subindex j refers to the measurement outcome. Projections satisfy $\Pi_j = \Pi_j^\dagger = \Pi_j^2$, and with completeness we mean that the projections sum up to the identity operator, $\sum_j \Pi_j = \mathbb{1}$. One can form such projections, e.g., from all the vectors of an orthonormal basis $\{|j\rangle\}_{j=0}^{d-1}$: $\Pi_j := |j\rangle\langle j| (= \Pi_j^\dagger) \Rightarrow \Pi_j^2 = |j\rangle\langle j|j\rangle\langle j| = |j\rangle\langle j| = \Pi_j$ and $\sum_j |j\rangle\langle j| = \mathbb{1}$. Unitary transformations $U|j\rangle$ form endless other bases, and whichever we choose to work with is called the *measurement basis*.

Let us clarify the physical meaning of projective measurements. Say, a quantum system in the pure state $|\psi\rangle = \sum_{j=0}^{d-1} C_j|j\rangle$ enters a measurement apparatus, and an experimentalist works in the same measurement basis. Then, the projection corresponding to the measurement outcome k is $|k\rangle\langle k|$, and the action of a measurement

leading up to this outcome reads

$$|k\rangle\langle k|\psi\rangle = |k\rangle \sum_{j=0}^{d-1} C_j \langle k|j\rangle \tag{2.8}$$

$$= |k\rangle \sum_{j=0}^{d-1} C_j \delta_{k,j} \tag{2.9}$$

$$= C_k|k\rangle. \tag{2.10}$$

We say that the initial state $|\psi\rangle$ has *collapsed* to $|k\rangle$ with the probability $|C_k|^2$. This is the famous "Copenhagen interpretation" of quantum mechanics [80].

Note that $C_k|k\rangle$ is not, in fact, a proper state, since it is not a unit vector (unless $|C_k| = 1$). In general, the state $\tilde{\rho}$ after a projective measurement reads

$$\tilde{\rho} = \frac{\Pi_j \rho \Pi_j}{\mathrm{tr}[\Pi_j \rho \Pi_j]}. \tag{2.11}$$

These kinds of post-measurement states are used in different parameter estimation methods introduced in Chapter 5. Although they have their advantages, note that $1 - \mathrm{tr}[\Pi_j \rho \Pi_j]$ of the individual resource states go to waste.

Going back to our example, an individual post-measurement state $|k\rangle$ does not tell much about the initial state $|\psi\rangle$. Furthermore, multiple measurements on identically prepared states in the same measurement basis only give the classical probability vector $(|C_0|^2, |C_1|^2, ..., |C_{d-1}|^2)$. In order to access the complex-valued probability amplitudes C_j, one often needs to perform measurements in multiple different bases. The *state tomography* of single-photon polarization illustrates this well [81]. Here, we use the Bloch representation and the notations $|D\rangle = (|H\rangle + |V\rangle)/\sqrt{2}$, $|A\rangle = (|H\rangle - |V\rangle)/\sqrt{2}$, $|R\rangle = (|H\rangle + i|V\rangle)/\sqrt{2}$, and $|L\rangle = (|H\rangle - i|V\rangle)/\sqrt{2}$.

Measurements in the $\{|H\rangle, |V\rangle\}$-basis give us the nonnormalized states $\sqrt{\frac{1+z}{2}}|H\rangle$ and $\sqrt{\frac{1-z}{2}}|V\rangle$, measurements in the $\{|D\rangle, |A\rangle\}$-basis give us the nonnormalized states $\sqrt{\frac{1+x}{2}}|D\rangle$ and $\sqrt{\frac{1-x}{2}}|A\rangle$, while measurements in the $\{|R\rangle, |L\rangle\}$-basis give us the nonnormalized states $\sqrt{\frac{1+y}{2}}|R\rangle$ and $\sqrt{\frac{1-y}{2}}|L\rangle$. In practice, a measurement corresponding to the projection Π_j can be realized by guiding single photons through a combination of a quarter-wave plate (QWP), a half-wave plate (HWP), and a polarizer. This combination acts as a filter that lets P_j of the incoming photons through. We won't go into the details of wave plates, but the angles of their fast axes with respect to the horizontal axis—as well as the polarizer's axis of transmission—are given in Table 2.1.

Now, by comparing the photon counts obtained from the different wave-plate configurations, we get the probabilities P_j, and we can calculate the components of

Table 2.1. Projections, wave-plate angles, and the final probabilities related to single-photon polarization tomography.

$\boldsymbol{\Pi_j}$	$\boldsymbol{\theta}_{\text{QWP}}(^\circ)$	$\boldsymbol{\theta}_{\text{HWP}}(^\circ)$	$\boldsymbol{\theta}_{\text{Polarizer}}(^\circ)$	$\boldsymbol{P_j}$
$\|H\rangle\langle H\|$	0	0	0	$(1+z)/2$
$\|V\rangle\langle V\|$	0	0	90	$(1-z)/2$
$\|D\rangle\langle D\|$	0	22.5	0	$(1+x)/2$
$\|A\rangle\langle A\|$	0	22.5	90	$(1-x)/2$
$\|R\rangle\langle R\|$	45	0	0	$(1+y)/2$
$\|L\rangle\langle L\|$	45	0	90	$(1-y)/2$

the Bloch vector:

$$\begin{cases} x = P_D - P_A, \\ y = P_R - P_L, \\ z = P_H - P_V. \end{cases} \tag{2.12}$$

In the context of polarization, the Bloch-vector components are also called the *Stokes parameters* S_j, and we can write the qubit state alternatively as

$$\rho = \frac{1}{2}\sum_{j=0}^{3} S_j \sigma_j. \tag{2.13}$$

Here, $S_0 = 1$, $S_1 = x$, $S_2 = y$, $S_3 = z$, $\sigma_0 = \mathbb{1}$, and σ_j (with $j = 1, 2, 3$) are the *Pauli matrices*

$$\sigma_1 \equiv \sigma_x = \begin{pmatrix} 0 & 1 \\ 1 & 0 \end{pmatrix}, \ \sigma_2 \equiv \sigma_y = \begin{pmatrix} 0 & -i \\ i & 0 \end{pmatrix}, \ \sigma_3 \equiv \sigma_z = \begin{pmatrix} 1 & 0 \\ 0 & -1 \end{pmatrix}. \tag{2.14}$$

An arbitrary N-qubit state can be written in terms of the Stokes parameters and Pauli matrices as [82]

$$\rho = \frac{1}{2^N} \sum_{j_1, j_2, \ldots, j_N = 0}^{3} S_{j_1 j_2 \ldots j_N} \sigma_{j_1} \otimes \sigma_{j_2} \otimes \ldots \otimes \sigma_{j_N}. \tag{2.15}$$

With N polarization qubits, we have 4^N Stokes parameters. By definition, $S_{00\ldots0} = 1$. To determine the rest of the parameters, we need 6^N different measurements in the worst-case scenario. Hence, polarization tomography can become quite a tedious task with an increasing number of qubits.

Polarization tomography is something that we will encounter many times in this Thesis. Hence, let us very briefly discuss a few more experimental issues related to it. Photon pairs can be produced with *spontaneous parametric down-conversion (SPDC* [83]*)*. In SPDC, a crystal with high second-order susceptibility $\chi^{(2)}$ [e.g., beta-barium borate (BBO)] is pumped with a strong laser beam. Most of the time, the

pump photons just go through the crystal, but sometimes—due to $\chi^{(2)}$ and vacuum fluctuations—the pump photon (p) is converted into two photons with lower energy. These photons are often called the *signal* (s) and *idler photon* (i).

The conservation of energy dictates that the frequencies of the signal and idler photon need to satisfy $f_s + f_i = f_p$. Similarly, due to the conservation of momentum, the photons need to satisfy the *phase matching condition* $\vec{k}_s + \vec{k}_i = \vec{k}_p$. Furthermore, polarization-entangled photon pairs can be created by collecting the signal and idler photons from the intersections of two light cones exiting the nonlinear crystal.

Polarization tomography is sensitive to background photons. The background photons' influence is typically mitigated by *coincidence counting*. Whichever photon of an N-photon state arrives at a photodetector connected to a coincidence counter first, triggers it to expect the other photons to arrive at their detectors; If all the other $N-1$ photons arrive within a fixed time window, we have a coincidence. Since the background photons rarely cause accidental coincidences, we can trust that the coincidences originate from some system of interest in the state ρ, which we are measuring, and we can safely omit all the other detection events.

The photodetectors themselves can also cause measurement errors. Dark counts and dead time are such examples [84]. Dark counts are accidental detection events caused by thermal fluctuations, and dead time is the time required by a detector to recover after each detection. Thus, photons arriving at a detector during its dead time are not registered. In Chapter 5, we will describe how to utilize dead time in parameter estimation.

2.4 Unitary dynamics and closed systems

Projections operate in a probabilistic manner. Π_j either projects a (possibly mixed) state ρ into a corresponding pure state with the probability $\mathrm{tr}[\Pi_j \rho \Pi_j]$ or destroys it with the probability $1 - \mathrm{tr}[\Pi_j \rho \Pi_j]$. On the contrary, the Hadamard operator H, HWP, and QWP are examples of unitary operators that preserve the system and its purity[3]. Unitary operators U satisfy $UU^\dagger = U^\dagger U = \mathbb{1}$, so the previous statements are easily proven. Denoting the input state by ρ and the output state by $U\rho U^\dagger$, we have

$$P_{\text{output}} = \mathrm{tr}[U\rho U^\dagger] = \mathrm{tr}[\rho U^\dagger U] = 1, \tag{2.16}$$

$$\mathcal{P}_{\text{output}} = \mathrm{tr}[U\rho U^\dagger U\rho U^\dagger] = \mathrm{tr}[\rho^2] = \mathcal{P}_{\text{input}}. \tag{2.17}$$

Here, we used the cyclic property of trace, $\mathrm{tr}[XY] = \mathrm{tr}[YX]$.

Quantum mechanical states are rarely passive entities that only change when experimentalists send them through beam splitters, wave plates, or polarizers. States

[3] In fact, a HWP with its fast axis 22.5° from the horizontal axis can be described with a Hadamard operator.

can also change continuously with time, whether an experimentalist means them or not to. Given a *time-evolution operator* $U(t)$, the evolution of a pure state can be written as $|\psi(t)\rangle = U(t)|\psi(0)\rangle$. With uniform dynamics, the time-evolution operators satisfy $U(s)U(t) = U(t)U(s) = U(t+s)$, i.e., there is no difference in a state evolving first for the time interval t, then s, in the other order, or the whole interval $t+s$ at once. Furthermore, evolution of zero time span is simply given by the identity, $U(0) = \mathbb{1}$.

We are now in the position to derive the famous *Schrödinger's equation* [85]. Let us begin by introducing a small change in time, $t+\epsilon$, so that the corresponding time-evolution operator is given by $U(t+\epsilon) = U(\epsilon)U(t)$. Expanding $U(\epsilon)$ as a Taylor series in 0, we obtain

$$U(\epsilon) = U(0) + \epsilon\frac{\partial}{\partial t}U(t)|_{t=0} + \frac{\epsilon^2}{2}\frac{\partial^2}{\partial t^2}U(t)|_{t=0} + ... \tag{2.18}$$

With continuous dynamics and small enough changes, $U(\epsilon)$ is linear in ϵ, meaning that $\epsilon^n \approx 0$ when $n \geq 2$. Denoting $\frac{\partial}{\partial t}U(t)|_{t=0} = -\frac{i}{\hbar}H$ (with $\hbar$ being the reduced Planck's constant), we get

$$U(t+\epsilon)|\psi(0)\rangle = U(\epsilon)U(t)|\psi(0)\rangle \tag{2.19}$$

$$\Leftrightarrow |\psi(t+\epsilon)\rangle = \Big(\mathbb{1} - \frac{i\epsilon}{\hbar}H\Big)|\psi(t)\rangle \tag{2.20}$$

$$= |\psi(t)\rangle - \frac{i\epsilon}{\hbar}H|\psi(t)\rangle \tag{2.21}$$

$$\Leftrightarrow \frac{|\psi(t+\epsilon)\rangle - |\psi(t)\rangle}{\epsilon} = -\frac{i}{\hbar}H|\psi(t)\rangle. \tag{2.22}$$

Letting ϵ approach 0, we finally arrive at the Schrödinger's equation

$$i\hbar\frac{\partial}{\partial t}|\psi(t)\rangle = H|\psi(t)\rangle. \tag{2.23}$$

The solution of Eq. (2.23) reads

$$|\psi(t)\rangle = e^{-\frac{iHt}{\hbar}}|\psi(0)\rangle, \tag{2.24}$$

where the exponential function can be identified as the time-evolution operator, $U(t) = e^{-iHt/\hbar}$. Sometimes, one uses units where $\hbar = 1$, and so do we in the rest of this Thesis. Furthermore, the operator H is known as the *Hamiltonian*[4]. Note that, with uniform dynamics, the Hamiltonian is independent of time. With $U(t)$, one can write the time evolution of a statistical mixture of pure states $\sum_j p_j|\psi_j\rangle\langle\psi_j|$ as

$$\rho(t) = \sum_j p_j U(t)|\psi_j(0)\rangle\langle\psi_j(0)|U(t)^\dagger. \tag{2.25}$$

[4]Now H can mean the Hadamard operator, horizontal polarization, or the Hamiltonian. Its meaning should still be clear from the context.

If the time evolution of a quantum system can be written in this form, the system is called a *closed quantum system* [6].

3 Dynamics of open quantum systems

In this Chapter we notice that, under special circumstances, quantum dynamics cannot be described by unitary operators. Instead, we need the theory of open quantum systems and quantum dynamical maps. We go through (pure) decoherence, describe its photonic model in full detail, and introduce a few definitions of (quantum) non-Markovianity.

3.1 Open quantum systems and dynamical maps

Let us begin by exploring the time evolution of a bipartite system, initially in the pure product state $|\psi_{AB}(0)\rangle = |\psi_A(0)\rangle \otimes |\psi_B(0)\rangle$. The time-evolution operator is now given by $U_{AB}(t) = e^{-iH_{AB}t}$, so the dynamics of our system of interest reads

$$|\psi_{AB}(t)\rangle = U_{AB}(t)|\psi_A(0)\rangle \otimes |\psi_B(0)\rangle. \tag{3.1}$$

If the Hamiltonian H_{AB} can be written in the form $H_{AB} = H_A \otimes \mathbb{1}_B + \mathbb{1}_A \otimes H_B$, the unitary operator factorizes, $U_{AB}(t) = e^{-i(H_A \otimes \mathbb{1}_B)t} e^{-i(\mathbb{1}_A \otimes H_B)t} = e^{-iH_A t} \otimes e^{-iH_B t} = U_A(t) \otimes U_B(t)$, and the state $|\psi_{AB}(t)\rangle$ remains a product state,

$$\begin{aligned} |\psi_{AB}(t)\rangle &= U_A(t) \otimes U_B(t)|\psi_A(0)\rangle \otimes |\psi_B(0)\rangle & (3.2)\\ &= U_A(t)|\psi_A(0)\rangle \otimes U_B(t)|\psi_B(0)\rangle & (3.3)\\ &= |\psi_A(t)\rangle \otimes |\psi_B(t)\rangle. & (3.4) \end{aligned}$$

However, this is not generally the case. Namely, if the Hamiltonian H_{AB} contains some additional term H_I, so that $H_{AB} = H_A \otimes \mathbb{1}_B + \mathbb{1}_A \otimes H_B + H_I$, we might not be able to write the evolved state in the product form. From the previous Chapter we remember that this means that the state $|\psi_{AB}\rangle$ is entangled, and with nonzero concurrence the purity of the reduced state $\rho_A(t) = \mathrm{tr}_B[\rho_{AB}(t)]$ (or $\rho_B(t) = \mathrm{tr}_A[\rho_{AB}(t)]$) becomes less than one, i.e., $\mathcal{P}\big(\rho_A(t)\big) < 1$ [see Eq. (2.7)].

Now we come to an important question: If we are interested only in the dynamics of the reduced state $\rho_A(t)$, how to describe it mathematically? Unitary operators preserve the purity of a state, but we just reasoned that the purity $\mathcal{P}\big(\rho_A(t)\big)$ might not be constant in time. Before answering this question, let us ask another one: Why should we restrict our attention to a mere part of the whole system?

Quantum systems, as any other systems, are always surrounded by some environment. As a consequence, a system (labeled by S) and its environmental degrees

of freedom (E) need to be described by some joint state ρ_{SE}. If the system and environment are initially uncorrelated, we can write $\rho_{SE}(0) = \rho_S(0) \otimes \rho_E(0)$. However, if the Hamiltonian of the total system reads $H_{SE} = H_0 + H_I = H_S \otimes \mathbb{1}_E + \mathbb{1}_S \otimes H_E + H_I$ [1], the state evolves as described above, i.e., entangling ρ_S and ρ_E with each other. As opposed to closed systems, systems described by reduced states with nonconstant purity due to system-environment interactions are known as *open quantum systems* [6; 7; 8].

One is usually interested in the reduced open-system dynamics $\rho_S(t)$ for two main reasons. First, on a more fundamental level, such dynamics provides one explanation to why we seldom encounter macroscopic quantum systems, e.g., simultaneously dead and alive cats. The process of an open quantum system becoming classical due to system-environment interactions (or "noise") is known as *decoherence* [5]. Secondly, quantum technologies typically operate in the Hilbert space of $\rho_S(t)$. Taking the vast and often inaccessible environment into account would simply be far too difficult.

When there is no risk of confusion, we drop the lower indices and denote the states of open quantum systems and their environments by ρ and ξ, respectively. If the states are initially uncorrelated, we can describe the dynamics of ρ by a *dynamical map* Φ^t, defined by [6]

$$\rho(t) = \Phi^t\big(\rho(0)\big) \tag{3.5}$$

$$:= \mathrm{tr}_E[U(t)\rho(0) \otimes \xi(0)U(t)^\dagger]. \tag{3.6}$$

Depending on the system-environment coupling, there are different kinds of dynamical maps, but they should all be *convex linear*, *completely positive (CP)* and *trace-preserving (TP)* [6]. Convex linearity means that $\Phi^t\big(\sum_j p_j\rho_j\big) = \sum_j p_j\Phi^t(\rho_j)$. Complete positivity arises from the possibility of quantum entanglement, and it means that an entangled initial state ρ_{AB} remains physical under the action of a local map Φ^t_A, i.e., $\big(\Phi^t_A \otimes \mathbb{1}_B\big)(\rho_{AB}) \geq \mathcal{O}$. In fact, *Choi's theorem* states that Φ^t is CP if and only if the above condition is satisfied by the maximally entangled state $\rho_{AB} = P^+_d = |\psi^+_d\rangle\langle\psi^+_d|$, where $|\psi^+_d\rangle = \frac{1}{\sqrt{d}}\sum_{j=0}^{d-1}|j\rangle \otimes |j\rangle$ and d is the dimension of the map's Hilbert space [86]. Finally, trace-preservity simply means that $\mathrm{tr}\big[\Phi^t(\rho)\big] = \mathrm{tr}[\rho]$. Convex linear CPTP dynamical maps are also called *(quantum) channels*. Some typical single-qubit channels and examples of their underlying physical scenarios are listed in Table 3.1.

Kraus operators provide a nice way to describe quantum channels [89]. A dynamical map Φ^t is convex linear and CPTP (and thus, a channel) if and only if it can be written as

$$\Phi^t(\rho) = \sum_j K_j(t)\rho K_j(t)^\dagger, \tag{3.7}$$

[1] H_0 and H_I are called the *free* and *interaction Hamiltonians*, respectively.

Table 3.1. Typical channels, their actions on a qubit, and example physical scenarios.

Channel	Qubit evolution	Example scenario
Amplitude damping	$\begin{pmatrix} \rho_{00}+\gamma(t)\rho_{11} & \rho_{01}\sqrt{1-\gamma(t)} \\ \rho_{10}\sqrt{1-\gamma(t)} & \big(1-\gamma(t)\big)\rho_{11} \end{pmatrix}$	Spontaneous emission [87]
Depolarizing	$\frac{p(t)}{2}\mathbb{1} + \big(1-p(t)\big)\rho$	Spin systems in fluctuating magnetic fields [88]
Dephasing	$\begin{pmatrix} \rho_{00} & \rho_{01}e^{-\lambda(t)} \\ \rho_{10}e^{-\lambda(t)} & \rho_{11} \end{pmatrix}$	A qubit coupled to a bosonic bath [45]

where $K_j(t)$ are the Kraus operators that also need to satisfy $\sum_j K_j(t)^\dagger K_j(t) = \mathbb{1}$. If $\sum_j K_j(t)^\dagger K_j(t) \leq \mathbb{1}$, the dynamical map does not necessarily preserve the trace, and so we talk about completely positive and trace-nonincreasing (CPTNI) *quantum operations* instead of channels.

3.2 Pure decoherence

In the rest of this Thesis, we focus mainly on *pure decoherence* or *dephasing*, i.e., the process under which the coherences of an open system's density matrix vanish (see Table 3.1). Because the diagonal elements of a state remain intact, one can talk about "pure" quantum-to-classical transition; An open system's quantum properties disappear—making any application based on them futile—while its measurement statistics remain invariant. In addition to a qubit coupled to a bosonic bath, dephasing naturally appears in many other physical systems, e.g., nitrogen-vacancy centers in dark spin baths [10], a central spin coupled to an Ising chain [90], excitons in quantum dots [91], superconducting qubits under the influence of fluctuating magnetic dipoles [92], particles in spatial superpositions [93], and impurities coupled to Morse oscillators [94] or a Bose-Hubbard model [95].

3.2.1 General dephasing

Before concentrating on a single specific physical system, let us take a step back and see how dephasing generally arises from the interaction Hamiltonian [6]. We take the interaction Hamiltonian to be of the form $H_I = \sum_j |j\rangle\langle j| \otimes E_j$. The projections $|j\rangle\langle j|$ effectively single out the orthonormal basis vectors $|j\rangle$ of an open-system state, while the operators $E_j = E_j^\dagger$ are arbitrary operators of the environment. We make only one other assumption, namely, that $[H_S, |j\rangle\langle j|] = 0$ [2]. This assumption has two immediate consequences. First, the open system's energy is a *conserved quantity*.

[2] $[X, Y] = XY - YX$ is called the *commutator* of X and Y.

In quantum mechanics, *observables* (such as position, momentum, and energy) are described by Hermitian operators $X = X^\dagger$ with the state-dependent mean values $\langle X \rangle_t := \langle \psi(t) | X | \psi(t) \rangle$. Then, by "conserved quantities", we mean observables with time-invariant expectation values, $\frac{\partial}{\partial t} \langle X \rangle_t = 0$. The open system's energy is described by $H_S \otimes \mathbb{1}_E$, so we get

$$\begin{aligned}
\frac{\partial}{\partial t} \langle \psi(t) | (H_S \otimes \mathbb{1}_E) | \psi(t) \rangle &= \langle \dot{\psi}(t) | (H_S \otimes \mathbb{1}_E) | \psi(t) \rangle \\
&\quad + \langle \psi(t) | (H_S \otimes \mathbb{1}_E) | \dot{\psi}(t) \rangle && (3.8) \\
&= i \langle [H_{SE}, H_S \otimes \mathbb{1}_E] \rangle_t && (3.9) \\
&= i \langle [H_S \otimes \mathbb{1}_E + \mathbb{1}_S \otimes H_E \\
&\quad + \sum_j |j\rangle\langle j| \otimes E_j, H_S \otimes \mathbb{1}_E] \rangle_t && (3.10) \\
&= 0 \text{ by the assumption.} && (3.11)
\end{aligned}$$

Secondly, as $[H_S, |j\rangle\langle j|] = 0$ directly results in $[H_{SE}, |j\rangle\langle j| \otimes \mathbb{1}_E] = 0$, also $|j\rangle\langle j| \otimes \mathbb{1}_E$ conserves in time.

Let us proceed by moving to the so-called *interaction picture*. That is, we consider the time-*dependent* interaction Hamiltonian $H_I(t) = e^{iH_0 t} H_I e^{-iH_0 t} = \sum_j |j\rangle\langle j| \otimes e^{iH_0 t} E_j e^{-iH_0 t} = \sum_j |j\rangle\langle j| \otimes E_j(t)$ and replace the time-evolution operator $U(t) = \exp(-iHt)$ with

$$U(t) = e^{-i \int_0^t ds H_I(s)}. \tag{3.12}$$

Denoting a pure and uncorrelated initial state by $|\psi(0)\rangle = \sum_j C_j |j\rangle \otimes |\xi\rangle$, we get

$$\begin{aligned}
|\psi(t)\rangle &= e^{-i \int_0^t ds \sum_j |j\rangle\langle j| \otimes E_j(s)} \sum_k C_k |k\rangle \otimes |\xi\rangle && (3.13) \\
&= \sum_j C_j |j\rangle \otimes e^{-i \int_0^t ds E_j(s)} |\xi\rangle && (3.14) \\
&= \sum_j C_j |j\rangle \otimes |\xi_j(t)\rangle. && (3.15)
\end{aligned}$$

Then, partial tracing over the environment (using some basis $\{|\xi_j\rangle\}_j$) yields

$$\begin{aligned}
\rho(t) &= \sum_j \langle \xi_j | \sum_k C_k |k\rangle \otimes |\xi_k(t)\rangle \sum_l C_l^* \langle l| \otimes \langle \xi_l(t) | \xi_j \rangle && (3.16) \\
&= \sum_{j,k,l} C_k C_l^* |k\rangle\langle l| \langle \xi_j | \xi_k(t) \rangle \langle \xi_l(t) | \xi_j \rangle && (3.17) \\
&= \sum_{j,k,l} C_k C_l^* |k\rangle\langle l| \langle \xi_l(t) | \xi_j \rangle \langle \xi_j | \xi_k(t) \rangle && (3.18) \\
&= \sum_{k,l} C_k C_l^* |k\rangle\langle l| \langle \xi_l(t) | \xi_k(t) \rangle. && (3.19)
\end{aligned}$$

Due to unitarity, $\langle\xi_j(t)|\xi_j(t)\rangle = 1$. Hence, one can see from Eq. (3.19) that the diagonal elements $\langle j|\rho(t)|j\rangle = |C_j|^2$ do not change with time. However, this is not generally the case for the off-diagonal elements $\langle j|\rho(t)|k\rangle = C_j C_k^* \langle\xi_k(t)|\xi_j(t)\rangle$, $j \neq k$. We call the inner products $\langle\xi_k(t)|\xi_j(t)\rangle$ *decoherence functions*, and their exact forms depend on the operators $E_j(t) = e^{iH_0 t} E_j e^{-iH_0 t}$. Typically, with long enough interaction times, $\langle\xi_k(t)|\xi_j(t)\rangle \to \delta_{k,j}$ and therefore $\rho(t) \to \sum_j |C_j|^2 |j\rangle\langle j|$, i.e., the initial system state $\sum_j C_j|j\rangle$ becomes its classical counterpart.

3.2.2 Photonic dephasing

We now introduce the linear optical dephasing model of whose engineering and utilization we are interested in in this Thesis. For simplicity, we restrict our attention first to initially uncorrelated single-photon states. Two photons and initial system-environment correlations are considered in later Chapters.

Here, the polarization degree of freedom of a single photon is the open quantum system, the same photon's frequency represents the environment, and the system-environment (polarization-frequency) interaction is realized in a birefringent medium (e.g., quartz), where the polarization components propagate at different velocities. The initial state of the total system is given by

$$|\psi(0)\rangle = (C_H|H\rangle + C_V|V\rangle) \int df\, g(f)|f\rangle, \tag{3.20}$$

where C_H and C_V are, as before, probability amplitudes for the photon to be horizontally and vertically polarized, respectively. Similarly, $g(f)$ is the probability amplitude of the frequency f, but in the continuous sense: The probability of the photon's frequency to be in the interval $[f_a, f_b]$ is $P(f_a \leq f \leq f_b) = \int_{f_a}^{f_b} df |g(f)|^2$. Thus, we have the normalization condition $\int df |g(f)|^2 = 1$.

The interaction Hamiltonian governing the system's evolution in a birefringent medium is $H_I = -(n_H|H\rangle\langle H| + n_V|V\rangle\langle V|) \int df 2\pi f |f\rangle\langle f|$, where n_H (n_V) is the medium's refractive index corresponding to horizontal (vertical) polarization[3]. Since we have no free evolution inside the medium, it suffices to show how this Hamiltonian alone acts on the joint state vector $|\lambda\rangle|f\rangle$, $\lambda = H, V$:

$$U(t)|\lambda\rangle|f\rangle = e^{-iH_I t}|\lambda\rangle|f\rangle \tag{3.21}$$

$$= \sum_{j=0}^{\infty} \frac{[i(n_H|H\rangle\langle H| + n_V|V\rangle\langle V|) \int df' 2\pi f' |f'\rangle\langle f'|t]^j}{j!} |\lambda\rangle|f\rangle \tag{3.22}$$

[3]To be precise, one should take dispersion of the refractive indices into account by using the *Sellmeier equations* $n_H(f)$ and $n_V(f)$ [96; 97]. However, the refractive indices can be treated as constants on small enough frequency intervals, as we do in the theoretical parts of this Thesis.

$$= \sum_{j=0}^{\infty} \frac{[i^j (n_H^j |H\rangle\langle H| + n_V^j |V\rangle\langle V|) \int df' (2\pi f')^j |f'\rangle\langle f'| t^j]}{j!} |\lambda\rangle|f\rangle \tag{3.23}$$

$$= \sum_{j=0}^{\infty} \frac{(i2\pi f n_\lambda t)^j}{j!} |\lambda\rangle|f\rangle \tag{3.24}$$

$$= e^{i2\pi f n_\lambda t} |\lambda\rangle|f\rangle. \tag{3.25}$$

Hence, the evolution of the total system-environment state reads

$$|\psi(t)\rangle = U(t)|\psi(0)\rangle \tag{3.26}$$

$$= C_H |H\rangle \int df g(f) e^{i2\pi f n_H t} |f\rangle + C_V |V\rangle \int df g(f) e^{i2\pi f n_V t} |f\rangle. \tag{3.27}$$

Finally, the open-system dynamics is obtained by partial tracing over the environment:

$$\rho(t) = \mathrm{tr}_E[U(t)|\psi(0)\rangle\langle\psi(0)|U(t)^\dagger] \tag{3.28}$$

$$\begin{aligned} = \int df \langle f| \Big(& |C_H|^2 |H\rangle\langle H| \int df' df'' g(f') g(f'')^* e^{i2\pi (f' n_H - f'' n_H) t} |f'\rangle\langle f''| \\ & + C_H C_V^* |H\rangle\langle V| \int df' df'' g(f') g(f'')^* e^{i2\pi (f' n_H - f'' n_V) t} |f'\rangle\langle f''| \\ & + C_H^* C_V |V\rangle\langle H| \int df' df'' g(f') g(f'')^* e^{i2\pi (f' n_V - f'' n_H) t} |f'\rangle\langle f''| \\ & + |C_V|^2 |V\rangle\langle V| \int df' df'' g(f') g(f'')^* e^{i2\pi (f' n_V - f'' n_V) t} |f'\rangle\langle f''| \Big) |f\rangle \end{aligned} \tag{3.29}$$

$$\begin{aligned} = \int df \Big(& |C_H|^2 |H\rangle\langle H| |g(f)|^2 + C_H C_V^* |H\rangle\langle V| |g(f)|^2 e^{i2\pi f (n_H - n_V) t} \\ & + C_H^* C_V |V\rangle\langle H| |g(f)|^2 e^{i2\pi f (n_V - n_H) t} + |C_V|^2 |V\rangle\langle V| |g(f)|^2 \Big) \end{aligned} \tag{3.30}$$

$$= \begin{pmatrix} |C_H|^2 & C_H C_V^* \kappa(t) \\ C_H^* C_V \kappa(t)^* & |C_V|^2 \end{pmatrix}. \tag{3.31}$$

Here, $\kappa(t) = \int df |g(f)|^2 e^{i2\pi f \Delta n t}$ is the decoherence function and $\Delta n = n_H - n_V$ is the medium's birefringence. Interestingly, the decoherence function is the frequency distribution's Fourier transform and independent of the environment's coherences. Furthermore, the concurrence of the open system and its environment in this case becomes

$$\mathcal{C}(\rho_{SE}) = 2|C_H||C_V|\sqrt{1 - |\kappa(t)|^2}. \tag{3.32}$$

The smaller the decoherence function, the more entangled the open system is with its environment.

If we choose the Gaussian distribution $|g(f)|^2 = \exp\left[-\frac{1}{2}\left(\frac{f-\mu}{\sigma}\right)^2\right]/\sqrt{2\pi\sigma^2}$, with μ and σ being its mean frequency and standard deviation, we obtain

$$\kappa(t) = e^{i2\pi\mu\Delta n t - \frac{1}{2}(2\pi\sigma\Delta n t)^2}. \tag{3.33}$$

Unless otherwise stated, we take the frequency integral(s) from $-\infty$ to ∞. In the case of a Gaussian spectrum, large enough ratio μ/σ makes this a good approximation. For example, with $\mu = 3.84 \times 10^{14}$ Hz and $\sigma = 5.68 \times 10^{11}$ Hz, the nonphysical part becomes negligibly small, $\int_{-\infty}^{0} df|g(f)|^2 \sim 10^{-99251}$.

The above decoherence function makes the initial open-system state rotate around the Bloch ball's z-axis with the frequency $2\pi\mu\Delta n$, while the state's coherences undergo Gaussian decay of the time scale $(2\pi\sigma\Delta n)^{-1}$. That is, the wider the spectrum, the faster dephasing we have. This is quite intuitive. Say, we had a discrete frequency mode instead of the continuous spectrum. Then, the "decoherence function" corresponding to the mode $|f\rangle$ would simply be the phase factor $e^{i2\pi f\Delta n t}$. However, when we have multiple modes that come from a continuous distribution $|g(f)|^2$ and cannot be distinguished, they need to be averaged over. With small σ, there is not much to be averaged, and the phase factors remain quite close to $e^{i2\pi\mu\Delta n t}$. With large σ, it is the opposite. The phase factors $e^{i2\pi f\Delta n t}$ corresponding to deviating values of f quickly spread around the unit circle in the complex plane with their average approaching its origin. This is illustrated in Fig. 3.1.

Slowing down dephasing by downsizing the environment—which in the linear optical case means narrowing the frequency spectrum—is an example of *reservoir engineering*. With reservoir engineering, one usually refers to manipulating the initial environment state $\xi(0)$ [28]. In this Thesis, we use the term in a broader sense, covering the initial system-environment correlations as well.

The dephasing rate also depends on the number of photons under noise. Say, we had the N-photon state $(|H\rangle^{\otimes N} + |V\rangle^{\otimes N})/\sqrt{2}$, also known as the *Greenberger-Horne-Zeilinger (GHZ) state* [98], interacting with N uncorrelated frequency distributions in equally thick and parallel birefringent crystals. The decoherence function would then simply be the product of all the single-photon functions, $\kappa_{\text{GHZ}}(t) = \prod_{j=1}^{N} \kappa_j(t)$. With N equally wide Gaussian spectra, we would have dephasing of the time scale $(2\pi\sigma\Delta n\sqrt{N})^{-1}$. This goes to demonstrate that the bigger the open system, the faster it can (and typically will) decohere.

Returning to the single-photon case, it is illustrative to study dephasing in the time domain, too. Multiplying the right-hand side of Eq. (3.27) from left by $\int ds|s\rangle\langle s| = \mathbb{1}$, where s is the time of the photon arriving at a photodetector, using $\langle s|f\rangle =$

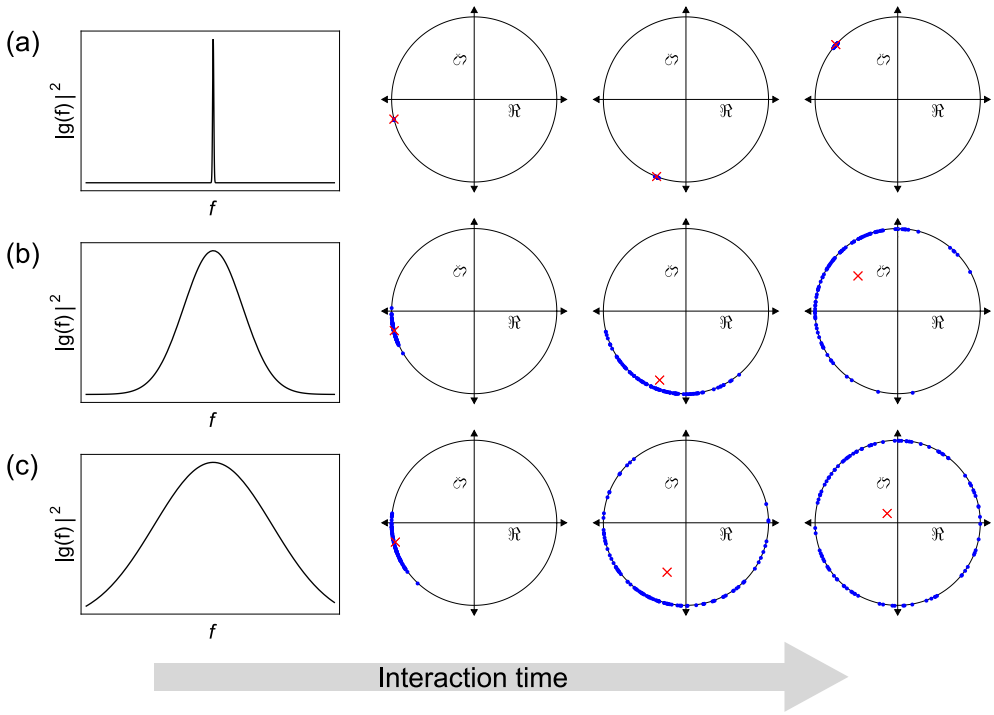

Figure 3.1. Visualization of dephasing. On the left, we have three Gaussian frequency distributions $|g(f)|^2$ of different widths σ. On the right, we have considered three different interaction times, increasing from left to right. In each case, we have drawn 100 frequencies from the distribution shown to their left. The corresponding phase factors lie on the unit circles (blue dots), while their averages are inside of the circles (red crosses).

$e^{-i2\pi fs}$ [99], and assuming Gaussianity and that $g(f) = |g(f)|$ [4], we obtain

$$|\psi(t)\rangle = (8\pi\sigma^2)^{\frac{1}{4}}\Big(C_H|H\rangle \int ds e^{i2\pi\mu(n_H t-s)-[2\pi\sigma(n_H t-s)]^2}|s\rangle \\ +C_V|V\rangle \int ds e^{i2\pi\mu(n_V t-s)-[2\pi\sigma(n_V t-s)]^2}|s\rangle\Big). \tag{3.34}$$

Now, we can solve the arrival-time distribution $|\hat{g}(s)|^2$ by partial tracing $|\psi(t)\rangle\langle\psi(t)|$ over polarization and sandwiching the result between $\langle s|$ and $|s\rangle$. Doing so, we arrive at

$$|\hat{g}(s)|^2 = \sqrt{8\pi\sigma^2}\Big(|C_H|^2 e^{-2[2\pi\sigma(s-n_H t)]^2} + |C_V|^2 e^{-2[2\pi\sigma(s-n_V t)]^2}\Big). \tag{3.35}$$

The right-hand side of Eq. (3.35) is just a convex combination of two translated Gaussians, with the translations $n_H t$ and $n_V t$ weighted by $|C_H|^2$ and $|C_V|^2$, respectively. With no interaction, the Gaussians overlap and it is more probable to detect

[4] This is a reasonable assumption, since the phases of the frequency amplitudes in SPDC are not random [43].

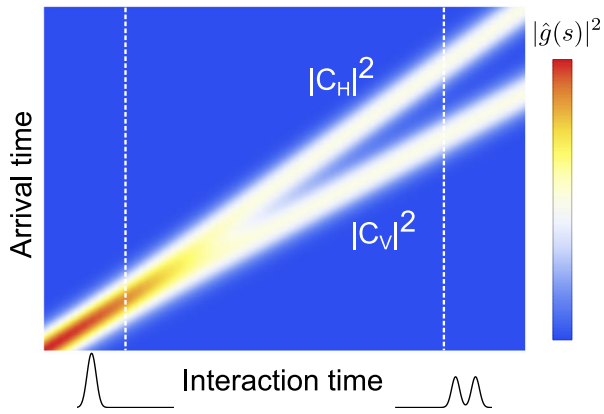

Figure 3.2. Arrival-time distribution $|\hat{g}(s)|^2$ as a function of the arrival time and interaction time. Here, $|C_H|^2 = |C_V|^2 = 0.5$ and $n_H > n_V$, i.e., horizontal polarization moves slower. Thus, its expected arrival time is later. The distributions at the bottom of the picture correspond to the intersections given by the dashed lines.

the photon earlier, around $s = 0$ (see Fig. 3.2). In a birefringent medium, the horizontal and vertical polarization components propagate at different velocities and the two Gaussians diverge. Because the photon has moved slower, it is more probable to detect it later. Interestingly, between the faster and slower component, we have a region where $P(s_a \leq s \leq s_b) \approx 0$.

The dephasing channel we have described is clearly convex linear and trace-preserving. For the channel to be CP, we must have $(\Phi_A^t \otimes \mathbb{1}_B)(|\Phi^+\rangle\langle\Phi^+|) \geq \mathcal{O}$:

$$\det\left[(\Phi_A^t \otimes \mathbb{1}_B)(|\Phi^+\rangle\langle\Phi^+|) - \lambda\mathbb{1}_{AB}\right] = \begin{vmatrix} 1/2-\lambda & 0 & 0 & \kappa(t)/2 \\ 0 & -\lambda & 0 & 0 \\ 0 & 0 & -\lambda & 0 \\ \kappa(t)^*/2 & 0 & 0 & 1/2-\lambda \end{vmatrix} \tag{3.36}$$

$$= \left(\frac{1}{2}-\lambda\right)^2\lambda^2 - \frac{|\kappa(t)|^2}{4}\lambda^2 = 0 \tag{3.37}$$

$$\Leftrightarrow \lambda_1 = \lambda_2 = 0, \lambda_3 = \frac{1+|\kappa(t)|}{2}, \lambda_4 = \frac{1-|\kappa(t)|}{2} \tag{3.38}$$

$$\lambda_4 \geq 0 \Leftrightarrow |\kappa(t)| \leq 1. \tag{3.39}$$

The above calculation shows that the dephasing channel is CP as long as the decoherence function's absolute value is at most one. Larger absolute values would map the qubit outside of the Bloch ball, resulting in probabilities outside of the interval $[0, 1]$. Because $\Phi^0 = \mathbb{1}$, the inequalities in Eq. (3.39) are saturated with $t = 0$. However, by controlling the initial system-environment correlations, we can go beyond the conventional channel-description of the dynamics and have $|\kappa(0)| < 1$. Although a dynamical map does not exist in correlated cases, the open-system dynamics can

still be physical. A canonical description for such dynamics is still missing, although some have been proposed, e.g., "bath-positive decompositions" [100].

Let us end this Section by addressing the elephant in the room: How can the frequency degree of freedom be considered an "environment"? Furthermore, doesn't the fact that, e.g., $\Delta n_{\text{air}} \approx 0$ absolve us from the problematics of decoherence? Couldn't we use photons in free air as fully decoherence-free information carriers?

Although the frequency is not an inaccessible "bath" or "reservoir", the open-system dynamics—i.e., dephasing of polarization—can be described in exactly the same fashion. Hence, *from the point of view of polarization*, the frequency effectively *acts* as an environment. As for the second question: Photons are, in fact, used in *linear optical quantum computing (LOQC)* due to their long coherence times [101]. However, quantum information processing with photons has problems of its own, e.g., poor scalability. But for emulating open-system dynamics, photons are perfect, allowing us to develop new, proof-of-principle quantum information protocols under noise and test existing ones. Conversely, the concepts of open quantum systems can be used in linear optics, interferometry, and parameter estimation, as we will see in Chapter 5.

3.3 Non-Markovianity

Markovianity and *non-Markovianity* are important concepts related to the dynamics of open quantum systems. Before going to quantum (non-)Markovianity, let us briefly discuss stochastic processes and classical (non-)Markovianity [102].

3.3.1 Classical case and CP-divisibility

A stochastic process $\{X(t) \in \mathcal{X}, t \in \mathcal{T}\}$ is a family of t-dependent random variables $X(t)$ that take values from some fixed set $\mathcal{X}$, while t, usually taken to be time, takes values from the interval $\mathcal{T}$. Then, $X(t_n) = x_n$ with some probability $P(x_n, t_n)$. The process is said to be *memoryless* or *Markovian*, if this probability, conditioned on all the previous values $x_{n-1}, x_{n-2}, ..., x_0$ at the respective time instants $t_{n-1} \geq t_{n-2} \geq ... \geq t_0$, only depends on the process's last preceding state,

$$P(x_n, t_n | x_{n-1}, t_{n-1}; x_{n-2}, t_{n-2}; ...; x_0, t_0) = P(x_n, t_n | x_{n-1}, t_{n-1}). \tag{3.40}$$

Otherwise, the process is non-Markovian.

The probability $P(x_n, t_n)$ can be written in terms of all the possible probabilities at some earlier point of time, $t_m \leq t_n$, as

$$P(x_n, t_n) = \sum_{x_m \in \mathcal{X}} T(x_n, t_n | x_m, t_m) P(x_m, t_m), \tag{3.41}$$

where $T(x_n, t_n | x_m, t_m)$ is a *transition matrix* also known as the *propagator*. Because $P(x_n, t_n) \geq 0$ and $\sum_{x_n \in \mathcal{X}} P(x_n, t_n) = 1$, the propagator needs to satisfy

$T(x_n, t_n|x_m, t_m) \geq 0 \; \forall x_n, x_m \in \mathcal{X}$ and $\sum_{x_n \in \mathcal{X}} T(x_n, t_n|x_m, t_m) = 1 \; \forall x_m \in \mathcal{X}$. A matrix satisfying these two properties is a *stochastic matrix*. Furthermore, if the process is Markovian, the propagator $T(x_n, t_n|x_m, t_m)$ can be identified as the conditional probability $P(x_n, t_n|x_m, t_m)$ by looking at the two-point probability $P(x_n, t_n; x_m, t_m)$:

$$P(x_n, t_n; x_m, t_m) = P(x_n, t_n|x_m, t_m)P(x_m, t_m) \tag{3.42}$$

$$\Rightarrow \sum_{x_m \in \mathcal{X}} P(x_n, t_n; x_m, t_m) = \sum_{x_m \in \mathcal{X}} P(x_n, t_n|x_m, t_m)P(x_m, t_m) \tag{3.43}$$

$$\Leftrightarrow P(x_n, t_n) = \sum_{x_m \in \mathcal{X}} P(x_n, t_n|x_m, t_m)P(x_m, t_m). \tag{3.44}$$

We can now show that a Markovian process $\{X(t) \in \mathcal{X}, t \in \mathcal{T}\}$ is *divisible*. We start by decomposing the probability of three consecutive events:

$$P(x_2, t_2; x_1, t_1; x_0, t_0) = P(x_2, t_2|x_1, t_1; x_0, t_0)P(x_1, t_1; x_0, t_0) \tag{3.45}$$

$$= P(x_2, t_2|x_1, t_1; x_0, t_0)P(x_1, t_1|x_0, t_0)P(x_0, t_0) \tag{3.46}$$

$$= P(x_2, t_2|x_1, t_1)P(x_1, t_1|x_0, t_0)P(x_0, t_0) \tag{3.47}$$

$$\Rightarrow \sum_{x_1 \in \mathcal{X}} \frac{P(x_2, t_2; x_1, t_1; x_0, t_0)}{P(x_0, t_0)} = \sum_{x_1 \in \mathcal{X}} P(x_2, t_2|x_1, t_1)P(x_1, t_1|x_0, t_0) \tag{3.48}$$

$$\Leftrightarrow P(x_2, t_2|x_0, t_0) = \sum_{x_1 \in \mathcal{X}} P(x_2, t_2|x_1, t_1)P(x_1, t_1|x_0, t_0) \tag{3.49}$$

$$\Leftrightarrow T(x_2, t_2|x_0, t_0) = \sum_{x_1 \in \mathcal{X}} T(x_2, t_2|x_1, t_1)T(x_1, t_1|x_0, t_0). \tag{3.50}$$

It should now become clear what we mean by "divisibility"; The propagator describing the evolution of a Markovian stochastic process can be divided into intermediate parts, first giving the evolution from t_0 to $t_1 \geq t_0$, then from t_1 to $t_2 \geq t_1$. Although divisibility does not guarantee Markovianity in general, they can be shown to coincide with one-point probabilities.

In the theory of open quantum systems, Markovianity can be defined in similar terms [102]. Going from classical stochastic processes to open-system dynamics is a subtle issue—and we refer to [28] for more detailed discussion—but for the purposes of this Thesis, it suffices to look at the simple substitutions $P(x, t) \mapsto \rho(t)$ and $\sum_{x_m \in \mathcal{X}} T(x_n, t_n|x_m, t_m)P(x_m, t_m) \mapsto \Phi^{t_n \leftarrow t_m}\big(\rho(t_m)\big)$. That is, we replace the single-point probabilities and classical propagators with their quantum versions.

Then, starting from the classical case and having $t_2 \geq t_1$, we can write

$$P(x_2, t_2) = \sum_{x_1 \in \mathcal{X}} T(x_2, t_2 | x_1, t_1) P(x_1, t_1) \tag{3.51}$$

$$\mapsto \rho(t_2) = \Phi^{t_2 \leftarrow t_1}\big(\rho(t_1)\big) \tag{3.52}$$

$$\Leftrightarrow \Phi^{t_2} = \Phi^{t_2 \leftarrow t_1} \circ \Phi^{t_1}. \tag{3.53}$$

We see that, like in the case of classical stochastic processes, the open-system dynamics from 0 to t_2 can be described first with a dynamical map Φ^{t_1} and then with a quantum propagator $\Phi^{t_2 \leftarrow t_1}$. However, this alone does not guarantee quantum Markovianity. With classical stochastic processes, the propagator also needed to be positive and sum up to unity. Now, due to the possibility of an entangled ancilla, the quantum propagator needs to be *completely* positive and trace-preserving. Hence, we conclude that the dynamics of an open quantum system in the time interval $[t_1, t_2]$ is *CP-divisible* and therefore Markovian, if the intermediate propagator $\Phi^{t_2 \leftarrow t_1}$ is CPTP. Conversely, if there exists a time interval with the corresponding propagator *not* being CPTP, the (whole) dynamics is said to be non-Markovian.

One could naïvely write the propagator as $\Phi^{t_2 \leftarrow t_1} = \Phi^{t_2 - t_1}$. Dynamical maps with this propagator are called *dynamical semigroups* [6]. However, while some maps admit the semigroup property, e.g., single-photon dephasing with Lorentzian frequency distribution and the decoherence function $\kappa(t) = e^{i2\pi f_0 \Delta n t - 2\pi\gamma\Delta n t}$, it does not hold in general (see, e.g., the Gaussian single-photon decoherence function). The Kraus operators

$$K_{\pm}(t_1, t_2) = \sqrt{\frac{1 \pm \frac{|\kappa(t_2)|}{|\kappa(t_1)|}}{2}} \begin{pmatrix} \pm \frac{\kappa(t_2)}{\kappa(t_1)} \frac{|\kappa(t_1)|}{|\kappa(t_2)|} & 0 \\ 0 & 1 \end{pmatrix} \tag{3.54}$$

define general propagator for single-qubit dephasing, as we can write

$$\Phi^{t_2 \leftarrow t_1}\big(\rho(t_1)\big) = K_+(t_1, t_2)\rho(t_1)K_+(t_1, t_2)^\dagger + K_-(t_1, t_2)\rho(t_1)K_-(t_1, t_2)^\dagger \tag{3.55}$$

$$= \begin{pmatrix} \rho_{00} & \rho_{01}\kappa(t_1)\frac{\kappa(t_2)}{\kappa(t_1)} \\ \rho_{10}\kappa(t_1)^* \frac{\kappa(t_2)^*}{\kappa(t_1)^*} & \rho_{11} \end{pmatrix} \tag{3.56}$$

$$= \begin{pmatrix} \rho_{00} & \rho_{01}\kappa(t_2) \\ \rho_{10}\kappa(t_2)^* & \rho_{11} \end{pmatrix}. \tag{3.57}$$

We can now show what the CP-divisibility means for general single-qubit de-

phasing. Requiring the propagator to be CP, we get

$$\det\left[(\Phi_A^{t_2\leftarrow t_1}\otimes \mathbb{1}_B)(|\Phi^+\rangle\langle\Phi^+|)-\lambda\mathbb{1}_{AB}\right]$$
$$=\begin{vmatrix} 1/2-\lambda & 0 & 0 & \kappa(t_2)/[2\kappa(t_1)] \\ 0 & -\lambda & 0 & 0 \\ 0 & 0 & -\lambda & 0 \\ \kappa(t_2)^*/[2\kappa(t_1)^*] & 0 & 0 & 1/2-\lambda \end{vmatrix} \tag{3.58}$$
$$=\left(\frac{1}{2}-\lambda\right)^2\lambda^2-\frac{|\kappa(t_2)/\kappa(t_1)|^2}{4}\lambda^2=0 \tag{3.59}$$
$$\Leftrightarrow \lambda_1=\lambda_2=0,\lambda_3=\frac{1+|\kappa(t_2)/\kappa(t_1)|}{2},\lambda_4=\frac{1-|\kappa(t_2)/\kappa(t_1)|}{2} \tag{3.60}$$
$$\lambda_4\geq 0\Leftrightarrow|\kappa(t_2)|\leq|\kappa(t_1)|. \tag{3.61}$$

The above calculation shows that, for single-qubit dephasing to be CP-divisible and Markovian, the coherences can never increase.

3.3.2 Trace distance and BLP-measure

Let us introduce an alternative definition of quantum non-Markovianity, based on *trace distance*. Say, Alice sends a message, encoded into a string of quantum states, to Bob[5]. Once the states have reached Bob, his success rate on recovering the intended message depends on the states' distinguishability; Two pure, orthogonal states can be distinguished from each other with certainty, while Bob needs to make a guess otherwise. The distinguishability of two states, ρ_1 and ρ_2, can be quantified by the trace distance [70]

$$\mathcal{D}_{\text{tr}}(\rho_1,\rho_2)=\frac{1}{2}\text{tr}|\rho_1-\rho_2|, \tag{3.62}$$

where $|X|=\sqrt{X^\dagger X}$ with $\sqrt{X}$ being the unique matrix satisfying $\sqrt{X}\sqrt{X}=X$.

Unfortunately for Alice and Bob, the systems carrying the message tend to be open quantum systems. That is, the initial states may become mixed under some environment-induced channel Φ^t, making ρ_1 and ρ_2 less distinguishable and forcing Bob to guess. Namely, it can be shown that quantum channels are contractions of trace distance [70],

$$\mathcal{D}_{\text{tr}}\big(\Phi^t(\rho_1),\Phi^t(\rho_2)\big)\leq\mathcal{D}_{\text{tr}}(\rho_1,\rho_2). \tag{3.63}$$

Since information, in the sense of the above discussion, may transform into system-environment correlations, one sometimes talks about *information flow* [29].

[5]Maybe they are executing the BB84 protocol.

However, as the total system-environment state is closed, the information is never really gone, and the open system may sometimes regain some of the previously lost information, i.e., experience *information backflow* or *memory effects*. In such situations, the trace distance can temporally increase, though never above its initial value. Then, the total increase of trace distance maximized with respect to the initial state pair,

$$\mathcal{N}(\Phi^t) = \max_{\rho_{1,2}(0)} \int_{\sigma>0} dt\sigma\big(t, \rho_{1,2}(0)\big), \tag{3.64}$$

can be interpreted as the amount of re-attainable information during the open system's whole time evolution induced by Φ^t. Here, $\sigma(t, \rho_{1,2}(0)\big) = \frac{\partial}{\partial t}\mathcal{D}_{tr}\big(\rho_1(t), \rho_2(t)\big)$. Eq. (3.64) is known as the *Breuer, Laine, and Piilo (BLP) measure* of non-Markovianity [103]. The channel is Markovian if $\mathcal{N}(\Phi^t) = 0$ and non-Markovian otherwise.

We get a rather simple expression for the trace distance with two qubits experiencing dephasing. Assuming pure initial states and denoting them by $|\psi_1\rangle = C_0|0\rangle + C_1|1\rangle$ and $|\psi_2\rangle = C_0'|0\rangle + C_1'|1\rangle$, we obtain

$$\mathcal{D}_{\text{tr}}\big(\rho_1(t), \rho_2(t)\big) = \frac{1}{2}\text{tr}\left| \begin{pmatrix} |C_0|^2 - |C_0'|^2 & (C_0C_1^* - C_0'C_1'^*)\kappa(t) \\ (C_0^*C_1 - C_0'^*C_1')\kappa(t)^* & |C_1|^2 - |C_1'|^2 \end{pmatrix} \right| \tag{3.65}$$

$$= \frac{1}{2}\text{tr}\sqrt{\big[(|C_0|^2 - |C_0'|^2)^2 + |C_0^*C_1 - C_0'^*C_1'|^2|\kappa(t)|^2\big]\mathbb{1}} \tag{3.66}$$

$$= \frac{\sqrt{(|C_0|^2 - |C_0'|^2)^2 + |C_0^*C_1 - C_0'^*C_1'|^2|\kappa(t)|^2}}{2}\text{tr}[\mathbb{1}] \tag{3.67}$$

$$= \sqrt{(|C_0|^2 - |C_0'|^2)^2 + |C_0^*C_1 - C_0'^*C_1'|^2|\kappa(t)|^2}. \tag{3.68}$$

Because $(|C_0|^2 - |C_0'|^2)^2$ and $|C_0^*C_1 - C_0'^*C_1'|^2$ are inversely proportional, maximizing the possible revivals of trace distance translates into minimizing the constant $(|C_0|^2 - |C_0'|^2)^2$ and maximizing the scaling factor in front of the dynamical part, $|C_0^*C_1 - C_0'^*C_1'|^2$. The first task is accomplished by setting $|C_0| = |C_0'|$. It follows that also $|C_1| = |C_1'|$. Therefore, we can write $C_0^{(\prime)*}C_1^{(\prime)} = |C_0||C_1|e^{i\theta^{(\prime)}}$ and $|C_0^*C_1 - C_0'^*C_1'|^2 = 2|C_0|^2|C_1|^2[1 - \cos(\theta - \theta')]$, which is maximized by setting $|C_0|^2 = |C_1|^2 = 1/2$ and $\theta - \theta' = \pi$. This means that the possible revivals of trace distance are maximized with any pair of initial states lying on antipodal points of the Bloch ball's equator. Using any such pair, e.g., $|\pm\rangle = (|0\rangle \pm |1\rangle)/\sqrt{2}$, yields

$$\mathcal{D}_{\text{tr}}\big(\rho_1(t), \rho_2(t)\big) = |\kappa(t)|. \tag{3.69}$$

From Eq. (3.69) we see that, with single-qubit dephasing, information flow is fully characterized by the absolute value of the decoherence function, the sign of its time derivative giving the direction of the flow; For information backflow and non-Markovian dynamics, we need to have $\frac{\partial}{\partial t}|\kappa(t)| > 0$. This coincides with the breaking of CP-divisibility [see Eq. (3.61)]. However, the two definitions do not generally

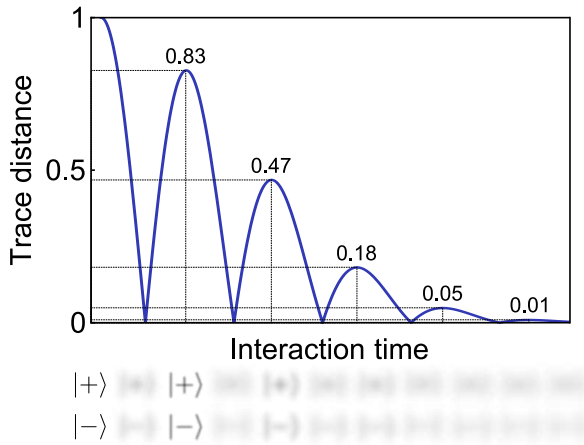

Figure 3.3. The trace-distance dynamics of the initial state pair $|\pm\rangle$, induced by a double-peaked Gaussian spectrum. The amounts of the trace distance increasing are shown on top of each "recoherence peak". In this case, we would have $\mathcal{N}(\Phi^t) \approx 1.54$. Trace distance as the distinguishability of states is further illustrated by the blurred state vectors at the bottom of the picture.

overlap (see, e.g., Ref. [104]). In fact, there is no sole, universally agreed definition of quantum (non-)Markovianity [31; 105], and the main reason for this lies within the measurement problem of quantum mechanics. As we saw in the previous Chapter, measurements change the state of interest—and therefore its dynamics, too. Some recently proposed definitions related to stochastic quantum processes have taken such state preparations and control operations into account [106; 107; 108; 109; 110; 111]. However, the continuous-time dephasing dynamics we are interested in does not fall into this category. Furthermore, as the trace-distance criterion has a simple analytic form and physical interpretation—and it coincides with many other indicators of non-Markovianity in the case of single-qubit dephasing, not just the breaking of CP-divisibility (e.g., negative *decay rates* of the *master equation* [112])—we shall use it as the criterion for quantum non-Markovianity in the rest of this Thesis.

Non-Markovianity is an interesting and important concept not just from the fundamental point of view related to information flow; Quantum information protocols (e.g., the *Deutsch–Jozsa algorithm* [10], quantum teleportation [49], and quantum key distribution [113]) have been shown to perform better under non-Markovian noise than Markovian. In addition, non-Markovianity can be used in parameter estimation, e.g., when evaluating initial correlations between two environments [41].

Now the question arises, how to go from Markovian to non-Markovian dephasing in the linear optical setting? The decoherence functions we have encountered so far—the Gaussian $\exp[i2\pi\mu\Delta nt-(2\pi\sigma\Delta nt)^2/2]$ and the Lorentzian $\exp(i2\pi f_0\Delta nt -2\pi\gamma\Delta nt)$—clearly describe Markovian dynamics (in terms of BLP-non-Markovianity), since their absolute values decrease monotonically. To achieve nonmono-

tonic dephasing, we could use a double-peaked Gaussian frequency distribution, $A|g_1(f)|^2+(1-A)|g_2(f)|^2$, with the peaks centered at μ_1 and μ_2 [46]. One example of the resulting dynamics is plotted in Fig. 3.3, with the initial state pair $|+\rangle \equiv |D\rangle$, $|-\rangle \equiv |A\rangle$ [6]. Introducing non-Markovian memory effects in this way is another example of reservoir engineering, and we will come back to the double-peaked Gaussian in Chapter 6. We will, e.g., fully characterize the spectrum's non-Markovian parameter space. Other ways to create, simulate, and harness non-Markovian memory effects in the linear optical framework are presented in Chapters 4 and 5.

[6] We shall use these notations for diagonally and antidiagonally polarized light in the rest of the Thesis.

4 Biphoton dephasing

This Chapter is dedicated to the dephasing of two photons, which allows us to explore the effects of initial system-system and environment-environment correlations. Due to these correlations, the two photons—not behaving as two separate entities—can also be called a *biphoton*. After introducing the basic model, we consider initial system-environment correlations, too, and describe how to create and control *memory partitions* and *reverse decoherence* with them. Finally, we apply reverse decoherence in noisy quantum teleportation.

4.1 The model

4.1.1 Local and nonlocal decoherence functions

The interaction Hamiltonian of biphoton dephasing is

$$H_I(t) = H_{I,A}\chi_A(t) \otimes \mathbb{1}_B + \mathbb{1}_A \otimes H_{I,B}\chi_B(t), \tag{4.1}$$

where the photons are labeled by A (for Alice) and B (for Bob). The Hamiltonians $H_{I,j}$ ($j = A, B$) act as before, coupling the polarization with frequency. The local form of Eq. (4.1) means that Alice's polarization does not interact with Bob's frequency and vice versa. Here, we have also considered different interaction times through the characteristic functions

$$\chi_j(t) = \begin{cases} 1 \text{ when } t_{i,j} \leq t \leq t_{f,j}, \\ 0 \text{ otherwise.} \end{cases} \tag{4.2}$$

That is, photon j enters a birefringent crystal at $t = t_{i,j}$ and exits it at $t = t_{f,j}$. The local unitaries $U_j(t)$ now act according to $U_j(t)|\lambda_j\rangle|f_j\rangle = e^{i2\pi f_j n_{\lambda_j} t_j(t)}|\lambda_j\rangle|f_j\rangle$, where the interaction times $t_j(t)$ depend on the photons' position with respect to the crystals,

$$t_j(t) = \int_0^t ds\chi_j(s) = \begin{cases} 0 \text{ if not yet entered,} \\ t - t_{i,j} \text{ if inside,} \\ t_{f,j} - t_{i,j} \text{ if exited.} \end{cases} \tag{4.3}$$

We denote Alice's (Bob's) total interaction time by $t_{A(B)} = t_{f,A(B)} - t_{i,A(B)}$. Here, we have omitted the global phase factors that the photons would acquire upon free evolution; They do not affect the open system's dynamics in this Chapter.

Now, with the initial state

$$|\psi(0)\rangle = \sum_{\lambda_A,\lambda_B=H,V} C_{\lambda_A\lambda_B}|\lambda_A\lambda_B\rangle \int df_A df_B g(f_A,f_B)|f_A f_B\rangle, \tag{4.4}$$

we get [cf. Eqs. (3.28)–(3.31)]

$$\rho_{AB}(t) = \Phi^t_{AB}\big(\rho_{AB}(0)\big) \tag{4.5}$$

$$= \mathrm{tr}_E[U_A(t)\otimes U_B(t)|\psi(0)\rangle\langle\psi(0)|U_A(t)^\dagger \otimes U_B(t)^\dagger] \tag{4.6}$$

$$= \begin{pmatrix} |C_{HH}|^2 & C_{HH}C^*_{HV}\kappa_B(t) & C_{HH}C^*_{VH}\kappa_A(t) & C_{HH}C^*_{VV}\kappa_{AB}(t) \\ C^*_{HH}C_{HV}\kappa_B(t)^* & |C_{HV}|^2 & C_{HV}C^*_{VH}\Lambda_{AB}(t) & C_{HV}C^*_{VV}\kappa_A(t) \\ C^*_{HH}C_{VH}\kappa_A(t)^* & C^*_{HV}C_{VH}\Lambda_{AB}(t)^* & |C_{VH}|^2 & C_{VH}C^*_{VV}\kappa_B(t) \\ C^*_{HH}C_{VV}\kappa_{AB}(t)^* & C^*_{HV}C_{VV}\kappa_A(t)^* & C^*_{VH}C_{VV}\kappa_B(t)^* & |C_{VV}|^2 \end{pmatrix}, \tag{4.7}$$

where the decoherence functions read

$$\kappa_j(t) = \int df_j |g_j(f_j)|^2 e^{i2\pi f_j \Delta n_j t_j(t)}, \tag{4.8}$$

$$\kappa_{AB}(t) = \int df_A df_B |g(f_A,f_B)|^2 e^{i[2\pi f_A \Delta n_A t_A(t) + 2\pi f_B \Delta n_B t_B(t)]}, \tag{4.9}$$

$$\Lambda_{AB}(t) = \int df_A df_B |g(f_A,f_B)|^2 e^{i[2\pi f_A \Delta n_A t_A(t) - 2\pi f_B \Delta n_B t_B(t)]}. \tag{4.10}$$

$|g_j(f_j)|^2$ in the *local decoherence functions* $\kappa_j(t)$ is the marginal frequency distribution obtained by averaging over the other party's frequency, i.e., $|g_{A(B)}(f_{A(B)})|^2 = \int df_{B(A)}|g(f_A,f_B)|^2$. Consequently, initial frequency correlations are locally undetectable in Eq. (4.7)[1]. On the contrary, the *nonlocal decoherence functions* $\kappa_{AB}(t)$ and $\Lambda_{AB}(t)$ do depend on initial frequency correlations. However, as none of the decoherence functions depend on the environment's coherences, the open-system dynamics is identical with classical and quantum frequency correlations.

If $\Delta n_A t_A(t) = \Delta n_B t_B(t)$ and the frequencies are perfectly correlated, i.e., $f_A = f_B$, we get $\Lambda_{AB}(t) = 1$. Hence, the Bell states $|\Psi^\pm\rangle$ do not experience dephasing, and we have the *decoherence-free subspace (DFS)* $\mathbf{S}_\Psi = \mathrm{span}\big(\{|HV\rangle, |VH\rangle\}\big)$. If $\Delta n_A t_A(t) = \Delta n_B t_B(t) = \Delta n t$ and the frequencies are perfectly *anti*correlated, i.e., $f_A + f_B = f_0$, we get $\kappa_{AB}(t) = e^{i2\pi f_0 \Delta n t}$. Although this decoherence function is not a constant, it preserves the trace distance of the Bell states $|\Phi^\pm\rangle$. In this sense, we have the DFS $\mathbf{S}_\Phi = \mathrm{span}\big(\{|HH\rangle, |VV\rangle\}\big)$. With no frequency correlations at all, i.e., when $|g(f_A,f_B)|^2 = |g_A(f_A)|^2|g_B(f_B)|^2$, we get $\kappa_{AB}(t) = \kappa_A(t)\kappa_B(t)$, $\Lambda_{AB}(t) = \kappa_A(t)\kappa_B(t)^*$, and $\Phi^t_{AB} = \Phi^t_A \otimes \Phi^t_B$.

4.1.2 The bivariate Gaussian

Above, we only dealt with the extreme cases of initial frequency correlations. Because perfectly (anti)correlated frequencies are hard to produce experimentally, it

[1] We will show how to get around this limitation in Chapter 5.

is meaningful to see how different cases in-between affect the biphoton dephasing. The bivariate Gaussian spectrum provides one analytically simple and experimentally realizable way to do so [40; 41; 48; 49; 114; 115; 116]. Using the vectors $\vec{f} = (f_A, f_B)^T$, $\langle\vec{f}\rangle = (\langle f_A\rangle, \langle f_B\rangle)^T$, and the *covariance matrix* $C_{jk} = \langle f_j f_k\rangle - \langle f_j\rangle\langle f_k\rangle$, $j, k = A, B$, the bivariate Gaussian can be written as

$$|g(f_A, f_B)|^2 = \frac{1}{2\pi\sqrt{\det C}} e^{-\frac{1}{2}(\vec{f}-\langle\vec{f}\rangle)^T C^{-1}(\vec{f}-\langle\vec{f}\rangle)}. \tag{4.11}$$

For simplicity, we assume the same mean frequency μ and variance σ^2 for both of the photons, i.e., $\langle f_A\rangle = \langle f_B\rangle = \mu$ and $C_{AA} = C_{BB} = \sigma^2$. The *correlation coefficient* $K = C_{AB}/C_{AA} \in [-1, 1]$ quantifies the initial frequency correlations, with $K = -1$ meaning perfect anticorrelation and $K = 1$ perfect correlation. Furthermore, assuming $g(f_A, f_B) = |g(f_A, f_B)|$, K is related to the concurrence of the pure frequency state $|\xi\rangle = \int df_A df_B g(f_A, f_B)|f_A f_B\rangle$ via

$$\mathcal{C}(\xi) = \sqrt{2\big(1 - \sqrt{1 - K^2}\big)}. \tag{4.12}$$

Note that this only holds for *pure* states [satisfying $g(f_A, f_B) = |g(f_A, f_B)|$]. By mixing pure frequency states having the same frequency distribution but different phases, we can keep K fixed while reducing the total state's concurrence. This explains the polarization dynamics not distinguishing between classical and quantum correlations.

Under the above assumptions, Eq. (4.11) can be alternatively written as

$$|g(f_A, f_B)|^2 = \frac{1}{2\pi\sigma^2\sqrt{1 - K^2}} e^{-\frac{(f_A-\mu)^2 - 2K(f_A-\mu)(f_B-\mu) + (f_B-\mu)^2}{2\sigma^2(1-K^2)}}. \tag{4.13}$$

This form may look ill-behaving at $K \to \pm 1$, but we can write the spectrum also as

$$|g(f_A, f_B)|^2 = \frac{1}{\sqrt{2\pi\sigma^2(1+K)}} e^{-\frac{(f_A+f_B-2\mu)^2}{4\sigma^2(1+K)}} \frac{1}{\sqrt{2\pi\sigma^2(1-K)}} e^{-\frac{(f_A-f_B)^2}{4\sigma^2(1-K)}}. \tag{4.14}$$

If we now take the limits, we get

$$\lim_{K\to-1} |g(f_A, f_B)|^2 = \delta(f_A + f_B - 2\mu) \frac{1}{\sqrt{2\pi\sigma^2}} e^{-\frac{(f_A-f_B)^2}{8\sigma^2}}, \tag{4.15}$$

$$\lim_{K\to1} |g(f_A, f_B)|^2 = \frac{1}{\sqrt{2\pi\sigma^2}} e^{-\frac{(f_A+f_B-2\mu)^2}{8\sigma^2}} \delta(f_A - f_B). \tag{4.16}$$

Eq. (4.15) is nonzero only at $f_A + f_B - 2\mu = 0$. Substituting either $f_A = 2\mu - f_B$ or $f_B = 2\mu - f_A$ in it, we get the Gaussian margin $|g_j(f_j)|^2 = \exp\Big[-\frac{1}{2}\big(\frac{f_j-\mu}{\sigma}\big)^2\Big]/\sqrt{2\pi\sigma^2}$, $j = A, B$. This means that, individually, the two frequencies

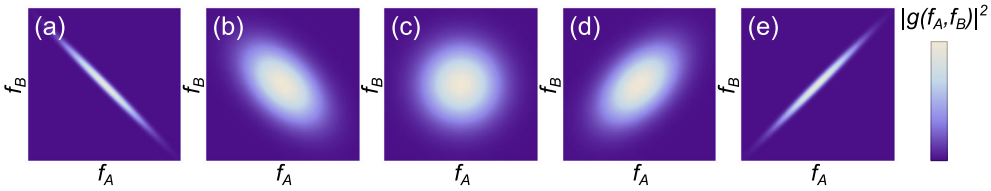

Figure 4.1. The bivariate Gaussian frequency disribution. (a) $K = -0.99$, (b) $K = -0.50$, (c) $K = 0.00$, (d) $K = 0.50$, (e) $K = 0.99$

seem random, as they are determined by the marginal distributions. But when compared with each other, one observes that $f_A + f_B = 2\mu$. Similar reasoning goes with Eq. (4.16), the correlated case.

Anticorrelated frequencies naturally arise from SPDC. However, it can be quite challenging to fully satisfy the phase matching condition in an actual experiment. The joint frequency spectrum of the signal and idler photons can be approximated by the bivariate Gaussian with K close to, but not exactly -1. Here, the frequency of the pump laser is 2μ. K can then be tuned, e.g., with interference filters (IFs [117]) or by controlling the pump laser's *phase matching function* [118]. The phase matching function depends on the nonlinear crystal's length, and positive correlations—even $K \approx 1$—can be achieved with very long crystals. The bivariate Gaussian has been plotted in Fig. 4.1 with different values of K.

It is interesting to notice that the sign of correlations is the opposite in time domain. Furthermore, perfectly (anti)correlated photons are *delocalized* in time. However, detecting one photon immediately localizes the other, as we will next show for the special case of $g(f_A, f_B) = |g(f_A, f_B)|$. This result will have a small part to play in Chapter 5.

The probability amplitude for the pair of arrival times (s_A, s_B) is obtained as the Fourier transform of $g(f_A, f_B)$,

$$\hat{g}(s_A, s_B) = \int df_A df_B g(f_A, f_B) e^{-i(2\pi f_A s_A + 2\pi f_B s_B)} \tag{4.17}$$

$$= \sqrt{8\pi\sigma^2\sqrt{1-K^2}} e^{-(2\pi\sigma)^2(s_A^2 + 2K s_A s_B + s_B^2) - i2\pi\mu(s_A+s_B)}. \tag{4.18}$$

The corresponding probability distribution is then

$$|\hat{g}(s_A, s_B)|^2 = 8\pi\sigma^2\sqrt{1-K^2} e^{-2(2\pi\sigma)^2(s_A^2 + 2K s_A s_B + s_B^2)}. \tag{4.19}$$

Here we see the opposite sign of K for the arrival times. The margins of Eq. (4.19) are given by

$$|\hat{g}(s_j)|^2 = \sqrt{8\pi\sigma^2(1-K^2)} e^{-2(2\pi\sigma)^2(1-K^2)s_j^2}. \tag{4.20}$$

The marginal distribution becomes infinitely wide as $K \to \pm 1$, which means that, if neither of the photons has been detected, it is equally probable to detect one at *any*

point of time. That is, the photons are temporally delocalized. Finally, the probability distribution for the arrival time of photon A, conditioned on photon B having been detected at $s_B = S_B$, is

$$|\hat{g}(s_A|s_B = S_B)|^2 = \frac{|\hat{g}(s_A, S_B)|^2}{|\hat{g}(S_B)|^2} \tag{4.21}$$

$$= \sqrt{8\pi\sigma^2} e^{-2(2\pi\sigma)^2(s_A + K S_B)^2}, \tag{4.22}$$

which is clearly localized in time. Note that the arrival times are interchangeable.

4.1.3 Hybrid entanglement

With single-photon dephasing, we obtained a very simple expression for the concurrence dynamics describing the open system becoming entangled with its environment [see Eq. (3.32)]. With biphoton dephasing, describing entanglement becomes more complex because we, in fact, have *four* parties altogether—two polarization degrees of freedom and two frequency degrees of freedom—and there is no entanglement measure for N-partite systems with $N > 2$. One should therefore divide the total system in half from somewhere. With biphoton dephasing, an obvious choice would be to have the polarization qubits on one side (the open system) and the frequency states on the other (the environment). The concurrence of this bipartition is inversely proportional to the purity of Eq. (4.7),

$$\begin{aligned}\mathcal{P}\big(\rho_{AB}(t)\big) = 1 &- 2\big(|C_{HH}|^2|C_{VH}|^2 + |C_{HV}|^2|C_{VV}|^2\big)\big[1 - |\kappa_A(t)|^2\big] \\ &- 2\big(|C_{HH}|^2|C_{HV}|^2 + |C_{VH}|^2|C_{VV}|^2\big)\big[1 - |\kappa_B(t)|^2\big] \\ &- 2|C_{HH}|^2|C_{VV}|^2\big[1 - |\kappa_{AB}(t)|^2\big] \\ &- 2|C_{HV}|^2|C_{VH}|^2\big[1 - |\Lambda_{AB}(t)|^2\big].\end{aligned} \tag{4.23}$$

From Eq. (4.23) we see that, in this case too, the open system does become entangled with its environment—unless the initial open-system state is given in a DFS.

An alternative bipartition would be that between Alice and Bob, i.e., having Alice's polarization and frequency on one side and Bob's on the other. Because the unitaries are local, the concurrence with this bipartition is constant in time and fully determined by the initial probability amplitudes. We now make an interesting observation. Say, the initial polarization state is one of the Bell states and the frequencies are uncorrelated. After full dephasing, we have either the classical polarization state $\mathrm{diag}(1/2, 0, 0, 1/2)$ or $\mathrm{diag}(0, 1/2, 1/2, 0)$, and the bipartite frequency state can still be written as a convex combination of product states. Thus, if we restrict to polarization or frequency alone, the entanglement cannot be detected. Yet, Alice's photon *is* entangled with Bob's photon due to the initial amplitudes. We call such entanglement, "shared" by different degrees of freedom (in our case, biphoton polarization and frequency), *hybrid entanglement* [119].

In general, many features of open-system dynamics become much more nuanced with two (or more) qubits. In the next Section, for example, we return to non-Markovianity and information backflow and ponder the question, *where does the information flow back into with two qubits?*

4.2 Controlling the dynamics with initial system-environment correlations

The system and environment in the initial biphoton state (4.4) were uncorrelated. Initial system-environment correlations can be introduced, e.g., by making the simple substitution $|\lambda_j\rangle|f_j\rangle \mapsto e^{i\theta_{\lambda_j}(f_j)}|\lambda_j\rangle|f_j\rangle$. Doing so, we obtain the new decoherence functions

$$\kappa_j(t) = \int df_j |g_j(f_j)|^2 e^{i[\theta_j(f_j)+2\pi f_j \Delta n_j t_j(t)]}, \tag{4.24}$$

$$\kappa_{AB}(t) = \int df_A df_B |g(f_A,f_B)|^2 e^{i[\theta_A(f_A)+2\pi f_A \Delta n_A t_A(t)+\theta_B(f_B)+2\pi f_B \Delta n_B t_B(t)]}, \tag{4.25}$$

$$\Lambda_{AB}(t) = \int df_A df_B |g(f_A,f_B)|^2 e^{i[\theta_A(f_A)+2\pi f_A \Delta n_A t_A(t)-\theta_B(f_B)-2\pi f_B \Delta n_B t_B(t)]}, \tag{4.26}$$

where we have defined $\theta_j(f_j) := \theta_{H_j}(f_j) - \theta_{V_j}(f_j)$. These kinds of frequency-dependent phase functions can be imprinted on photons with *spatial light modulators (SLMs* [47]*)*. In this Section, we focus on biphoton dephasing influenced by three different phase functions.

4.2.1 Memory partitions

With single-qubit dephasing, the connection between non-Markovianity and information backflow was quite clear; With a non-Markovian channel, information backflow showed as any pair of initial states with different coherences becoming momentarily more distinguishable. With two-qubit dephasing, we have two local and two nonlocal decoherence functions, which makes the issue with information backflow more subtle—though distinguishing between Markovian and non-Markovian channels is still simple; If the absolute value of even one of the decoherence functions behaves nonmonotonically, we can find an initial state pair with nonmonotonic trace distance. Such dynamics is then declared non-Markovian by the BLP definition, regardless of the initial state pair maximizing the revivals of trace distance. However, it is now reasonable to ask, *where does the information flow back into?* To answer this question, we introduce the concept of "memory partitions".

With the two-qubit Hilbert space $\mathcal{H}_{AB}$, we have the subspaces $\mathbf{S}_A = \operatorname{span}\big(\{|H_A\rangle,$

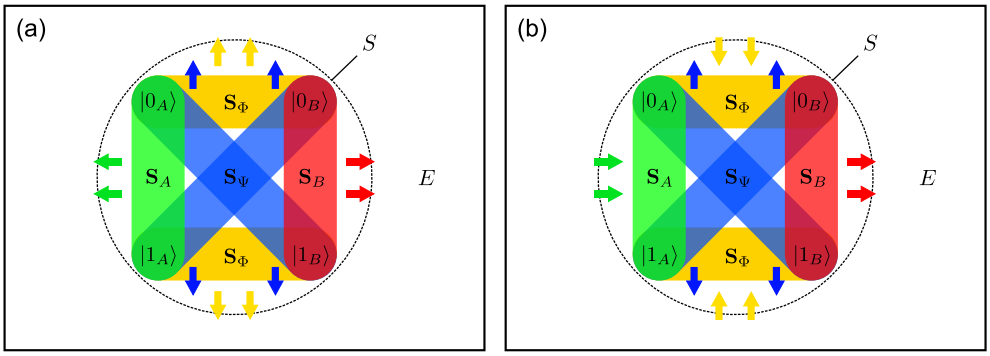

Figure 4.2. A schematic picture of the two-qubit subspaces and the example memory partition $\langle 1,0,1,0\rangle$. The arrows indicate the direction of possible information flow. (a) As the open system S starts interacting with its environment E, information may flow from the system into the environment (with any DFS, we have no information flow). (b) At some later time intervals, we may have information backflow into the subspaces $\mathbf{S}_A$ and $\mathbf{S}_\Phi$ (possibly at different time intervals).

$|V_A\rangle\}\big)$, $\mathbf{S}_B = \mathrm{span}\big(\{|H_B\rangle, |V_B\rangle\}\big)$, $\mathbf{S}_\Psi$, and $\mathbf{S}_\Phi$, all of whose dynamics is governed by single, different decoherence function. If the absolute value of some of the decoherence functions behaves nonmonotonically, state pairs in the associated subspace, with different initial coherences, may become temporarily more distinguishable. Thus, we interpret information flowing back to that specific subspace. With the local subspaces $\mathbf{S}_A = \mathcal{H}_A$ and $\mathbf{S}_B = \mathcal{H}_B$, we are actually considering the (non-)Markovianity of the local channels

$$\Phi^t_{A(B)}\big(\rho(0)\big) = \mathrm{tr}_{B(A)}\big[\Phi^t_{AB}\big(\rho(0)\big)\big], \tag{4.27}$$

where we have included Bob's (Alice's) polarization to Alice's (Bob's) environment[2].

We call the quadruplets $\langle \mathbf{S}_A, \mathbf{S}_B, \mathbf{S}_\Phi, \mathbf{S}_\Psi\rangle$ memory partitions, as they indicate where the channel Φ^t_{AB} displays memory effects; We write 0 in the place of "Markovian subspaces" and 1 in the place of "non-Markovian subspaces". For example, the partition $\langle 1,0,1,0\rangle$ means that Alice's local channel is non-Markovian, Bob's local channel is Markovian, the total channel restricted to $\mathbf{S}_\Phi$ is non-Markovian, whereas the total channel restricted to $\mathbf{S}_\Psi$ is again Markovian (see Fig. 4.2).

With four subspaces, we have $2^4 = 16$ memory partitions, and our linear optical model allows us to create all of them. Here, $\kappa_A(t)$ governs the dephasing dynamics in $\mathbf{S}_A$, $\kappa_B(t)$ in $\mathbf{S}_B$, $\kappa_{AB}(t)$ in $\mathbf{S}_\Phi$, and $\Lambda_{AB}(t)$ in $\mathbf{S}_\Psi$, and we can control their monotonicity by engineering the initial frequency correlations given by K and system-environment correlations given by $\theta_j(f_j)$. The two phase functions we need

[2]Where the bound between the system and environment is drawn is called the "Heisenberg cut" [120].

are the zigzag function

$$z(f,\alpha) = \arcsin\Big[\sin\Big(\alpha\frac{f-\mu}{\sigma}\Big)\Big] \tag{4.28}$$

and the quadratic

$$q(f,\beta) = \beta\Big(\frac{f-\mu}{\sigma}\Big)^2. \tag{4.29}$$

Whenever these phases are implemented, we have initial system-environment correlations, and the respective decoherence functions satisfy $|\kappa(0)| < 1$. However, if we also have $|\kappa(t)| < |\kappa(0)|\ \forall t$, we obtain proper quantum channels by normalizing them, $\tilde{\kappa}(t) = \kappa(t)/\kappa(0)$.

We now assume equal and overlapping interaction times, so we can simply write $t_A(t) = t_B(t) = t$ in Eqs. (4.24)–(4.26). We also assume that $\Delta n_A = \Delta n_B = \Delta n$ and use the shorthand notations $\eta = \mu/\sigma$ and $\tau = 2\pi\sigma\Delta n t$. By substituting the bivariate Gaussian distribution and the phase functions $\theta_j(f_j) = z(f_j,\alpha_j)$ in Eqs. (4.24)–(4.26), we get the local decoherence functions

$$\begin{aligned}\kappa_j(\tau) = e^{i\eta\tau}\Bigg\{&\frac{2}{\pi}e^{-\frac{1}{2}\tau^2} + \frac{2}{\pi}\sum_{k=1}^{\infty}\frac{(-1)^k}{1-4k^2}\Big[e^{-\frac{1}{2}(\tau-2k\alpha_j)^2} + e^{-\frac{1}{2}(\tau+2k\alpha_j)^2}\Big]\\ &- \frac{1}{2}\Big[e^{-\frac{1}{2}(\tau-\alpha_j)^2} - e^{-\frac{1}{2}(\tau+\alpha_j)^2}\Big]\Bigg\}\end{aligned} \tag{4.30}$$

and nonlocal decoherence functions with long, not particularly illuminating forms (see Publication **I**). From Eq. (4.30) we see that the local decoherence functions' magnitudes consist of Gaussian "recoherence peaks" centered at $\tau = \pm\alpha_j$ and $\tau = \pm 2k\alpha_j$, $k = 1, 2, 3, ...$ Hence, we can control the non-Markovian time intervals by tuning α_j. The zigzag phase is used, whenever we want to target the corresponding local subspace $\mathbf{S}_j$ with memory effects.

With the quadratic phase functions $\theta_j(f_j) = q(f_j,\beta_j)$, we obtain the decoherence functions

$$\kappa_j(\tau) = \sqrt{\frac{i}{2\beta_j + i}}e^{i\left(\eta\tau - \frac{1}{2(2\beta_j+i)}\tau^2\right)}, \tag{4.31}$$

$$\kappa_{AB}(\tau) = \sqrt{\frac{1}{1-4\beta_A\beta_B(1-K^2)+i2(\beta_A+\beta_B)}}e^{i2\eta\tau - \frac{1+K+i(\beta_A+\beta_B)(1-K^2)}{1-4\beta_A\beta_B(1-K^2)+i2(\beta_A+\beta_B)}\tau^2}, \tag{4.32}$$

$$\Lambda_{AB}(\tau) = \sqrt{\frac{1}{1+4\beta_A\beta_B(1-K^2)+i2(\beta_A-\beta_B)}}e^{-\frac{1-K+i(\beta_A-\beta_B)(1-K^2)}{1+4\beta_A\beta_B(1-K^2)+i2(\beta_A-\beta_B)}\tau^2}. \tag{4.33}$$

Table 4.1. Memory partitions, frequency distributions, and phase functions.

Fig. 4.3 panel	$\langle \mathbf{S_A}, \mathbf{S_B}, \mathbf{S_\Phi}, \mathbf{S_\Psi} \rangle$	$\lvert \mathbf{g}(\mathbf{f_A}, \mathbf{f_B}) \rvert^2$	$\theta_\mathbf{A}(\mathbf{f_A})$	$\theta_\mathbf{B}(\mathbf{f_B})$
(a)	$\langle 0,0,0,0 \rangle$	$G(0)$	constant	constant
(b)	$\langle 1,0,0,0 \rangle$	$G(0)$	$z(f_A,5)$	constant
(c)	$\langle 0,1,0,0 \rangle$	$G(0)$	constant	$z(f_B,5)$
(d)	$\langle 0,0,1,0 \rangle$	$[G(-1)+G(1)]/2$	$q(f_A,3)$	$q(f_B,3)$
(e)	$\langle 0,0,0,1 \rangle$	$[G(-1)+G(1)]/2$	$q(f_A,3)$	$q(f_B,-3)$
(f)	$\langle 1,1,0,0 \rangle$	$[G(-1)+G(1)]/2$	$z(f_A,5)$	$z(f_B,-5)$
(g)	$\langle 1,0,1,0 \rangle$	$G(1)$	$z(f_A,5)$	constant
(h)	$\langle 1,0,0,1 \rangle$	$G(-1)$	$z(f_A,5)$	constant
(i)	$\langle 0,1,1,0 \rangle$	$G(1)$	constant	$z(f_B,5)$
(j)	$\langle 0,1,0,1 \rangle$	$G(-1)$	constant	$z(f_B,5)$
(k)	$\langle 0,0,1,1 \rangle$	$[G(-1)+G(1)]/2$	$q(f_A,3)$	constant
(l)	$\langle 1,1,1,0 \rangle$	$G(1)$	$z(f_A,5)$	$z(f_B,-15)$
(m)	$\langle 1,1,0,1 \rangle$	$G(-1)$	$z(f_A,5)$	$z(f_B,-15)$
(n)	$\langle 1,0,1,1 \rangle$	$G(0)$	$z(f_A,5)$	$q(f_B,3)$
(o)	$\langle 0,1,1,1 \rangle$	$G(0)$	$q(f_A,3)$	$z(f_B,5)$
(p)	$\langle 1,1,1,1 \rangle$	$G(0)$	$z(f_A,5)$	$z(f_B,5)$

We use the quadratic phase functions in two occasions: First, when we want to introduce *only* nonlocal memory effects and keep the local dynamics Markovian, and secondly, when the only Markovian subspace is one of the local subspaces. In the first case, we also use a balanced mixture of frequency-correlated and frequency-anticorrelated spectrum.

When we remember that $K = 0$ factorizes the nonlocal decoherence functions and that $K = \pm 1$ gives Markovian DFSs—the trace-distance dynamics in DFSs is constant, i.e., monotonic—we have all the tools to construct the 16 linear optical memory partitions. The memory partitions are listed in Table 4.1 together with the corresponding frequency distributions and phase functions. A bivariate Gaussian frequency distribution with the correlation coefficient K is written as $G(K)$. The α_j and β_j parameters given in the table are just examples. However, they need to be selected carefully, as some values might result in non-CP dynamics. The matching decoherence functions have been plotted in Fig. 4.3.

Few comments regarding some of the partitions are now in order. With $\langle 1,0,0,0 \rangle$ and $\langle 0,1,0,0 \rangle$, the nonlocal decoherence functions are actually nonmonotonic. However, as $|\kappa_{B(A)}(\tau)| \approx 0$ when $|\kappa_{A(B)}(\tau)|$ increases, the revivals of $|\kappa_{AB}(\tau)|$ and $|\Lambda_{AB}(\tau)|$ are negligibly small—both being products of $|\kappa_A(\tau)|$ and $|\kappa_B(\tau)|$—and they can be forced even smaller by increasing $\alpha_{A(B)}$.

The mixed distribution $[G(-1)+G(1)]/2$ provides a nice way to partially protect all nonlocal coherences and hence the so-called "X-states" [121]. This is the

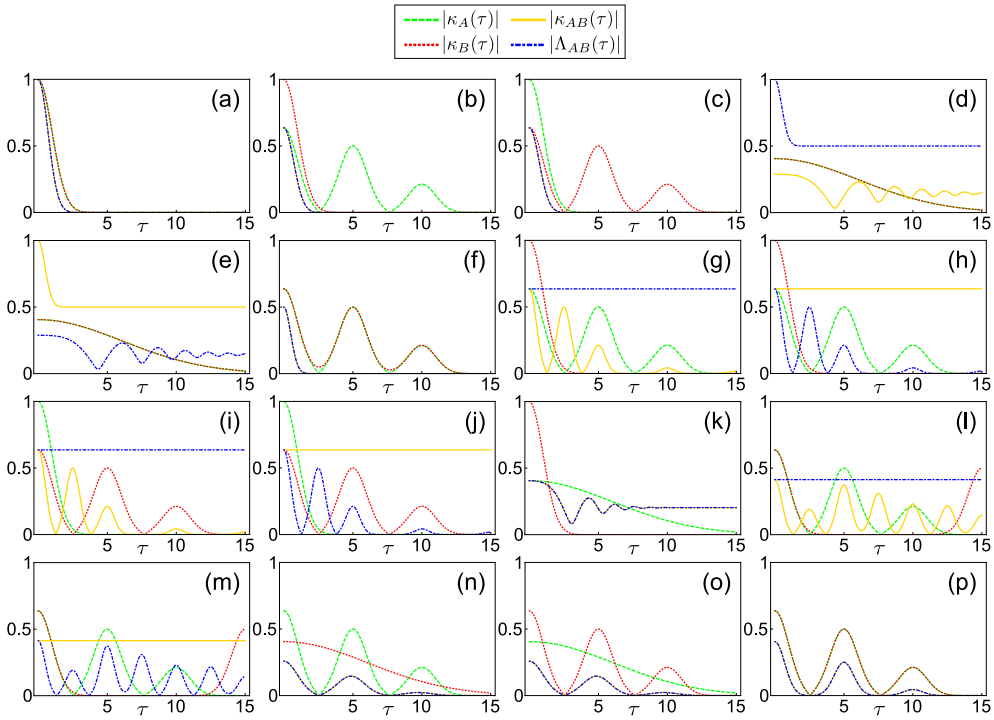

Figure 4.3. Absolute values of the decoherence functions given in Table 4.1 as functions of the scaled (and unitless) interaction time τ.

case with the memory partitions $\langle 0,0,1,0\rangle$, $\langle 0,0,0,1\rangle$, and $\langle 0,0,1,1\rangle$, but interestingly not with $\langle 1,1,0,0\rangle$. Here, the nonlocal coherences die very quickly due to the opposite-sign α_j parameters in the zigzag phases. It is also worth mentioning that the partitions $\langle 0,0,1,0\rangle$, $\langle 0,0,0,1\rangle$, and $\langle 0,0,1,1\rangle$ are in contrast to conventional wisdom; Usually, enlarging the system of interest drives the dynamics more towards the Markovian regime [24; 122; 123].

Finally, $\langle 1,0,1,1\rangle$ and $\langle 0,1,1,1\rangle$ could, in fact, be achieved with constant phases instead of the quadratic phases. However, as the quadratic phases prolong the local coherence times, the nonlocal recoherence peaks become more distinct.

The number of different decoherence functions and memory partitions grows rapidly with the number of qubits. If there are no uncorrelated frequency pairs, the dephasing dynamics of an N-qubit system is described by $M = (3^N - 1)/2$ independent decoherence functions, which means 2^M different memory partitions. The factor of $3^N - 1$ comes from the fact that the terms $\theta_j(f_j) + 2\pi f_j \Delta n_j t_j(t)$ in the decoherence functions can be multiplied by -1, 0, or 1, but not all by 0 [cf. Eqs. (4.24)–(4.26)]. We divide $3^N - 1$ by two to account for complex conjugates; $\kappa(t)$ and $\kappa(t)^*$ are essentially the same decoherence function.

Memory partitions have both fundamental and information technological impli-

cations. With the memory partition $\langle j_1, j_2, ..., j_M \rangle$, the fraction $\sum_{k=1}^{M} j_k/M$ quantifies how common information backflow is in a multipartite open quantum system. In addition, the number of decoherence functions exceeding the dimension of the open system's Hilbert space at $d_S > 4$ makes the memory partitions a tempting alternative to convey information with. With an N-qubit system, one could encode M bits of information to the system's dephasing dynamics by selecting the monotonic (0) and nonmonotonic (1) decoherence functions. Note that this would not violate the *Holevo's theorem* of N qubits transmitting at most N bits of information [70], since we would be dealing with *global* N-qubit dynamics instead of the system's state at some single point of (interaction) time. Accordingly, the decoding protocol would require at least two measurement points, were it not possible to decode a snapshot of the system's evolution[3]. However, even with a single measurement point, the decoding protocol would quickly become quite laborious; From Chapter 2, we remember that it takes 6^N measurements to determine the state of an N-qubit system. Furthermore, it remains to be shown whether a generic strategy of creating—or even simulating—any N-qubit memory partition exists.

4.2.2 Reverse decoherence and hidden nonlocality

Decoherence degrades quantum to classical by destroying the coherences of an open quantum system, but is it possible to go to the other direction and have "reverse decoherence", i.e., start from a fully classical state and reach maximum coherences at some later point of time? With proper phase functions, *yes*.

Maximum coherences mean a pure state, and maximum coherences can be obtained with unit decoherence functions. The decoherence functions (4.24)–(4.26) become 1 at some point of time $t = T$, when

$$\theta_j(f_j) = -2\pi f_j \Delta n_j t_j(T). \tag{4.34}$$

At $t = T$, all the phases overlap and there is nothing to be averaged over. Different phase functions and the corresponding biphoton decoherence functions are plotted in Fig. 4.4, when $\Delta n_A t_A(t) = \Delta n_B t_B(t)$ and we have uncorrelated, yet equal Gaussian frequency distributions.

It is important to note a few things. First, reverse decoherence cannot be described by a CPTP map. Alternatively, the domain of initial states should be restricted. Secondly, phase functions given by Eq. (4.34) reverse (pure) decoherence with *any* number of photons—purifying *any* N-qubit state and hence going beyond DFSs. However, if the system-environment interaction proceeds after $t = T$, we have "normal" decoherence and the coherences eventually disappear (see Fig. 4.4). And finally, reversing decoherence like this highly depends on the type of noise and

[3] We will deal with a special case of such snapshot measurements in Chapter 6.

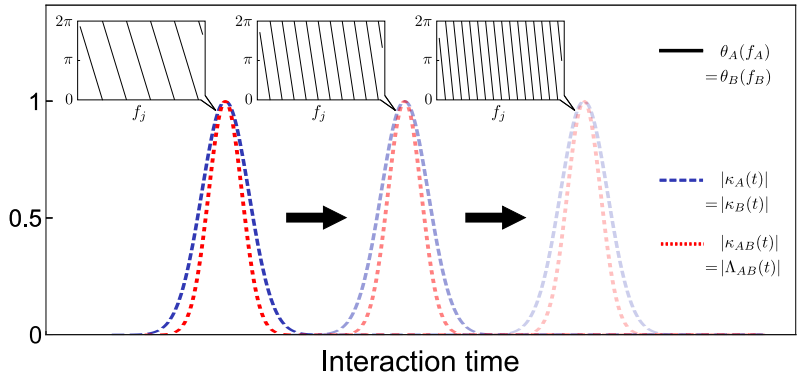

Figure 4.4. Reverse decoherence. The steeper the phase functions, the further in time we can move the instant of maximum coherences. For simplicity, we have only considered two qubits, overlapping interaction times, and the bivariate Gaussian with $K = 0$.

its duration being known and the initial system-environment correlations being fully accessible. These are extremely heavy assumptions, which means that, for now, our linear optical system serves as a proof-of-principle model—nevertheless providing an intriguing and effective way to fight decoherence with decoherence itself.

In certain cases, reverse decoherence can also be understood in terms of *hidden nonlocality*. Hidden nonlocality means initially undetectable entanglement that can be activated by local filtering [124; 125; 126; 127]. This is exactly what happens, when a hybrid-entangled initial state is subjected to local dephasing. That is, when we have, e.g., $C_{HV} = C_{VH} = 1/\sqrt{2}$ and $t_j \gg 0$, and the frequency spectra are not perfectly correlated; The open system, initially in the classical state $\mathrm{diag}(0, 1/2, 1/2, 0)$, becomes the Bell state $|\Psi^+\rangle$ after local dephasing of the durations t_j. Note that our "filters", i.e., the local unitaries $U_j(t)$, do not actually filter anything out.

We tested reverse decoherence by purifying all the Bell states with dephasing. These experiments will be described shortly, as they can be applied in noisy quantum teleportation.

4.3 Noisy quantum teleportation

We now come to one of the most fascinating applications of quantum theory, and in particular, quantum entanglement: quantum teleportation. The basic teleportation protocol goes as follows [73]. Alice has a qubit in some unknown state $|\phi\rangle = \alpha|0\rangle + \beta|1\rangle$, which she wishes to teleport to Bob. In view of this task, Alice and Bob have shared a bipartite auxiliary state, which is one of the maximally entangled Bell states. Alice performs a Bell-state measurement (BSM) on the state being teleported and her part of the auxiliary state. As a result, the measured pair becomes entangled, erasing

the initial entanglement between Alice and Bob. Alice reports which Bell state she obtained to Bob, who operates with a matching unitary on his qubit. Finally, the state of Bob's qubit becomes $|\phi\rangle$.

The basic protocol assumes ideal conditions, i.e., no noise. In this Section, we consider a more realistic scenario: quantum teleportation with the auxiliary state experiencing dephasing noise. An obvious strategy for Alice and Bob would be to first prepare the auxiliary state appropriately (i.e., hide its nonlocality with proper phase functions), then fully purify it with reverse decoherence, and finally proceed with the basic protocol when they are in possession of a pure Bell state. However, the auxiliary state's nonlocality *need not be fully activated for quantum teleportation to work*. That is, there can still be noise on Bob's side *after* Alice's BSM. Next, we will go through the steps of this reordered protocol.

4.3.1 Theoretical description

The state to be teleported is $|\phi\rangle = \alpha|H\rangle + \beta|V\rangle$ and the auxiliary state shared by Alice and Bob is given by Eq. (4.7) with the polarization amplitudes $C_{HV} = C_{VH} = 1/\sqrt{2}$, decoherence functions (4.24)–(4.26), and phase functions $\theta_j(f_j) = -2\pi f_j \Delta n_j t_j$. We remind that $t_{A(B)}$ is the total interaction time on Alice's (Bob's) side. The initial bipartite polarization state reads

$$\rho_{AB}(0) = \frac{1}{2}\begin{pmatrix} 0 & 0 & 0 & 0 \\ 0 & 1 & \Lambda_{AB}(0) & 0 \\ 0 & \Lambda_{AB}(0)^* & 1 & 0 \\ 0 & 0 & 0 & 0 \end{pmatrix}, \tag{4.35}$$

where $\Lambda_{AB}(t) = \int df_A df_B |g(f_A, f_B)|^2 \exp\{i[2\pi f_A \Delta n_A (t_A(t) - t_A) - 2\pi f_B \Delta n_B (t_B(t) - t_B)]\}$. With $t_j \gg 0$ and the reasonable assumption that the frequencies are not perfectly correlated[4], we obtain the approximate, (seemingly) local form $\rho_{AB}(0) \approx (|HV\rangle\langle HV| + |VH\rangle\langle VH|)/2$ [see Fig. 4.5(a)].

Alice subjects her auxiliary photon to polarization dephasing by sending it through a birefringent crystal with the birefringence Δn_A and length ct_A [5] [Fig. 4.5(b)]. Because we still have $t_B \gg 0$, nonlocality in the auxiliary state $\rho_{AB}(t_A) \approx (|HV\rangle\langle HV| + |VH\rangle\langle VH|)/2$ is still hidden. Now, the total polarization-frequency state of the *three* photons is, omitting the frequency of the photon whose polarization state is being teleported,

$$|\Psi_3(t_A)\rangle = \frac{1}{\sqrt{2}}|\phi\rangle\big(|HV\rangle|\xi_{HV}(t_A)\rangle + |VH\rangle|\xi_{VH}(t_A)\rangle\big), \tag{4.36}$$

[4] Here, we make no other assumptions regarding the frequency distribution.

[5] c is the speed of light in vacuum.

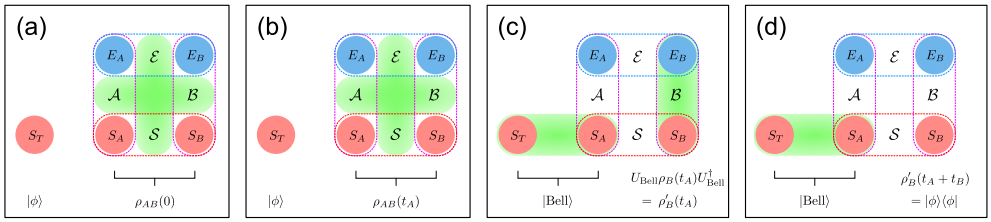

Figure 4.5. The stages of noisy quantum teleportation. $\mathcal{S}$ = the open system consisting of Alice and Bob's polarization qubits, S_A and S_B. S_T = the system carrying the state being teleported, $|\phi\rangle$. $\mathcal{E}$ = the environment consisting of Alice and Bob's frequencies, E_A and E_B. $\mathcal{A}$ ($\mathcal{B}$) = Alice's (Bob's) photon. The green ovals represent (hybrid) entanglement. (a) Alice and Bob have prepared a hybrid-entangled total state. Their open system is in the classical state $\rho_{AB}(0)$. (b) Alice subjects her photon to dephasing noise, making the bipartite polarization state $\rho_{AB}(t_A)$, which is still classical. (c) Alice performs BSM on her photons—converting the hybrid entanglement into entanglement between S_T and S_A, and S_B and E_B—and Bob operates with a matching unitary U_{Bell} on his local polarization state, $\rho_B(t_A)$. (d) Bob converts the S_B–E_B entanglement into coherences by subjecting his photon to dephasing noise and obtains the state $|\phi\rangle$.

where $|\xi_{\lambda_A\lambda_B}(t_A)\rangle = \int df_A df_B g(f_A, f_B) \exp\{i[\theta_{\lambda_A}(f_A) + 2\pi f_A n_{\lambda_A} t_A + \theta_{\lambda_B}(f_B)]\} |f_A f_B\rangle$. Note that, in Eq. (4.36), we have written the state being teleported first, then Alice's auxiliary qubit, and finally Bob's auxiliary qubit. Keeping the same order but having all the Bell states on Alice's side, $|\Psi_3(t_A)\rangle$ can be written as

$$\begin{aligned}
|\Psi_3(t_A)\rangle =& \frac{1}{2}|\Phi^+\rangle\Big[\beta|H\rangle|\xi_{VH}(t_A)\rangle + \alpha|V\rangle|\xi_{HV}(t_A)\rangle\Big] \\
&+\frac{1}{2}|\Phi^-\rangle\Big[-\beta|H\rangle|\xi_{VH}(t_A)\rangle + \alpha|V\rangle|\xi_{HV}(t_A)\rangle\Big] \\
&+\frac{1}{2}|\Psi^+\rangle\Big[\alpha|H\rangle|\xi_{VH}(t_A)\rangle + \beta|V\rangle|\xi_{HV}(t_A)\rangle\Big] \\
&+\frac{1}{2}|\Psi^-\rangle\Big[\alpha|H\rangle|\xi_{VH}(t_A)\rangle - \beta|V\rangle|\xi_{HV}(t_A)\rangle\Big].
\end{aligned} \tag{4.37}$$

Alice performs BSM on her pair of qubits and classically communicates her result $|\text{Bell}\rangle$ to Bob, who applies a matching unitary operation U_{Bell} on his qubit $\rho_B(t_A) = \text{tr}_A[\rho_{AB}(t_A)]$. The unitaries are

$$U_{\text{Bell}} = \begin{cases} \sigma_x \text{ for } |\text{Bell}\rangle = |\Phi^+\rangle, \\ i\sigma_y \text{ for } |\text{Bell}\rangle = |\Phi^-\rangle, \\ \mathbb{1} \text{ for } |\text{Bell}\rangle = |\Psi^+\rangle, \\ \sigma_z \text{ for } |\text{Bell}\rangle = |\Psi^-\rangle. \end{cases} \tag{4.38}$$

Now, Bob's polarization state is [Fig. 4.5(c)]

$$U_{\text{Bell}}\rho_B(t_A)U_{\text{Bell}}^\dagger = \begin{pmatrix} |\alpha|^2 & \alpha\beta^*\Lambda_{AB}(t_A) \\ \alpha^*\beta\Lambda_{AB}(t_A)^* & |\beta|^2 \end{pmatrix}. \tag{4.39}$$

Bob purifies the state (4.39) by guiding his photon through a birefringent crystal with the birefringence Δn_B and length ct_B. As $\Lambda_{AB}(t_A + t_B) = 1$, Bob's polarization state finally becomes $|\phi\rangle$ [Fig. 4.5(d)].

Here, we made the harmless assumptions that $0 = t_{i,A} < t_{f,A} = t_{i,B}$, i.e., the protocol starts simultaneously with Alice's interaction, and Bob's interaction starts immediately as Alice's ends. Surely, time passes in-between, but free evolution does not affect the polarization dynamics. Hence, in favor of simpler notation, we disregarded the time intervals of free evolution.

Interestingly, the biphoton polarization shared by Alice and Bob is never entangled, which is commonly required for quantum teleportation to work. This might suggest that quantum teleportation is possible with fully local resources. However, this is *not* the case, as the nonlocality of the biphoton polarization is actually just hidden—manifesting as hybrid polarization-frequency entanglement.

4.3.2 Experimental setups

In the experiments, we considered Bob's dephasing appearing both before and after Alice's BSM, separately. In the first case, we only purified the auxiliary Bell state(s). This was achieved by slightly modifying the experimental setup of the latter case, which is shown in Fig. 4.6 and goes as follows.

A combination of sandwich-like BBO+HWP+BBO (C-BBO) and BBO crystals is pumped by a femtosecond ultraviolet laser (390 nm, 76 MHz). The auxiliary photons are produced in C-BBO and sent to Alice and Bob. Most of the photons just impinge the C-BBO combination and continue to the BBO crystal, where a second SPDC takes place. Again, most of the photons just go through the crystal, but out of the produced photon pairs one carries the polarization state to be teleported—prepared by HWP2 and QWP2—and the other is used in coincidence counting.

The auxiliary photons' frequency modulations are composed of gratings (1200 l/mm), plano-convex cylindrical lenses (PCC lenses), beam displacers (BDs), HWPs at $45°$, and SLMs. Because the SLMs work in spatial domain, the gratings and PCC lenses are used to convert frequency to spatial degrees of freedom. Furthermore, because the SLMs are effective for horizontal polarization only [i.e., $\theta_{H,j}(f_j) = \theta_j(f_j)$, $\theta_{V,j}(f_j) = 0$], the BDs and HWPs are used to convert polarization to path (with horizontal polarization). The phase functions are then imprinted on the photons with SLMs that consist of 150 pixels, covering the photons' full width at half maximum (FWHM, approximately 3.5 nm). The mean wavelengths (λ_0 = 780 nm) are aligned to the middle of the SLM holograms.

In Fig. 4.6, example holograms are shown next to Alice and Bob's SLMs—Alice's hologram matching with approximately 1.5 mm of yttrium orthovanadate (YVO_4) and Bob's with 2 m of polarization maintaining single-mode fiber (PM fiber). The pixels in the middle of the holograms are used to imprint the phase func-

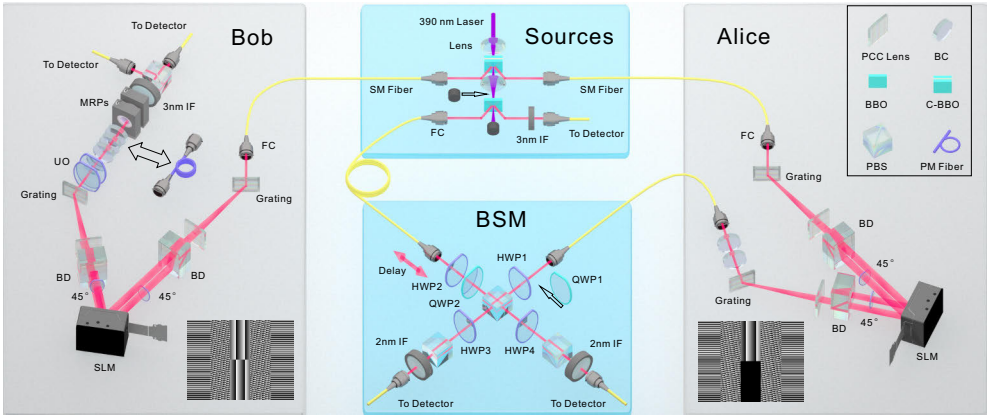

Figure 4.6. The experimental setups of noisy quantum teleportation and reverse decoherence. The setup of teleportation is composed of four parts: the photon sources, Alice and Bob's frequency modulations, and BSM. The sources include both a polarization entanglement source and a single-photon source. The auxiliary photons are distributed to Alice and Bob, whose SLMs are accompanied by example holograms in the picture. After the frequency modulations, Alice's auxiliary photon and one from the single-photon source combine in BSM. Bell-state purification with reverse decoherence is achieved by blocking the pump laser between C-BBO (sandwich-like BBO+HWP+BBO combination) and BBO (beta-barium borate) and inserting QWP1 (quarter-wave plate) in the setup. In this version of the experiment, we also use a PM fiber (polarization maintaining single-mode fiber) on Bob's side, emulating a more realistic scenario. HWP = half-wave plate, PCC lens = plano-convex cylindrical lens, BD = beam displacer, BC = birefringent crystal, MRP = motor rotating plate, PBS = polarizing beam splitter, UO = unitary operation, SM fiber = single-mode fiber, FC = fiber collimator.

tions. The other pixels resemble blazed grating and diffract excess photons to other angles. After the SLMs, the paths are recombined in the second HWPs and BDs, while the spatial degrees of freedom are converted back to frequency in the second PCC lenses and gratings.

The bipartite frequency modulation is followed by dephasing on Alice's side, BSM, and dephasing on Bob' side. Quartz or PM fiber is used on Bob's side, while YVO_4 is used on Alice's side; YVO_4 has a larger birefringence than quartz, making the thickness of YVO_4 thinner than that of quartz with the same interaction time, therefore easing BSM. The interaction time is controlled by adjusting the thickness of the crystals.

The BSM is carried out with HWP1, HWP3, HWP4, and three polarizing beam splitters (PBSs). When we measure the Bell states $|\Phi^{\pm}\rangle$, HWP1 is set to $0°$, and HWP3 and HWP4 to $\pm 22.5°$. With $|\Psi^{\pm}\rangle$, HWP1 is set to $45°$, and HWP3 and HWP4 to $\pm 22.5°$. To make the photonic identity better, we use IFs of FWHM = 2 nm in BSM. The unitary operation is composed of two HWPs that change according to Alice's Bell state. Bob uses motor rotating plates and a PBS to perform state tomography on his photons and receive the teleported state.

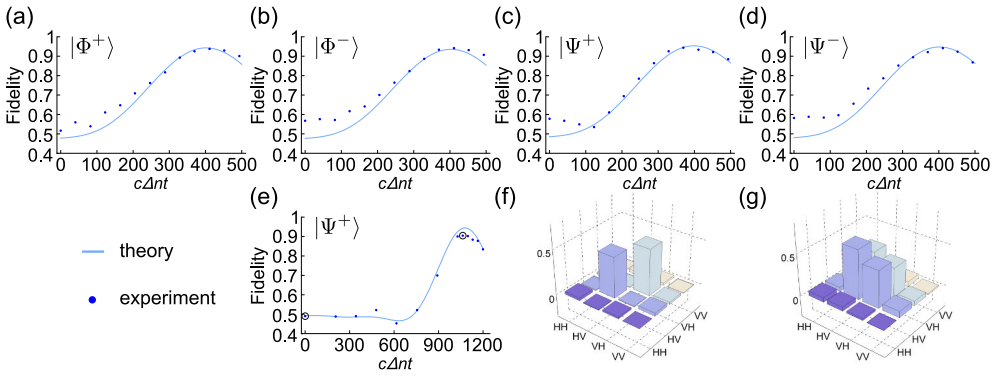

Figure 4.7. The experimental results of reverse decoherence. (a)–(e) Fidelities of the states under reverse decoherence as functions of the effective path difference in units of λ_0, with the target Bell states shown in upper left corners. The birefringent medium is quartz in (a)–(d) and a PM fiber in (e). The solid curves are the theoretical predictions, and the dots correspond to measurement data. The error bars, calculated by a Monte Carlo method, are of the same size as the dots. (f), (g) Real values of (f) the initial and (g) purified density matrix elements, corresponding to the circled data points in (e).

The auxiliary Bell state can be fully purified with noise appearing on Bob's side *before* the BSM. We modify the teleportation setup by blocking the pump laser before the BBO, inserting QWP1 on Alice's path, and setting HWP3 and HWP4 to $0°$.

4.3.3 Experimental results

Reverse decoherence

First, we considered the more trivial version of the protocol, i.e., having Bob's dephasing *before* the BSM. Here, we purified all the Bell states with dephasing—thus verifying reverse decoherence—but did not proceed with the rest of the teleportation protocol. These results are shown in Fig. 4.7, where we have plotted the *fidelities* $\mathcal{F}(t) = \langle\psi|\rho_{AB}(t)|\psi\rangle$ with $|\psi\rangle$ denoting the target Bell state. While trace distance quantifies the difference of states, fidelity quantifies their similarity, and it is given by [128]

$$\mathcal{F}(\rho_1, \rho_2) = \left(\mathrm{tr}\sqrt{\sqrt{\rho_1}\rho_2\sqrt{\rho_1}}\right)^2 \tag{4.40}$$

for two arbitrary states. With one them being pure, fidelity reduces to $\mathcal{F}(|\psi\rangle\langle\psi|, \rho) = \langle\psi|\rho|\psi\rangle$.

In Figs. 4.7(a)–(d), we used the phase function $\theta_B(f_B) = -2\pi f_B/c \cdot 429\lambda_0$ to reverse decoherence produced by quartz on Bob's side only. In all cases, maximum purity was achieved at approximately $400\lambda_0$. The mismatch with the factor of 429 in $\theta_B(f_B)$ is due to dispersion in quartz that accelerates dephasing. Moreover, the initial disagreements between theory and experiment may be due to a couple of factors.

First, a wider IF on Bob's side (3 nm) may have let decohered photons without the SLM-correction through. Secondly, the quartz plates may not have been perfectly aligned. Still, the experimental results match quite well with the theory. The theoretical predictions were evaluated numerically by using the SLM-pixel values, fitted frequency spectra, and Sellmeier equation of quartz instead of constant birefringence.

The theory and experimental data overlap quite nicely in Fig. 4.7(e), too. Here, we purified the Bell state $|\Psi^+\rangle$ in a 2 m PM fiber, gradually changing the slope of the phase function. Because there were no quartz plates to be aligned, the theory and experiment match even better than in Figs. 4.7(a)–(d). Maximum purity was achieved with $\theta_B(f_B) = -2\pi f_B/c \cdot 1063\lambda_0$. The amount of dephasing, $1080\lambda_0$, was used as a fit parameter. Because the Sellmeier equation of the fiber was not known, dispersion was not taken into account. This explains the small difference between the maxima of theory and experiment. Note that, while the phase function's slope is greater than the amount of dephasing in Figs. 4.7(a)–(d) ($429 > 400$), here it is the opposite ($1063 < 1080$), suggesting the opposite effect of dispersion. However, this is *not* the case. Actually, this is explained by the opposite quantities being fixed in Figs. 4.7(a)–(d) and Fig. 4.7(e), i.e., the phase functions and amount of dephasing, respectively. Dispersion still accelerates dephasing in Fig. 4.7(e).

To further visualize reverse decoherence, we have plotted the real values of the initial and time-evolved density matrix elements in Figs. 4.7(f) and (g), respectively. The imaginary components were practically zero.

Teleportation

With Bob's dephasing appearing *after* the BSM, we teleported the states $|+\rangle$, $|-\rangle$, $|R\rangle$, and $|L\rangle$ with different noise configurations: dephasing on Alice's side only ($400\lambda_0$ of YVO_4), dephasing on Bob's side only ($411\lambda_0$ of quartz), combination of these two, and either using or not using corresponding phase functions. Whenever SLMs were used, the phase functions were set to $\theta_A(f_A) = -2\pi f_A/c \cdot 446\lambda_0$ and $\theta_B(f_B) = -2\pi f_B/c \cdot 429\lambda_0$.

The fidelities of the final states ρ_f with respect to the input states ρ_i, given by Eq. (4.40), are presented in Fig. 4.8. The red and blue bars correspond to Alice and Bob's noise configurations, respectively, while the purple bars indicate that both configurations have been used in the same setup. The green bars represent the versions of each preceding bar on their left, where SLMs and phase functions were used to reverse decoherence. Clearly, we achieve high fidelities, in all cases well above the classical average fidelity limit, 2/3 [129] (black, dotted line), and approximately equal to the reference fidelities given by the orange lines. The reference fidelities were obtained with the basic, noiseless protocol.

These results, though of proof-of-concept nature, dispel two common requirements for quantum teleportation to work: (1) noise being absent, and (2) the re-

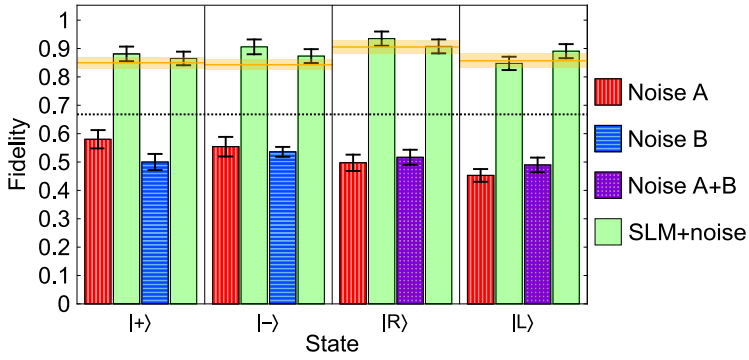

Figure 4.8. Fidelities of the teleported states. Red, vertical lines: dephasing on Alice's side only. Blue, horizontal lines: dephasing on Bob's side only. Purple grid: dephasing on both sides. Green: the same noise configuration as with the preceding bar on the left but with the SLMs and phase functions reversing decoherence. Different panels correspond to different states being teleported—given at the bottom of the picture—and the orange lines on top of each panel give the reference fidelities with no SLMs nor dephasing. The black dotted line is the classical average fidelity limit, 2/3. The error bars, calculated by a Monte Carlo method, are mainly due to the counting statistics.

source qubits being entangled. Strictly speaking, Alice and Bob do share a fully entangled polarization state in our setup. This is right before the polarization entanglement is converted to hybrid entanglement with SLMs. However, the initial polarization entanglement in our case is just a result of SPDC and not generally required for our protocol to work. For example, in Chapter 5, we will see that the same auxiliary state could also be prepared by guiding orthogonally polarized photons from independent sources into a beam splitter with distinct delay—corresponding to $\theta_j(f_j)$—and post-selecting the coincident photons. Here, the (coincident) polarization qubits shared by Alice and Bob would *never* be entangled. However, this method is more uncontrollable due to the increased randomness with two single-photon sources, which is why we chose to use SPDC and SLMs. Furthermore, one can control both $\theta_A(f_A)$ and $\theta_B(f_B)$ more precisely with SLMs, and they leave only dephasing time-parameterized, which corresponds better to the open-system picture.

5 Open system interference

The environment of the polarization degree of freedom can be expanded by taking other degrees of freedom into consideration besides frequency. In this Chapter, we take the photons' *path* and the discrete-time dynamics occurring at beam splitters into account—introducing the concept of *open system interference*. Open system interferometers serve three purposes: First, they highlight the fact that, in order for interference to occur at beam splitters, it is not enough for the photons' several degrees of freedom to be indistinguishable; Their correlations need to be identical as well. Secondly, open system interferometers provide a new way of reservoir engineering, resulting in rich features of open-system dynamics. And finally, open system interferometers give rise to alternative applications *based on* dephasing, not hindered by it.

5.1 Open system Mach-Zehnder interference

In Chapter 2, we saw that $HH|\psi\rangle = |\psi\rangle$, i.e., a photon entering a MZ interferometer consisting of two beam splitters ends up on its initial path with certainty. In other words, we have perfect interference. However, it was implicitly assumed that the two paths between the beam splitters are identical. In this Section, we consider a more general case, where the paths can be of different lengths and the polarization (arbitrary, but initially pure) can interact with frequency for different durations.

5.1.1 The model

The state of a single photon entering the first beam splitter of a MZ interferometer is

$$|\psi\rangle = (C_H|H\rangle + C_V|V\rangle) \int df g(f)|f\rangle|0\rangle, \tag{5.1}$$

where $|0\rangle$ denotes the photon's path (see Fig. 5.1). We write the corresponding path state after the first beam splitter as $|0'\rangle$, after the second beam splitter as $|0''\rangle$, and similarly for the other path. Going through the first beam splitter, we get $|0\rangle \mapsto (|0'\rangle + |1'\rangle)/\sqrt{2}$. Then, having free evolution and polarization dephasing for the respective durations $t_{j'f}$ and $t_{j'}$ on paths $j' = 0', 1'$, the state's evolution is described

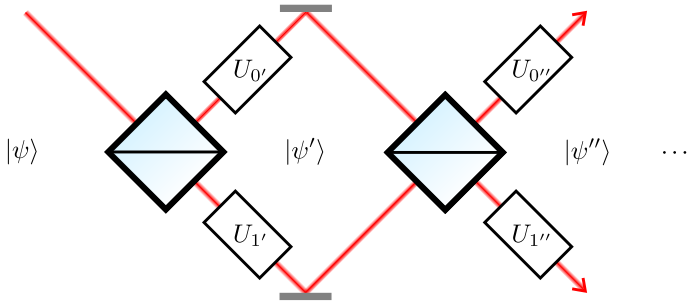

Figure 5.1. A schematic picture of the open system MZ interferometer.

by the unitary

$$U_{0'} \otimes |0'\rangle\langle 0'| + U_{1'} \otimes |1'\rangle\langle 1'|, \tag{5.2}$$

where $U_{j'}|\lambda\rangle|f\rangle = e^{i[2\pi f(t_{j'f}+n_\lambda t_{j'})]}|\lambda\rangle|f\rangle$, $\lambda = H, V$. For now, for the sake of simpler notation, we only consider the total durations of free evolution and dephasing and not the freely running laboratory time. At this stage, the total state of the photon is

$$\begin{aligned}|\psi'\rangle = \frac{1}{\sqrt{2}}\Big[&U_{0'}(C_H|H\rangle + C_V|V\rangle)\int df g(f)|f\rangle|0'\rangle \\ &U_{1'}(C_H|H\rangle + C_V|V\rangle)\int df g(f)|f\rangle|1'\rangle\Big].\end{aligned} \tag{5.3}$$

Again, partial tracing over environment (frequency and path) gives us the state of the open system (polarization),

$$\rho' = \begin{pmatrix} |C_H|^2 & C_H C_V^*(\kappa_{0'} + \kappa_{1'})/2 \\ C_H^* C_V(\kappa_{0'}^* + \kappa_{1'}^*)/2 & |C_V|^2 \end{pmatrix}. \tag{5.4}$$

This is just a balanced mixture of the two *pathwise states*

$$\rho_{j'} = \begin{pmatrix} |C_H|^2 & C_H C_V^* \kappa_{j'} \\ C_H^* C_V \kappa_{j'}^* & |C_V|^2 \end{pmatrix}, \tag{5.5}$$

where $\kappa_{j'} = \int df |g(f)|^2 e^{i2\pi f \Delta n t_{j'}}$. That is, if we measure the photon's path after the first beam splitter and get the result j', the polarization is in the state $\rho_{j'}$, but if we ignore the path, the state is $\rho' = (\rho_{0'} + \rho_{1'})/2$. Here, the projection operator corresponding to measuring path j' is $\mathbb{1} \otimes \mathbb{1} \otimes |j'\rangle\langle j'|$, and the probability of both paths is 1/2. In an actual experiment, measuring the photon's path and the pathwise polarization state could simply mean performing state tomography on the desired path and omitting photons on the other path.

Depending on the frequency distribution, the pathwise states can undergo Markovian dephasing while the total state experiences non-Markovian memory effects. If

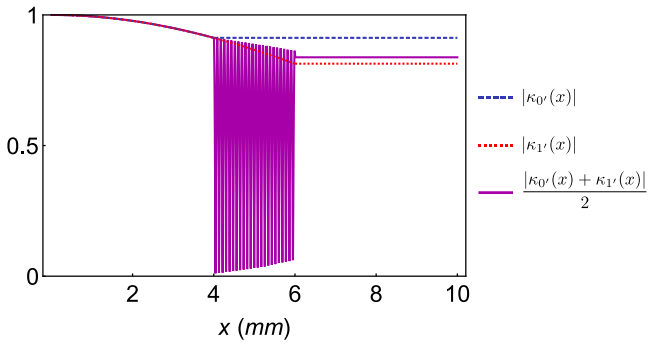

Figure 5.2. Magnitudes of the decoherence functions inside the interferometer as functions of position. $\mu = c/(780\text{ nm})$, $\sigma = 5.68 \times 10^{11}$ Hz, $n_H = 1.553$, $n_V = 1.544$, $x_{0'} = ct_{0'} = 4$ mm, and $x_{1'} = ct_{1'} = 6$ mm.

the spectrum is Gaussian and there are time intervals with nonoverlapping interaction (e.g., the photon travels across free air on path $0'$ but through quartz on path $1'$), ρ' undergoes oscillating dephasing dynamics (and therefore oscillating trace-distance dynamics of, e.g., the initial state pair $|\pm\rangle$) with the spectrum's mean frequency μ; On one of the paths, the polarization state is constant. On the other, the state keeps spiraling towards the Bloch ball's z-axis, periodically moving away and approaching its constant counterpart. Hence, the average dynamics oscillates. In Fig. 5.2, we have plotted such example dynamics. Note that the dynamics greatly resembles that caused by a double-peaked Gaussian (see Fig. 3.3). With the double-peaked Gaussian, the peaks' difference $\mu_1 - \mu_2$ gives the oscillation frequency, which means that it is easier to obtain much greater frequencies with the current setup.

Letting the photon take both paths between the beam splitters and having similar unitary dynamics as inside the interferometer, we get the total state

$$\begin{aligned}|\psi''\rangle = \frac{1}{2}\Big[&U_{0''}(U_{0'} + U_{1'})(C_H|H\rangle + C_V|V\rangle)\int df\, g(f)|f\rangle|0''\rangle \\ &U_{1''}(U_{0'} - U_{1'})(C_H|H\rangle + C_V|V\rangle)\int df\, g(f)|f\rangle|1''\rangle\Big].\end{aligned} \tag{5.6}$$

One could continue chaining beam splitters like this—creating an exotic *collision model* that mixes continuous-time and discrete-time dynamics—but this is where we stop. We are now in the position to answer the two main questions of this Section: *How does dephasing affect interference, i.e., the final path probabilities? How does interference, in turn, affect the following dephasing?*

The probability $P_{j''}$ to detect photon on path j'' is obtained as the trace of

$|\psi''\rangle\langle\psi''|$ projected on path $|j''\rangle$,

$$P_{j''} = \mathrm{tr}\big[\mathbb{1}\otimes\mathbb{1}\otimes|j''\rangle\langle j''|\psi''\rangle\langle\psi''|\mathbb{1}\otimes\mathbb{1}\otimes|j''\rangle\langle j''|\big] \tag{5.7}$$

$$= \langle\psi''|\mathbb{1}\otimes\mathbb{1}\otimes|j''\rangle\langle j''|\psi''\rangle \tag{5.8}$$

$$= \frac{2+(-1)^{j''}|C_H|^2\kappa_H + (-1)^{j''}|C_V|^2\kappa_V}{4}. \tag{5.9}$$

Here, assuming Gaussianity,

$$\kappa_\lambda = 2e^{-\frac{1}{2}(2\pi\sigma)^2(\Delta t'_f + n_\lambda\Delta t')^2}\cos[2\pi\mu(\Delta t'_f + n_\lambda\Delta t')], \tag{5.10}$$

where $\lambda = H, V$ and $\Delta t'_{(f)} := t_{0'(f)} - t_{1'(f)}$. Since unitaries preserve trace, the ongoing dynamics on paths j'' has no effect here.

From Eqs. (5.9) and (5.10) we see that the path probability depends on the temporal overlap of all the polarization components at the second beam splitter, the difference in interaction times having almost the same role as the delay $\Delta t'_f$. With equal interaction times $t_{0'} = t_{1'}$, the path probability would reduce to

$$P_{j''}(\Delta t'_f) = \frac{1}{2}\Big[1 + (-1)^{j''}e^{-\frac{1}{2}(2\pi\sigma\Delta t'_f)^2}\cos(2\pi\mu\Delta t'_f)\Big]. \tag{5.11}$$

However, as horizontal and vertical polarization components act differently under dephasing, we can control $P_{j''}$ in a much more versatile manner by adjusting $\Delta t'$, too. As before, the interaction times can be controlled by changing the thickness of birefringent crystals between the beam splitters, whereas the duration of free evolution can be controlled with mirrors.

Let us proceed with the open-system dynamics following the MZ interferometer. The total dynamics obtained by not measuring the photon's final path is similar to what we already described and therefore not particularly interesting—if the interaction times do not overlap, we may observe oscillating coherences. On the contrary, the pathwise dynamics turn out to be quite fascinating. Because the interactions on paths $0''$ and $1''$ do not affect each other, we can simplify the analysis by writing $U_{0''} = U_{1''} = U''(t)$, where we have the familiar action $U''(t)|\lambda\rangle|f\rangle = e^{i2\pi f n_\lambda t}|\lambda\rangle|f\rangle$. Here, we have omitted free evolution. It would not affect the open-system dynamics anymore. $t = 0$ is the point of time that the photon exits the second beam splitter and enters another birefringent crystal. The earlier time intervals may be interpreted as a way of introducing initial correlations, $t_{j'f}$ being responsible for interenvironmental (frequency-path) correlations and $t_{j'}$ for system-environment correlations.

Operating with $\mathbb{1}\otimes\mathbb{1}\otimes|j''\rangle\langle j''|$ on Eq. (5.6), taking partial trace, and normalizing, we get the open-system state on path $j'' = 0'', 1''$,

$$\rho_{j''}(t) = \frac{1}{4P_{j''}}\begin{pmatrix} |C_H|^2\big[2+(-1)^{j''}\kappa_H\big] & C_HC_V^*\kappa_{j''}(t) \\ C_H^*C_V\kappa_{j''}(t)^* & |C_V|^2\big[2+(-1)^{j''}\kappa_V\big]\end{pmatrix}. \tag{5.12}$$

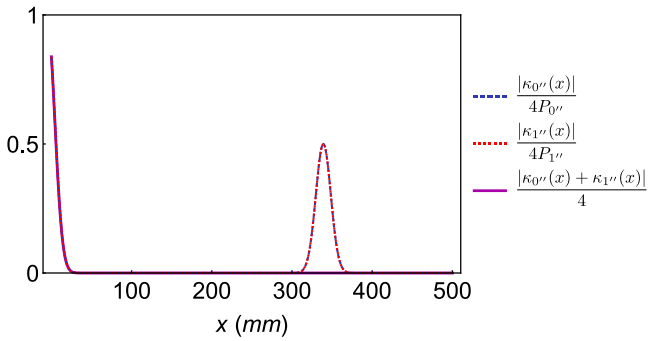

Figure 5.3. Magnitudes of the decoherence functions outside the interferometer as functions of position. Here, dephasing is implemented on the entire x-axis. $\mu = c/(780\text{ nm})$, $\sigma = 5.68 \times 10^{11}$ Hz, $n_H = 1.553$, $n_V = 1.544$, $x_{0'} = 4$ mm, $x_{1'} = 6$ mm, and $\Delta t'_f = 0$.

Here,

$$\begin{aligned}\kappa_{j''}(t) =& \kappa\big(\Delta n(t+t_{0'})\big) + \kappa\big(\Delta n(t+t_{1'})\big) \\ &+ (-1)^{j''}\kappa(\Delta n t + n_H t_{0'} - n_V t_{1'} + \Delta t'_f) \\ &+ (-1)^{j''}\kappa(\Delta n t - n_V t_{0'} + n_H t_{1'} - \Delta t'_f),\end{aligned} \tag{5.13}$$

where $\kappa(\tau)$ is the familiar single-photon decoherence function, $\kappa(\tau) = \exp[i2\pi\mu\tau - \frac{1}{2}(2\pi\sigma\tau)^2]$. The new decoherence function $\kappa_{j''}(t)/(4P_{j''})$ is a combination of the basic decoherence functions with different shifts, describing how the different polarization pairs $H+V$ combine in the second beam splitter and evolve afterwards. In the first (second) term, we have H and V from path $0'$ ($1'$). In the third (fourth) term, we have H (V) from path $0'$ and V (H) from path $1'$. From Eq. (5.13) we also see that, depending on the parameters, there should be some kind of a recoherence peak around either $\Delta n t = -n_H t_{0'} + n_V t_{1'} - \Delta t'_f$ or $\Delta n t = n_V t_{0'} - n_H t_{1'} + \Delta t'_f$, or not at all. The possible recoherence peak is due to the slower component of the shorter path j' momentarily recombining with the faster component of the longer path $j' \oplus 1'$. However, we might not have recoherence at all due to destructive interference.

In Fig. 5.3, we have plotted example dynamics outside of the open system MZ interferometer using the same parameters as in Fig. 5.2. For simplicity, we have set $\Delta t'_f = 0$. We will deal with the nonzero case soon. Comparing the two figures with each other, it is interesting to note a few things. First, it only takes the difference of 2 mm of quartz to push the pathwise recoherence peaks as far away as ~ 340 mm, and the peaks are very wide when compared to the preceding oscillations in Fig. 5.2. The increased time scale is due to the birefringence being close to zero; It takes long for the orthogonal polarization components to meet again. The peaks reach the value of 1/2 because the other two polarization components only move further away from each other, never intersecting. However, by locating this maximum value, we can estimate either $-n_H t_{0'} + n_V t_{1'} - \Delta t'_f$ or $n_V t_{0'} - n_H t_{1'} + \Delta t'_f$ *even when the path*

probabilities no longer carry information about them; In Fig. 5.3, we have $P_{0''} \approx P_{1''} \approx 1/2$, and small changes in the parameters do not change these probabilities.

By normalizing the decoherence function, $\tilde{\kappa}_{j''}(t) = \kappa_{j''}(t)/\kappa_{j''}(0)$, we can associate the recoherence peak in Fig. 5.3 with non-Markovianity. Thus, with the chosen parameters, the open system MZ interferometer displays completely opposite non-Markovian features inside and outside of itself; Inside, we have fast oscillations of trace distance, which are killed by the which-path-information. Outside, it is the which-path-information that gives rise to non-Markovianity, but this time giving only one, wide recoherence peak.

5.1.2 Interferometric region and CPTNI description

The interaction time difference in Fig. 5.3 is so large that we have no interference, at least in the traditional sense: The path probabilities are equal. Moreover, the polarization probabilities are just the initial values, $P_{\lambda_{0''}} \approx P_{\lambda_{1''}} \approx |C_\lambda|^2$. But when we start bringing the interaction times closer to each other and enter the "interferometric region", a couple of interesting things take place. First, as the path probabilities start oscillating, so do the polarization probabilities, allowing us to mimic dissipativelike dynamics. Note that this is solely due to $\Delta t'$. With $\Delta t' = 0$, the polarization probabilities would stay constant, regardless of the value of $\Delta t'_f$. Secondly, the pathwise recoherence peaks not only move to left, towards $t = 0$. They become very sensitive to the translation terms in Eq. (5.13), starting to vanish and reappear in an abrupt fashion. We will return to the question of sensitivity shortly.

In Fig. 5.4, we have plotted example dynamics in the interferometric region, using the initial values $|C_H|^2 = |C_V|^2 = 1/2$. With any set of parameters, even though the polarization probabilities may change from their initial values, the initial states maximizing the revivals of trace distance still lie on the antipodal points of the Bloch ball's equator. Hence, the pathwise trace distance of such a state pair is still given by the absolute value of the corresponding decoherence function. For example, with the usual normalization $\tilde{\kappa}_{j''}(t) = \kappa_{j''}(t)/\kappa_{j''}(0)$, the dephasing dynamics in Fig. 5.4(a) is Markovian on path $0''$ and non-Markovian on path $1''$. In Figs. 5.4(b), (d), (e), and (f), all the dynamics is Markovian. In Fig. 5.4(f), we have perfect interference, which is why we have nothing on path $1''$.

In Fig. 5.4(c), we cannot associate a CPTP map with the dynamics on path $0''$. However, such dynamics can still be described by a CPTNI quantum operation $\mathcal{E}^t_{j''}$ having the Kraus-type representation $\mathcal{E}^t_{j''}(\rho) = K_{+,j''}(t)\rho K_{+,j''}(t)^\dagger +$

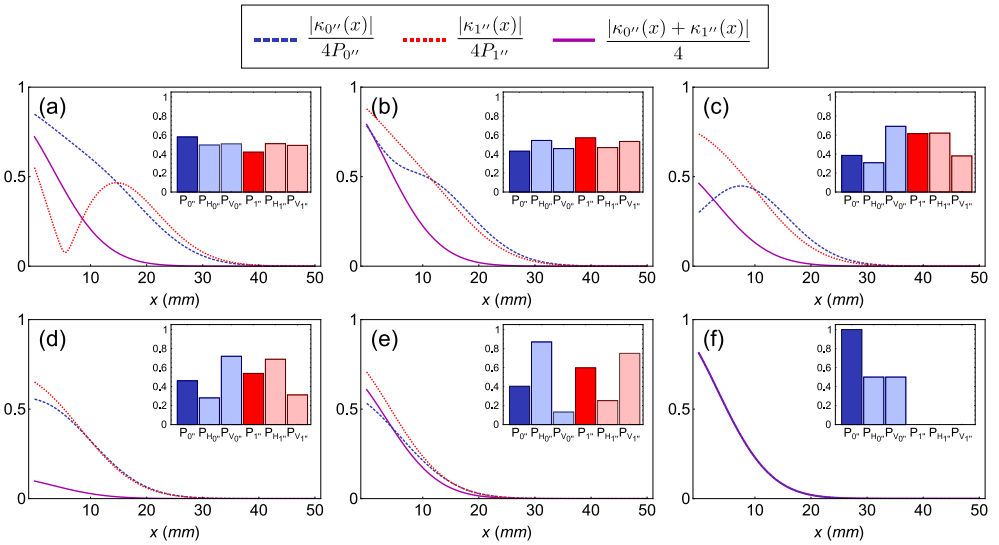

Figure 5.4. Magnitudes of the decoherence functions outside the interferometer as functions of position. Again, we have dephasing on the entire x-axis. Path and polarization probabilities are shown in the insets. Initially, before the second beam splitter, $|C_H|^2 = |C_V|^2 = 1/2$. (a) $x_{0'} = 5.90$ mm, (b) $x_{0'} = 5.92$ mm, (c) $x_{0'} = 5.94$ mm, (d) $x_{0'} = 5.96$ mm, (e) $x_{0'} = 5.98$ mm, and (f) $x_{0'} = 6.00$ mm. All the other parameters are the same as in Figs. 5.2 and 5.3.

$K_{-,j''}(t)\rho K_{-,j''}(t)^\dagger$, where

$$K_{\pm,j''}(t) = \sqrt{\frac{\sqrt{[2+(-1)^{j''}\kappa_H][2+(-1)^{j''}\kappa_V]} \pm |\kappa_{j''}(t)|}{2\sqrt{[2+(-1)^{j''}\kappa_H][2+(-1)^{j''}\kappa_V]}}} \times \begin{pmatrix} \pm\sqrt{2+(-1)^{j''}\kappa_H}\,\frac{\kappa_{j''}(t)}{|\kappa_{j''}(t)|} & 0 \\ 0 & \sqrt{2+(-1)^{j''}\kappa_V} \end{pmatrix} \tag{5.14}$$

and $\rho = (C_H|H\rangle + C_V|V\rangle)(C_H^*\langle H| + C_V^*\langle V|)$. Note that, in general, $\mathcal{E}^t_{j''}(\rho)$ is not normalized, i.e., we have $K_{+,j''}(t)^\dagger K_{+,j''}(t) + K_{-,j''}(t)^\dagger K_{-,j''}(t) \leq \mathbb{1}$. However, this inequality is saturated by perfect interference ($\kappa_H = \kappa_V = 2$), making $\mathcal{E}^t_{j''}$ a valid CPTP map with $j'' = 0''$. With $j'' = 1''$, we have nothing. Here, it is important to distinguish between the *input* state ρ and the *initial* state $\mathcal{E}^0_{j''}(\rho)$. Given a pure input state, the lossy CPTNI quantum operation $\mathcal{E}^0_{j''}$ either gives the initial state as an output or nothing at all. In the first case, before the continuous time evolution begins, $\mathcal{E}^0_{j''}$ immediately creates initial system-environment correlations and alters the open-system populations.

The two definitions of quantum non-Markovianity introduced in Chapter 3 were both based on the existence of a CPTP map. So, what can be said about non-Markovianity in the case of CPTNI operations? CPTNI operations do not (necessarily) preserve the trace, and here we not only have initial correlations, but $\mathcal{D}_{\text{tr}}\big(\rho_1(t),$

$\rho_2(t)\big) > \mathcal{D}_{\text{tr}}\big(\rho_1(0), \rho_2(0)\big)$ at some time interval. A linear mapping with this property could map states outside the Bloch ball. However, it turns out that the "TNI" in "CPTNI" saves us from such nonphysical scenarios; The decoherence function's absolute value remains below one because, with CPTNI dynamics, we do not normalize the evolving state. Furthermore, with our system of interest, the intermediate propagator $\mathcal{E}_{j''}^{t_2 \leftarrow t_1}$ can be written in terms of the Kraus operators

$$K_{\pm,j''}(t_1, t_2) = \sqrt{\frac{1 \pm \frac{|\kappa_{j''}(t_2)|}{|\kappa_{j''}(t_1)|}}{2}} \begin{pmatrix} \pm\frac{\kappa_{j''}(t_2)}{\kappa_{j''}(t_1)} \frac{|\kappa_{j''}(t_1)|}{|\kappa_{j''}(t_2)|} & 0 \\ 0 & 1 \end{pmatrix}, \tag{5.15}$$

which are essentially the same operators as in Eq. (3.54). The trace-decreasing part of the dynamics occurs strictly at the beam splitter. Hence, it is not considered in the propagator; Crudely speaking, we omit the time interval "$0_{\text{input}} \to 0_{\text{initial}}$". Concluding, if we are willing to accept losses, we can use the earlier definitions and call the dephasing dynamics in Fig. 5.4(c) path $0''$ non-Markovian—at least in the generalized CPTNI sense.

5.1.3 Sensitivity of memory effects

Here, we study the sensitivity of pathwise recoherence in more detail. We set $t_{0'} = t_{1'} = 0$, so $\frac{|\kappa_{j''}(t)|}{4P_{j''}} \leq \frac{|\kappa_{j''}(0)|}{4P_{j''}} = 1$, and we have the proper dephasing channel

$$\Phi_{j''}^t\big(\rho(0)\big) = \begin{pmatrix} |C_H|^2 & C_H C_V^* \frac{\kappa_{j''}(t)}{4P_{j''}} \\ C_H^* C_V \frac{\kappa_{j''}(t)^*}{4P_{j''}} & |C_V|^2 \end{pmatrix} \tag{5.16}$$

on both exit paths of the open system MZ interferometer. Therefore, we are actually studying the sensitivity of non-Markovian memory effects.

We have plotted $P_{0''}$ and the BLP-measures $\mathcal{N}(\Phi_{j''}^t)$ in Fig. 5.5, which gives some idea of how sensitive the memory effects are with respect to the path difference $\Delta x'_f = c\Delta t'_f$, and how the memory effects and path probabilities are related: The smaller the path difference, the narrower the "BLP peaks", and as the path difference grows, the peaks eventually approach the constant value of 1/2. Depending on the delay, both channels can be Markovian, non-Markovian, or one Markovian, the other non-Markovian. Interestingly, the non-Markovianities $\mathcal{N}(\Phi_{j''}^t)$ peak at the local minima of $P_{j''}$.

Before estimating the sensitivity of memory effects in more detail, let us define "sensitivity" in a more rigorous fashion. Say, we have an observable $O(\lambda)$ that depends on some parameter λ, and that we want to detect if λ changes by measuring $O(\lambda)$. In an ideal situation, if $\langle O(\lambda)\rangle$ changed, we would immediately know that there was a change in λ. With small deviations $|\delta\lambda| \ll 1$, the two changes have the

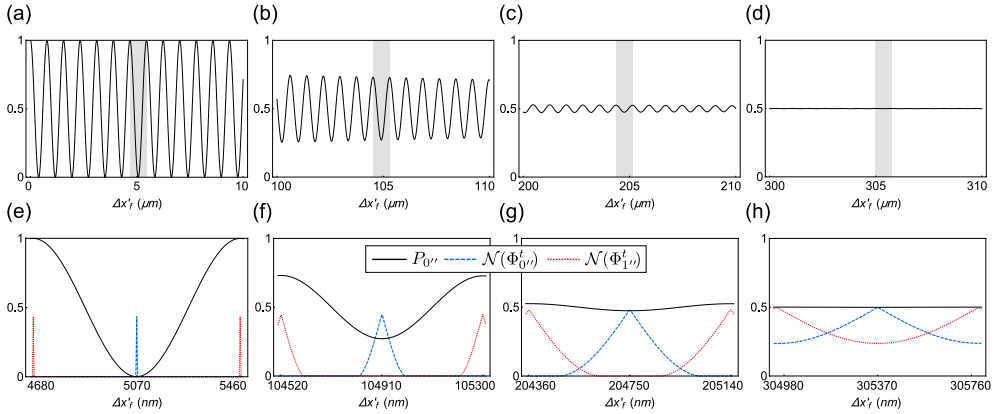

Figure 5.5. Path probabilities $P_{0''}$ (black, solid) and the pathwise BLP-non-Markovianities $\mathcal{N}(\Phi^t_{0''})$ (blue, dashed) and $\mathcal{N}(\Phi^t_{1''})$ (red, dotted) as functions of the path difference $\Delta x'_f$. The panels (e)–(h) are magnifications of the shaded regions in (a)–(d). $\mu = c/(780\text{ nm})$, $\sigma = 5.68 \times 10^{11}$ Hz, and $\Delta n = 0.009$.

approximate connection

$$\langle O(\lambda + \delta\lambda)\rangle \approx \langle O(\lambda)\rangle + \frac{\partial\langle O(\lambda)\rangle}{\partial\lambda}\delta\lambda \tag{5.17}$$

$$\Leftrightarrow |\langle O(\lambda + \delta\lambda)\rangle - \langle O(\lambda)\rangle| \approx \left|\frac{\partial\langle O(\lambda)\rangle}{\partial\lambda}\delta\lambda\right|. \tag{5.18}$$

However, since observables have intrinsic spread defined by the standard deviation $\Delta O := \sqrt{\langle O^2\rangle - \langle O\rangle^2}$, we cannot say if a small change in $\langle O(\lambda)\rangle$ was actually due to $\delta\lambda$ or not. Therefore, in order for $\delta\lambda$ to be experimentally detectable, the change $|\langle O(\lambda + \delta\lambda)\rangle - \langle O(\lambda)\rangle|$ needs to "stand out" from ΔO,

$$|\langle O(\lambda + \delta\lambda)\rangle - \langle O(\lambda)\rangle| \geq \Delta O \tag{5.19}$$

$$\Leftrightarrow |\delta\lambda| \geq \Delta O\left|\frac{\partial\langle O(\lambda)\rangle}{\partial\lambda}\right|^{-1}. \tag{5.20}$$

Finally, the value $\delta\lambda'$ that saturates the above inequality is called the observable's sensitivity [62].

With *parameter-independent measurements*—i.e., measurements with the parameter of interest not affecting the measurement procedure itself or its outcome space—the smallest achievable sensitivity is given by the *quantum Cramér-Rao bound (QCRB* [65]*)*,

$$|\delta\lambda'| \geq \frac{1}{\sqrt{MF_Q(\lambda)}}. \tag{5.21}$$

Here, M is the number of independent measurements and $F_Q(\lambda)$ is the *quantum Fisher information*. For pure states $|\psi\rangle$, the quantum Fisher information can be written as [66]

$$F_Q(\lambda) = 4(\langle\partial_\lambda\psi|\partial_\lambda\psi\rangle - |\langle\partial_\lambda\psi|\psi\rangle|^2), \tag{5.22}$$

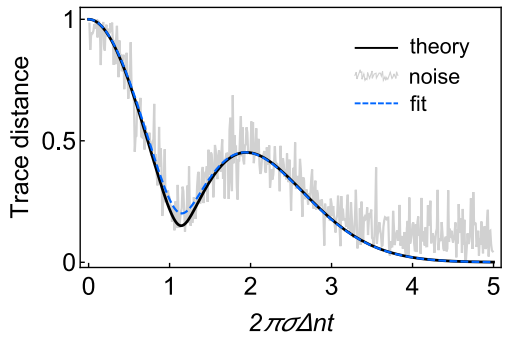

Figure 5.6. Illustration of the algorithm at $\Delta x'_f = 104888$ nm and FW $= 0.4$. While the theoretical, noiseless value is $\mathcal{N}(\Phi^t_{0''}) = 0.301498$, this run of the algorithm yields $\tilde{\mathcal{N}}_n(\Phi^t_{0''}) = 0.251261$. $\mu = c/(780\text{ nm})$, $\sigma = 5.68 \times 10^{11}$ Hz, and $\Delta n = 0.009$.

where $|\partial_\lambda \psi\rangle = \partial|\psi(\lambda)\rangle/\partial\lambda$.

We now use Eq. (5.20) to estimate the sensitivity of memory effects. Because the derivation of Eq. (5.20) did not depend on the measurable quantity being specifically an observable, we just replace O by $\mathcal{N}(\Phi^t_{j''})$ and λ by $\Delta x'_f$. The derivative $\partial\mathcal{N}(\Phi^t_{j''})/\partial\Delta x'_f$ can be evaluated numerically, but because $\mathcal{N}(\Phi^t_{j''})$ is not an observable, we cannot write "$\Delta\mathcal{N} = \sqrt{\langle\mathcal{N}^2\rangle - \langle\mathcal{N}\rangle^2}$". Instead, we define $\Delta\mathcal{N}(\Phi^t_{j''})$ as the standard deviation (SD) of $N \gg 1$ *perturbed* non-Markovianities $\tilde{\mathcal{N}}_n(\Phi^t_{j''})$, $\Delta\mathcal{N}(\Phi^t_{j''}) := \text{SD}\big(\{\tilde{\mathcal{N}}_n(\Phi^t_{j''})\}_{n=1}^N\big)$. The perturbed non-Markovianities are obtained from the following algorithm that illustrates how also non-Markovianity can vary between measurements. Here, however, the spread is not intrinsic, but results from outside factors such as dark counts and background photons.

At each value of $\Delta x'_f$, we simulate additional noise so that

$$\tilde{\rho}_{j''}(t) = \Phi^t_{j''}\big(\rho(0)\big) + \begin{pmatrix} \epsilon_1(t) & \epsilon_2(t)e^{i\epsilon_3(t)} \\ \epsilon_2(t)e^{-i\epsilon_3(t)} & -\epsilon_1(t) \end{pmatrix}. \tag{5.23}$$

We draw $\epsilon_1(t)$ and $\epsilon_2(t)$ from a normal distribution with the mean 0 and standard deviation $\tilde{\sigma}$, while the random phase $\epsilon_3(t)$ comes from a uniform distribution from 0 to 2π. At each time step from $2\pi\sigma\Delta n t_{\text{min}} = 0$ to $2\pi\sigma\Delta n t_{\text{max}} = 5$, we draw separate noise terms for the initial state pair $|\pm\rangle$, redrawing them if the resulting states are nonphysical. The width of one time step is $2\pi\sigma\Delta n\Delta t = 0.01$. Once the "randomized" trace-distance dynamics is fixed, we fit $|\kappa_{j''}(t)|/(4P_{j''})$ on it with a random seed value of $\Delta x'_f$—depicting our ignorance of its actual value—and evaluate $\tilde{\mathcal{N}}_n(\Phi^t_{j''})$. A single run of this algorithm is illustrated in Fig. 5.6 with $\Delta x'_f = 104888$ nm and full width of the additional noise FW $= 6\tilde{\sigma} = 0.4$.

Now, it is interesting to compare the sensitivity of memory effects with the QCRB. Note that, to use Eqs. (5.21) and (5.22), the state being measured should be pure and fixed. However, when measuring non-Markovianity, we need the state's

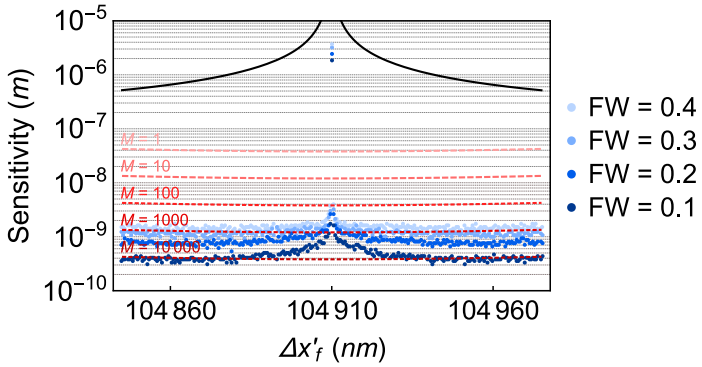

Figure 5.7. Sensitivities of $P_{0''}$ (black, solid) and $\mathcal{N}(\Phi^t_{0''})$ (blue dots), and the QCRBs (red, dashed). Different shades of blue correspond to different widths of additional noise, whereas different shades of red correspond to different numbers of measurements. $\mu = c/(780\text{ nm})$, $\sigma = 5.68 \times 10^{11}$ Hz, and $\Delta n = 0.009$.

entire time evolution, not just a single state. Hence, we are actually comparing our dynamical model against its more traditional, fixed-state counterpart. In the latter case, the QCRB can be calculated using the post-selected pure state

$$|\psi_{j''}(t)\rangle = \frac{1}{2\sqrt{P_{j''}}}\Bigg[C_H|H\rangle \int df g(f) e^{i2\pi f n_H t}\left(e^{i2\pi f t_{0'f}} + (-1)^{j''} e^{i2\pi f t_{1'f}}\right)|f\rangle|j''\rangle + C_V|V\rangle \int df g(f) e^{i2\pi f n_V t}\left(e^{i2\pi f t_{0'f}} + (-1)^{j''} e^{i2\pi f t_{1'f}}\right)|f\rangle|j''\rangle\Bigg]. \tag{5.24}$$

In Fig. 5.7, we have plotted the sensitivities of memory effects with four different FWs of additional noise (blue dots), the QCRBs with five different numbers of measurements (red, dashed curves), and, for comparison, the sensitivity of $P_{0''}$ (black, solid curve). At each value of $\Delta x'_f$, the algorithm was repeated $N = 100$ times to obtain $\Delta\mathcal{N}(\Phi^t_{0''})$. With $P_{0''}$, the observable used in Eq. (5.20) was $\mathbb{1} \otimes \mathbb{1} \otimes |0''\rangle\langle 0''|$. From Fig. 5.7, we can clearly see that the sensitivities are directly proportional to FW, while the QCRBs are inversely proportional to M. Therefore, with small enough values of FW and M, the memory effects can beat the QCRB.

But what counts as a single measurement in our case? If each and every coincidence event in polarization tomography adds up to M, our protocol requires a huge number of them, meaning low QCRB. However, while we need lots of measurements in this sense, our protocol is also very robust against additional noise[1], meaning low sensitivity. Our protocol therefore has genuine potential to break the QCRB in an actual experiment. And even with more noise, when Eq. (5.21) is satisfied, the memory effects still beat the path probabilities.

[1] FW $= 0.4$ in Fig. 5.6 is greatly exaggerated.

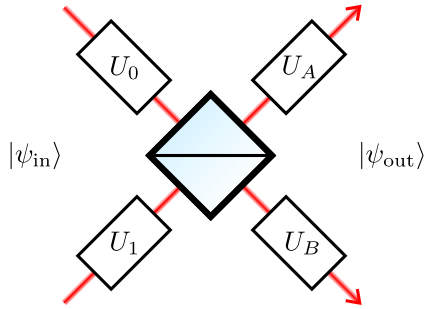

Figure 5.8. A schematic picture of the open system HOM interferometer.

We can go beyond the quantum Cramér-Rao theorem for two reasons. First, our protocol depends on the parameter of interest in the sense that, to fully capture the memory effects (or their absence), the process tomography should extend until $t \approx |\Delta t'_f/\Delta n|$, and the quantum Cramér-Rao theorem does not concern parameter-dependent measurements [130]. Secondly, instead of our system of interest being in a single fixed state, we monitor its entire evolution, and—to the best of our knowledge—the quantum Cramér-Rao theorem does not concern such situations either.

5.2 Open system Hong-Ou-Mandel interference

In this Section, we double the number of photons and half the number of beam splitters. That is, we study the interplay of *Hong-Ou-Mandel (HOM) interference* [63] and the dephasing of polarization.

5.2.1 The model

Our system of interest consists of two photons initially on their own paths, labeled by 0 and 1. The photons are guided into a beam splitter, from which they go to Alice (path A) or Bob (path B), i.e., they *bunch*, or both parties receive one photon (coincidence). Here, dephasing is considered both before and after the beam splitter, while free evolution is only considered on paths 0 and 1. Again, free evolution after the beam splitter would not affect the open-system dynamics. The model is illustrated in Fig. 5.8.

Because we now have the possibility of bunching, i.e., having two photons on the same path (A or B), we use the *creation* and *annihilation operators*. $\hat{a}^\dagger_\lambda(f)$ creates a photon with the polarization $\lambda = H, V$ and frequency f on the mode a, while $\hat{a}_\lambda(f)$ destroys such photon. The operators satisfy the commutation relation $[\hat{a}_\lambda(f), \hat{a}^\dagger_\lambda(f)] = \mathbb{1}$.

The initial biphoton state can be written in terms of the creation operators as

$$
\begin{aligned}
&|\psi_{\text{in}}\rangle = \\
&\Big[C_{HH}\int df_0 df_1 g(f_0,f_1)\hat{a}_H^\dagger(f_0)\hat{b}_H^\dagger(f_1) + C_{HV}\int df_0 df_1 g(f_0,f_1)\hat{a}_H^\dagger(f_0)\hat{b}_V^\dagger(f_1) \\
&+ C_{VH}\int df_0 df_1 g(f_0,f_1)\hat{a}_V^\dagger(f_0)\hat{b}_H^\dagger(f_1) + C_{VV}\int df_0 df_1 g(f_0,f_1)\hat{a}_V^\dagger(f_0)\hat{b}_V^\dagger(f_1)\Big] \\
&|0_{ab}\rangle.
\end{aligned}
\tag{5.25}
$$

Here, $\hat{a}_\lambda^\dagger(f_0)$ operates on path 0 and $\hat{b}_\lambda^\dagger(f_1)$ on path 1, and $|0_{ab}\rangle$ is the *vacuum state*. The operators transform in free evolution and polarization-frequency interaction according to

$$
\begin{cases}
U_0\hat{a}_{\lambda_0}^\dagger(f_0) = e^{i2\pi f_0(t_{0f}+n_{\lambda_0}t_0)}\hat{a}_{\lambda_0}^\dagger(f_0), \\
U_1\hat{b}_{\lambda_1}^\dagger(f_1) = e^{i2\pi f_1(t_{1f}+n_{\lambda_1}t_1)}\hat{b}_{\lambda_1}^\dagger(f_1).
\end{cases}
\tag{5.26}
$$

The action of the beam splitter reads

$$
\begin{cases}
H\hat{a}_{\lambda_0}^\dagger(f_0) = \frac{1}{\sqrt{2}}\big[\hat{a}_{\lambda_0}^\dagger(f_0) + \hat{b}_{\lambda_0}^\dagger(f_0)\big], \\
H\hat{b}_{\lambda_1}^\dagger(f_1) = \frac{1}{\sqrt{2}}\big[\hat{a}_{\lambda_1}^\dagger(f_1) - \hat{b}_{\lambda_1}^\dagger(f_1)\big].
\end{cases}
\tag{5.27}
$$

From now on, $\hat{a}_{\lambda_j}^\dagger(f_j)$ operates on path A and $\hat{b}_{\lambda_j}^\dagger(f_j)$ on path B. The final transformations following the beam splitter read

$$
\begin{cases}
U_A\hat{a}_{\lambda_j}^\dagger(f_j) = e^{i2\pi f_j n_{\lambda_j} t_A}\hat{a}_{\lambda_j}^\dagger(f_j), \\
U_B\hat{b}_{\lambda_j}^\dagger(f_j) = e^{i2\pi f_j n_{\lambda_j} t_B}\hat{b}_{\lambda_j}^\dagger(f_j).
\end{cases}
\tag{5.28}
$$

Substituting Eqs. (5.26)–(5.28) in Eq. (5.25), we get the output state

$$
\begin{aligned}
&|\psi_{\text{out}}\rangle = \sum_{\lambda_0,\lambda_1=H,V}\frac{C_{\lambda_0\lambda_1}}{2}\int df_0 df_1 g(f_0,f_1)e^{i[2\pi f_0(t_{0f}+n_{\lambda_0}t_0)+2\pi f_1(t_{1f}+n_{\lambda_1}t_1)]} \\
&\times\Big[e^{i(2\pi f_0 n_{\lambda_0}t_A+2\pi f_1 n_{\lambda_1}t_A)}\hat{a}_{\lambda_0}^\dagger(f_0)\hat{a}_{\lambda_1}^\dagger(f_1) - e^{i(2\pi f_0 n_{\lambda_0}t_A+2\pi f_1 n_{\lambda_1}t_B)}\hat{a}_{\lambda_0}^\dagger(f_0)\hat{b}_{\lambda_1}^\dagger(f_1) \\
&+ e^{i(2\pi f_0 n_{\lambda_0}t_B+2\pi f_1 n_{\lambda_1}t_A)}\hat{b}_{\lambda_0}^\dagger(f_0)\hat{a}_{\lambda_1}^\dagger(f_1) - e^{i(2\pi f_0 n_{\lambda_0}t_B+2\pi f_1 n_{\lambda_1}t_B)}\hat{b}_{\lambda_0}^\dagger(f_0)\hat{b}_{\lambda_1}^\dagger(f_1)\Big] \\
&|0_{ab}\rangle.
\end{aligned}
\tag{5.29}
$$

Note that we still have not considered whether the photons bunch or not, i.e., they are in the superposition of both options. The projection operator corresponding to Alice receiving only one photon is

$$
\hat{P}_A = \int df\hat{a}_H^\dagger(f)|0_a\rangle\langle 0_a|\hat{a}_H(f) + \int df\hat{a}_V^\dagger(f)|0_a\rangle\langle 0_a|\hat{a}_V(f),
\tag{5.30}
$$

while the projection of Alice receiving *both* photons is

$$\hat{P}_{AA} = \frac{1}{2} \sum_{\lambda_0,\lambda_1=H,V} \int df_0 df_1 \hat{a}^\dagger_{\lambda_0}(f_0)\hat{a}^\dagger_{\lambda_1}(f_1)|0_a\rangle\langle 0_a|\hat{a}_{\lambda_0}(f_0)\hat{a}_{\lambda_1}(f_1) \otimes |0_b\rangle\langle 0_b|, \tag{5.31}$$

and similarly for Bob.

We now have all the tools to calculate the coincidence probability P_c and see how dephasing before the beam splitter affects it. Using the bivariate Gaussian frequency distribution (4.13), we get

$$\begin{aligned} P_c &= \mathrm{tr}\big[\hat{P}_A \otimes \hat{P}_B|\psi_{\text{out}}\rangle\langle\psi_{\text{out}}|\hat{P}_A \otimes \hat{P}_B\big] && (5.32)\\ &= \langle\psi_{\text{out}}|\hat{P}_A \otimes \hat{P}_B|\psi_{\text{out}}\rangle && (5.33)\\ &= \frac{1}{2}\Big\{1 - |C_{HH}|^2 e^{-(1-K)(2\pi\sigma)^2(\Delta t_f + n_H\Delta t)^2} - |C_{VV}|^2 e^{-(1-K)(2\pi\sigma)^2(\Delta t_f + n_V\Delta t)^2} \\ &\quad - 2|C_{HV}||C_{VH}|e^{-\frac{1}{2}(2\pi\sigma)^2\left[(\Delta t_f + n_H\Delta t)^2 - 2K(\Delta t_f + n_H\Delta t)(\Delta t_f + n_V\Delta t) + (\Delta t_f + n_V\Delta t)^2\right]} \\ &\quad \times \cos(2\pi\mu\Delta n\Delta t + \theta_{HV} - \theta_{VH})\Big\}. && (5.34) \end{aligned}$$

Here, $\Delta t_f := t_{0f} - t_{1f}$, $\Delta t := t_0 - t_1$, and θ_{HV} (θ_{VH}) is the phase of C_{HV} (C_{VH}). The receiver-specific bunching probability is simply $P_b^{A(B)} = (1 - P_c)/2$.

The exponential functions weighted by the probabilities $|C_{\lambda\lambda}|^2$ just describe the temporal difference of the input paths' λ components. The cross-terms, on the other hand, oscillate with the frequency μ. Unlike with the open system MZ interferometer, the μ-dependency in Eq. (5.34) comes *solely from dephasing*. The Bell state $|\Psi^+\rangle$ is symmetric with respect to pairwise change of variables and therefore contributes to the bosonic behavior of photons, i.e., they tend to bunch ($P_c = 0$). Conversely, the Bell state $|\Psi^-\rangle$ is antisymmetric, which tends to drive the photons away from each other ($P_c = 1$). Now, the μ-dependency of P_c is explained by the rotation in dephasing, which causes the symmetry and antisymmetry to alternate.

Note that when the two photons entering the beam splitter differ only by free evolution, we get the classical "HOM dip" [63]

$$P_c(\Delta t_f) = \frac{1}{2}\Big[1 - e^{-(1-K)(2\pi\sigma\Delta t_f)^2}\Big]. \tag{5.35}$$

The narrowest dip is given by $K = -1$, i.e., frequency-anticorrelated photons, while the dip "fattens" as $K \to 1$. This is because HOM interference is differential-frequency-type interference [131]. That is, if the spectrum is decomposed as in Eq. (4.14), only the term with the argument $f_0 - f_1$ contributes to P_c. While this term is well-defined at $K = -1$, it approaches delta function when $K \to 1$, and the photons become temporally delocalized (see the earlier discussion in Chapter 4). Hence, the delay Δt_f does not matter, and the photons always bunch.

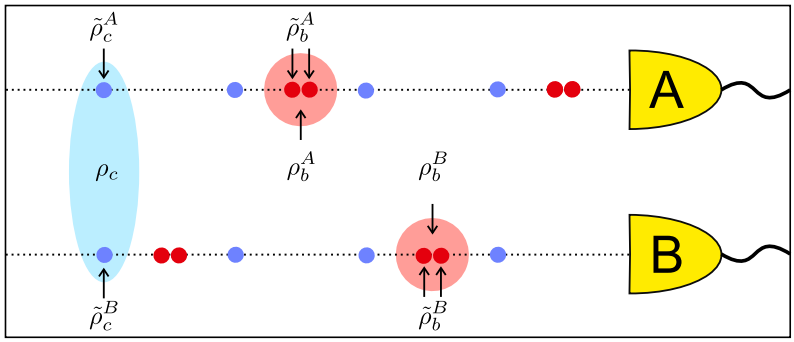

Figure 5.9. A schematic picture of the c- and b-photons and the different polarization states they carry. For illustrative purposes, the photons are depicted as point-like particles and as if they were not in the superposition state of coincidence and bunching.

We now turn our focus to the open-system dynamics following the beam splitter. With two photons either bunching or not, Alice and Bob can reconstruct different states with polarization tomography. They can post-select the coincident photons (*c-photons*) or bunched photons (*b-photons*), and choose whether to perform single-photon or biphoton polarization tomography. We denote the bipartite states of the c-photons by ρ_c and the corresponding single-qubit states by $\tilde{\rho}_c^{A(B)}$. Similarly, we denote the two-qubit states carried by the b-photons by $\rho_b^{A(B)}$ and the corresponding single-qubit states by $\tilde{\rho}_b^{A(B)}$. These states are visualized in Fig. 5.9 with the simplifying assumption that the photons already bunch (or not) at the beam splitter.

In the case of coincidence, Alice and Bob share the polarization-frequency state

$$\Pi_c = \frac{1}{P_c}\hat{P}_A \otimes \hat{P}_B |\psi_{\text{out}}\rangle\langle\psi_{\text{out}}| \hat{P}_A \otimes \hat{P}_B. \tag{5.36}$$

The density matrix elements $\langle\xi_0\xi_1|\rho_c|\lambda_0\lambda_1\rangle$ of the bipartite polarization state ρ_c are given by

$$\langle\xi_0\xi_1|\rho_c|\lambda_0\lambda_1\rangle = \int df_0 df_1 \langle 0_{ab}|\hat{a}_{\xi_0}(f_0)\hat{b}_{\xi_1}(f_1)\Pi_c \hat{a}^\dagger_{\lambda_0}(f_0)\hat{b}^\dagger_{\lambda_1}(f_1)|0_{ab}\rangle, \tag{5.37}$$

where $\xi_0, \xi_1, \lambda_0, \lambda_1 = H, V$. Alice's (Bob's) single-photon polarization state corresponding to coincidence is then obtained by the partial trace $\tilde{\rho}_c^{A(B)} = \text{tr}_{B(A)}[\rho_c]$.

In the case of bunching on Alice's side, the polarization-frequency state is

$$\Pi_b^A = \frac{1}{2P_b^A}\hat{P}_{AA}|\psi_{\text{out}}\rangle\langle\psi_{\text{out}}|\hat{P}_{AA}, \tag{5.38}$$

where the factor of $1/2$ is a normalization constant coming from the commutation relation of the creation and annihilation operators. The density matrix elements

$\langle\xi_0\xi_1|\rho_b^A|\lambda_0\lambda_1\rangle$ of the polarization state ρ_b^A are given by

$$\langle\xi_0\xi_1|\rho_b^A|\lambda_0\lambda_1\rangle = \int df_0 df_1 \langle 0_{ab}|\hat{a}_{\xi_0}(f_0)\hat{a}_{\xi_1}(f_1)\Pi_b^A \hat{a}^\dagger_{\lambda_0}(f_0)\hat{a}^\dagger_{\lambda_1}(f_1)|0_{ab}\rangle. \quad (5.39)$$

Note that Eq. (5.39) describes a biphoton polarization state completely on Alice's side, and reconstructing it with state tomography would require separating the b-photons. *Not* separating the b-photons—and performing single-photon polarization tomography instead—we get the identical states $\tilde{\rho}_b^A = \mathrm{tr}_0[\rho_b^A] = \mathrm{tr}_1[\rho_b^A]$. Bob's states are obtained in a similar fashion.

Interpreting the open-system dynamics to start from the beam splitter, t_0 and t_1 once again produce initial system-environment correlations. This time, however, the correlation coefficient K describes interenvironmental correlations, and the beam splitter mixes the preceding dynamics in a way that allows us to go beyond the conventional decoherence-function-description of open-system dynamics. For example, while the standard description gives us the nonlocal density matrix element

$$\langle HV|\rho(t)|VH\rangle = C_{HV}C^*_{VH}\Lambda_{AB}(t), \quad (5.40)$$

where $\Lambda_{AB}(t)$ is some decoherence function, here we have

$$\begin{aligned}
&\langle HV|\rho_c|VH\rangle = \\
&\frac{1}{4P_c}\Big\{ C_{HV}C^*_{VH} e^{i\eta(\tau_0-\tau_1+\tau_A-\tau_B)-\frac{1}{2}\left[(\tau_0+\tau_A)^2-2K(\tau_0+\tau_A)(\tau_1+\tau_B)+(\tau_1+\tau_B)^2\right]} \\
&\quad + C^*_{HV}C_{VH} e^{i\eta(-\tau_0+\tau_1+\tau_A-\tau_B)-\frac{1}{2}\left[(\tau_0+\tau_B)^2-2K(\tau_0+\tau_B)(\tau_1+\tau_A)+(\tau_1+\tau_A)^2\right]} \\
&\quad - |C_{HV}|^2 e^{i\eta(\tau_A-\tau_B)-\frac{1}{2}\left[(\Delta\tau_{HV}+\tau_A)^2-2K(\Delta\tau_{HV}+\tau_A)(\Delta\tau_{HV}+\tau_B)+(\Delta\tau_{HV}+\tau_B)^2\right]} \\
&\quad - |C_{VH}|^2 e^{i\eta(\tau_A-\tau_B)-\frac{1}{2}\left[(\Delta\tau_{VH}-\tau_A)^2-2K(\Delta\tau_{VH}-\tau_A)(\Delta\tau_{VH}-\tau_B)+(\Delta\tau_{VH}-\tau_B)^2\right]} \Big\}
\end{aligned} \quad (5.41)$$

and

$$\begin{aligned}
\langle HV|\rho_b^A|VH\rangle = \frac{1}{8P_b^A}\Big\{ &|C_{HV}|^2 e^{-(1-K)(\Delta\tau_{HV}+\tau_A)^2} + |C_{VH}|^2 e^{-(1-K)(\Delta\tau_{VH}-\tau_A)^2} \\
&+ 2|C_{HV}||C_{VH}| e^{-\frac{1}{2}\left[(\tau_0+\tau_A)^2-2K(\tau_0+\tau_A)(\tau_1+\tau_A)+(\tau_1+\tau_A)^2\right]} \\
&\times \cos\left[\eta(\tau_0-\tau_1)+\theta_{HV}-\theta_{VH}\right]\Big\}.
\end{aligned} \quad (5.42)$$

That is, we do not have a single decoherence function multiplying the coherence term $C_{HV}C^*_{VH}$ anymore. In Eqs. (5.41) and (5.42), we used the shorthand notations $\eta = \mu/\sigma$, $\tau_j = 2\pi\sigma\Delta n t_j$, and $\Delta\tau_{\lambda_0\lambda_1} = 2\pi\sigma(\Delta t_f + n_{\lambda_0}t_0 - n_{\lambda_1}t_1)$.

All the other density matrix elements can be found from Publication **V**. In the following Subsections, we concentrate on a few special cases that have interesting applications. For simplicity, we drop the dephasing before the beam splitter, i.e., $t_0 = t_1 = 0$.

5.2.2 Remote entanglement generation

In addition to SPDC, polarization-entangled photons can be produced with HOM interference [132]. Guiding horizontally and vertically polarized photons simultaneously into a beam splitter, Alice and Bob receive the Bell state $|\Psi^-\rangle$ with the probability $P_c = 1/2$. With the probability $P_b^{A(B)} = 1/4$, Alice (Bob) has the "local" Bell state $|\Psi^+\rangle$ all to themselves. However, it can be quite demanding to reach exactly $\Delta t_f = 0$. Hence, we let $|\Delta t_f| > 0$ and show how to compensate this delay with dephasing following the beam splitter.

With the initial polarization state $|HV\rangle$ experiencing coincidence (with the probability $P_c = 1/2$), we get the state

$$\rho_c(t_A, t_B) = \frac{1}{2}\begin{pmatrix} 0 & 0 & 0 & 0 \\ 0 & 1 & -\Lambda_c(t_A, t_B) & 0 \\ 0 & -\Lambda_c(t_A, t_B)^* & 1 & 0 \\ 0 & 0 & 0 & 0 \end{pmatrix}, \tag{5.43}$$

where $\Lambda_c(t_A, t_B) = \exp\left\{i2\pi\mu\Delta n(t_A - t_B) - \frac{1}{2}(2\pi\sigma)^2\left[(\Delta n t_A + \Delta t_f)^2 - 2K(\Delta n t_A + \Delta t_f)(\Delta n t_B + \Delta t_f) + (\Delta n t_A + \Delta t_f)^2\right]\right\}$. If we have bunching on Alice's side ($P_b^A = 1/4$), we get

$$\rho_b^A(t_A) = \frac{1}{2}\begin{pmatrix} 0 & 0 & 0 & 0 \\ 0 & 1 & \Lambda_b^A(t_A) & 0 \\ 0 & \Lambda_b^A(t_A)^* & 1 & 0 \\ 0 & 0 & 0 & 0 \end{pmatrix}, \tag{5.44}$$

and similarly for Bob. Here, $\Lambda_b^A(t_A) = \Lambda_c(t_A, t_A) = e^{-(1-K)(2\pi\sigma)^2(\Delta n t_A + \Delta t_f)^2}$.

If $\Delta t_f = 0$, there is clearly no need for delay-compensating dephasing. The same holds if $K = 1$. In other cases, Alice and Bob achieve maximum entanglement by implementing dephasing for the durations $t_A = t_B = -\Delta t_f/\Delta n$. At these points of time, the slower polarization component of the first photon overlaps with the faster component of the second photon. If $K = -1$, it suffices for only one of the parties to apply dephasing, e.g., $t_A = -2\Delta t_f/\Delta n$. Due to the birefringence Δn being (typically) close to zero, the temporal overlap of the photons is much easier to achieve here than in free air. For example, to compensate the path difference of $\Delta x_f = c\Delta t_f = 10$ µm, Alice and Bob need to use approximately 1 mm of quartz, and small deviations do not significantly hurt the concurrence of the final state.

Once the parties share the Bell state $|\Psi^-\rangle$, it can be changed to others with local Pauli operators. To prepare the same Bell state independently of coincidence and bunching (up to a global phase factor), either Alice or Bob needs to operate with σ_z after dephasing. In the case of coincidence, σ_z operates only once and transforms $|\Psi^-\rangle$ into $\pm|\Psi^+\rangle$ (+ with Alice, − with Bob). Bunching, on the other hand, means

operating with σ_z to either both of the photons (yielding $-|\Psi^+\rangle$) or neither (yielding $|\Psi^+\rangle$).

Note that the protocol would work similarly with dephasing *before* the beam splitter. However, our method dispels the common belief that the two photons should overlap at the beam splitter. Furthermore, applying dephasing after the beam splitter might be more convenient for distant parties. Note also that the delay plays exactly the same role as the phase functions $\theta_j(f_j)$ in reverse decoherence [see Eq. (4.34)]. Here, however, the two functions $\theta_A(f_A)$ and $\theta_B(f_B)$ cannot be controlled independently of each other, since $\theta_j(f_j) = -2\pi f_j \Delta t_f$ with both $j = A, B$.

Besides remote entanglement generation, our procol can be applied in parameter estimation when there is no more information about the parameter(s) of interest in the coincidence rate. Alice and Bob can, e.g., estimate Δt_f and K by monitoring the nonlocal dephasing dynamics. While $\Delta t_f = -\Delta n t_j$ (where t_j is the point of interaction time of maximum coherences), K can be estimated by analyzing the width of the recoherence peak. In the following Subsection, we will propose an alternative method for this task that, counterintuitively, does not require communication between Alice and Bob. That is, they need not compare their photon counts with each other.

5.2.3 Local parameter estimation by dead-time filtering

The single-photon polarization state that Alice can reconstruct alone is a mixture of P_c c-photon states and $2P_b^A$ b-photon states,

$$\tilde{\rho}^A(t_A) = P_c \tilde{\rho}_c^A(t_A) + 2P_b^A \tilde{\rho}_b^A(t_A). \tag{5.45}$$

The factor of two comes from the fact that for each bunching event there are two photons. Assuming initial polarization state of the form $(C_H|H\rangle + C_V|V\rangle) \otimes (C_H|H\rangle + C_V|V\rangle)$ and taking partial traces over the other polarization degree of freedom, we obtain

$$\tilde{\rho}_c^A(t_A) = \begin{pmatrix} |C_H|^2 & C_H C_V^* \kappa_-(t_A) \\ C_H^* C_V \kappa_-(t_A)^* & |C_V|^2 \end{pmatrix} \tag{5.46}$$

and

$$\tilde{\rho}_b^A(t_A) = \begin{pmatrix} |C_H|^2 & C_H C_V^* \kappa_+(t_A) \\ C_H^* C_V \kappa_+(t_A)^* & |C_V|^2 \end{pmatrix}, \tag{5.47}$$

where

$$\begin{aligned} \kappa_\pm(t_A) =& \frac{1 \pm e^{-(1-K)(2\pi\sigma\Delta t_f)^2} \cosh[(1-K)(2\pi\sigma)^2 \Delta t_f \Delta n t_A]}{1 \pm e^{-(1-K)(2\pi\sigma\Delta t_f)^2}} \\ & \times e^{i2\pi\mu\Delta n t_A - \frac{1}{2}(2\pi\sigma\Delta n t_A)^2}. \end{aligned} \tag{5.48}$$

From Eq. (5.48), we see that the H and V polarization components originating from different paths acquire different phase depending on whether the photons bunch or

not: An even multiple of π for b-photons and odd for c-photons. Conversely, H and V from the same path are in the same phase for c- and b-photons [cf. Eq. (5.13) and its description]. Both single-photon states $\tilde{\rho}_c^A(t_A)$ and $\tilde{\rho}_b^A(t_A)$ depend on K due to the nonlocal transformations in Eq. (5.27).

Substituting Eqs. (5.46) and (5.47) in Eq. (5.45), we get

$$\tilde{\rho}_A(t_A) = \begin{pmatrix} |C_H|^2 & C_H C_V^* \kappa(t_A) \\ C_H^* C_V \kappa(t_A)^* & |C_V|^2 \end{pmatrix}. \tag{5.49}$$

Here, quite interestingly, $\kappa(t_A)$ is just the familiar single-photon decoherence function, $\kappa(t_A) = e^{i2\pi\mu\Delta n t_A - (2\pi\sigma\Delta n t_A)^2/2}$, which is independent of Δt_f and K [2]. This makes sense. After all, it should not be possible to detect nonlocal correlations locally. *However*, if we can retroactively manipulate the probabilities in Eq. (5.45), we can go beyond this restriction.

Say, the dead time of Alice's photodetector is long enough to filter out every second b-photon. That is, the first b-photon of each bunched pair gets detected, but the second arrives at the photodetector during the time span that it is off and therefore goes undetected. Taking such losses [or *dead-time filtering (DTF)*] into account, we get the new state

$$\tilde{\rho}_{\mathrm{DTF}}^A(t_A) = \frac{P_c\tilde{\rho}_c^A(t_A) + P_b^A\tilde{\rho}_b^A(t_A)}{\mathrm{tr}\big[P_c\tilde{\rho}_c^A(t_A) + P_b^A\tilde{\rho}_b^A(t_A)\big]} \tag{5.50}$$

$$= \begin{pmatrix} |C_H|^2 & C_H C_V^* \kappa_{\mathrm{DTF}}(t_A) \\ C_H^* C_V \kappa_{\mathrm{DTF}}(t_A)^* & |C_V|^2 \end{pmatrix} \tag{5.51}$$

with the new decoherence function

$$\kappa_{\mathrm{DTF}}(t_A) = \frac{3 - e^{-(1-K)(2\pi\sigma\Delta t_f)^2}\cosh[(1-K)(2\pi\sigma)^2\Delta t_f \Delta n t_A]}{3 - e^{-(1-K)(2\pi\sigma\Delta t_f)^2}} \times e^{i2\pi\mu\Delta n t_A - \frac{1}{2}(2\pi\sigma\Delta n t_A)^2}. \tag{5.52}$$

In Fig. 5.10, we have plotted the dead-time filtered trace-distance dynamics of the initial state pair $|\pm\pm\rangle = \frac{1}{2}(|HH\rangle \pm |HV\rangle \pm |VH\rangle + |VV\rangle)$ with different path differences $\Delta x_f = c\Delta t_f$ and correlation coefficients K, which Alice can estimate by fitting $|\kappa_{\mathrm{DTF}}(t_A)|$ to her measurement data. Together, the height and location of the recoherence peak give rough estimates for K and $|\Delta t_f|$, respectively. This goes drastically against the conventional use of HOM interference in parameter estimation. Typically, one can estimate either Δt_f or K by looking at both exit paths. Here, we access *both* by looking at *one* of the exit paths only. Still, Fig. 5.10 tells that our protocol quickly becomes futile with increasing K. This is due to the increasing share of b-photons.

[2] In fact, the same decoherence function could be obtained without the simplifying assumption about the initial polarization state.

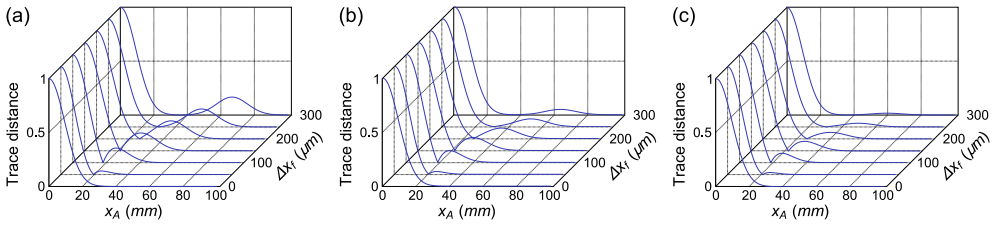

Figure 5.10. Dead-time filtered trace-distance dynamics as functions of $x_A = ct_A$, with different values of $\Delta x_f = c\Delta t_f$ and K. (a) $K = -1.0$, (b) $K = -0.9$, (c) $K = -0.8$. In all panels, $\mu = c/(780\text{ nm})$, $\sigma = 5.68 \times 10^{11}$ Hz, $\Delta n = 0.009$.

Let us take a closer look at how long the dead time should be for our protocol to work. With the maximum thickness d of the birefringent medium, the earliest possible arrival time of the b-photons is, on average, $t_{\text{earliest}} = \min\{n_H, n_V\}d/c$, while the latest possible arrival time is, on average, $t_{\text{latest}} = \max\{n_H, n_V\}d/c + |\Delta t_f|$. Hence, for the second b-photon to arrive at the photodetector during its dead time t_D, we need to have

$$t_D \geq t_{\text{latest}} - t_{\text{earliest}} = \frac{|\Delta n|d}{c} + |\Delta t_f|. \tag{5.53}$$

Note that the photons were treated as localized particles. This is permitted, since detecting one localizes the other (see the earlier discussion in Chapter 4). Note also, that here we considered *ideal* dead-time filtering. That is, c- and b-photons are detected in the ratio of $P_c : P_b^A$. In a more rigorous theory, one should take into account the photon pair production rate of, e.g., SPDC. Namely, it might happen that (future) c-photons are produced right after (future) b-photons so that some of the c-photons remain undetected as well. While this formalization is left for future research, the current study is important for bringing to light the dead time affecting the (observable) open-system dynamics.

5.2.4 Dynamical delayed-choice quantum eraser

In the previous Subsection, we observed that the c- and b-photons behave differently under dephasing. This brings up the possibility of Alice distinguishing between coincidence and bunching events *without communicating with Bob*. In this Subsection, we derive the maximum probability for Alice to do so. To avoid bias, we assume that we are well outside the HOM dip, i.e., $(1 - K)(2\pi\sigma\Delta t_f)^2 \gg 0$, meaning that $P_c \approx P_b \approx 1/2$. Because we are interested in retroactively changing these probabilities, we are actually introducing a new kind of *delayed-choice quantum eraser*. Delayed-choice quantum erasers erase the distinguishing information of the input paths *after* the beam splitter and therefore revive the interference pattern. Commonly, in the case of HOM interference, orthogonal polarizations mark the input

paths, whereas the signature dip (or peak) is revived with polarizers [133]. Here, we mark the input paths with distinct delay and revive the interference pattern with delay-compensating dephasing. Hence, we call our model *dynamical* delayed-choice quantum eraser.

The trace distance of the c- and b-photons' polarization states, which we wish to maximize, is

$$\mathcal{D}_{\text{tr}}\big(\tilde{\rho}_c^A(t_A), \tilde{\rho}_b^A(t_A)\big) = \frac{1}{2}\text{tr}|\tilde{\rho}_c^A(t_A) - \tilde{\rho}_b^A(t_A)| \tag{5.54}$$

$$\approx \big|C_{HH}\big[C_{HV}^* e^{-\frac{1}{2}\gamma_+(t_A)} + C_{VH}^* e^{-\frac{1}{2}\gamma_-(t_A)}\big] + C_{VV}^*\big[C_{HV} e^{-\frac{1}{2}\gamma_+(t_A)} + C_{VH} e^{-\frac{1}{2}\gamma_-(t_A)}\big]\big|, \tag{5.55}$$

where $\gamma_\pm(t_A) = (2\pi\sigma)^2\big[\Delta t_f^2 - 2K\Delta t_f(\Delta t_f \pm \Delta n t_A) + (\Delta t_f \pm \Delta n t_A)^2\big]$. Noticing that when $e^{-\frac{1}{2}\gamma_+(t_A)} = 1$, $e^{-\frac{1}{2}\gamma_-(t_A)} \approx 0$ (and vice versa), we can focus on the terms with $\gamma_+(t_A)$ and set $C_{VH} = 0$. Vertical polarization from path 0 and horizontal polarization from path 1 would never intersect anyway. Simplifying the problem by letting $C_{\lambda_0\lambda_1} \in \mathbb{R}_+$, we obtain the trace distance $1/\sqrt{2}$ with $C_{HH} = C_{VV} = 1/2$, $C_{HV} = 1/\sqrt{2}$, $K = -1$, and $t_A = -2\Delta t_f/\Delta n$. With these values, but keeping the interaction time t_A free, the polarization states corresponding to c- and b-photons read

$$\tilde{\rho}_c^A(t_A) = \frac{1}{2}\begin{pmatrix} 1 & \kappa_-(t_A) \\ \kappa_-(t_A)^* & 1 \end{pmatrix} \tag{5.56}$$

and

$$\tilde{\rho}_b^A(t_A) = \frac{1}{2}\begin{pmatrix} 1 & \kappa_+(t_A) \\ \kappa_+(t_A)^* & 1 \end{pmatrix}, \tag{5.57}$$

where

$$\kappa_\pm(t_A) = \frac{1}{\sqrt{2}} e^{i2\pi\mu\Delta n t_A}\Big[e^{-\frac{1}{2}(2\pi\sigma\Delta n t_A)^2} \pm e^{-\frac{1}{2}(2\pi\sigma)^2(\Delta n t_A + 2\Delta t_f)^2}\Big]. \tag{5.58}$$

In Fig. 5.11, we have plotted $\kappa_\pm(t_A)$, $\mathcal{D}_{\text{tr}}\big(\tilde{\rho}_c^A(t_A), \tilde{\rho}_b^A(t_A)\big)$, and the trajectories of the c- and b-photons' polarization states inside the Bloch ball, when the initial polarization state is $(|\Phi^+\rangle + |HV\rangle)/\sqrt{2}$. From Fig. 5.11, we see that the trajectories of the two polarization states overlap until they first become fully mixed. Then, at the Bloch ball's origin, they split up to opposite directions and experience recoherence.

With equally probable states ρ_1 and ρ_2, the probability to correctly guess the received state is [134]

$$P_{\text{guess}} = \frac{1}{2}\big[1 + \mathcal{D}_{\text{tr}}(\rho_1, \rho_2)\big]. \tag{5.59}$$

Using this property, Alice can revive HOM peaks such as the one shown in Fig. 5.12. An experimental realization would go as follows. After applying dephasing noise for the duration of t_A, Alice could rotate her states $\pi/2$ around the axis $\hat{n} = (\sin\varphi, \cos\varphi,$

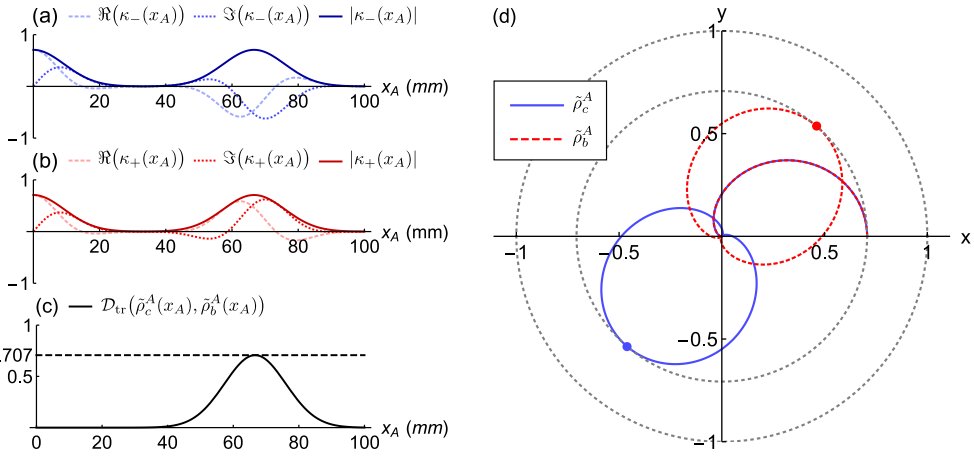

Figure 5.11. Dephasing dynamics of the initial state $(|\Phi^+\rangle+|HV\rangle)/\sqrt{2}$. (a) The c-photon dynamics. (b) The b-photon dynamics. (c) The trace distance of c- and b-photon polarization states. (d) The dephasing dynamics on the xy-plane of the Bloch ball. $\sigma = 5.68 \times 10^{11}$ Hz, $\Delta n = 0.009$, $\Delta x_f = c\Delta t_f = -300$ µm, and $K = -1$. For illustrative purposes, $\mu = \sigma$.

$0)$, where $\varphi = 2\pi\mu\Delta n t_A$, and use a polarizing beam splitter. First, the rotation operator

$$R_{\hat{n}}\left(\frac{\pi}{2}\right) = \frac{1}{\sqrt{2}}\begin{pmatrix} 1 & -e^{i\varphi} \\ e^{-i\varphi} & 1 \end{pmatrix} \tag{5.60}$$

would transform the states $\tilde{\rho}_c^A(t_A)$ and $\tilde{\rho}_b^A(t_A)$ into

$$R_{\hat{n}}\left(\frac{\pi}{2}\right)\tilde{\rho}_c^A(t_A)R_{\hat{n}}\left(\frac{\pi}{2}\right)^\dagger \approx \frac{1}{2}\begin{pmatrix} 1+\frac{1}{\sqrt{2}}e^{-\frac{1}{2}(2\pi\sigma)^2(\Delta n t_A+2\Delta t_f)^2} & 0 \\ 0 & 1-\frac{1}{\sqrt{2}}e^{-\frac{1}{2}(2\pi\sigma)^2(\Delta n t_A+2\Delta t_f)^2} \end{pmatrix} \tag{5.61}$$

and

$$R_{\hat{n}}\left(\frac{\pi}{2}\right)\tilde{\rho}_b^A(t_A)R_{\hat{n}}\left(\frac{\pi}{2}\right)^\dagger \approx \frac{1}{2}\begin{pmatrix} 1-\frac{1}{\sqrt{2}}e^{-\frac{1}{2}(2\pi\sigma)^2(\Delta n t_A+2\Delta t_f)^2} & 0 \\ 0 & 1+\frac{1}{\sqrt{2}}e^{-\frac{1}{2}(2\pi\sigma)^2(\Delta n t_A+2\Delta t_f)^2} \end{pmatrix}. \tag{5.62}$$

Then, after separating the H and V components with a polarizing beam splitter, P_{guess} of all photons in the H (V) branch would be c-photons (b-photons).

The maximum probability achieved at $t_A = -2\Delta t_f/\Delta n$ is $P_{\text{guess}} = (1+\sqrt{2})/(2\sqrt{2}) \approx 0.854$. Should $P_{\text{guess}} = 1$ be possible, the dynamical delayed-choice quantum eraser could be applied in mutual quantum key generation. For example, every time Alice and Bob[3] detect a c-photon in their H branches, they write down

[3] Bob's protocol goes identically.

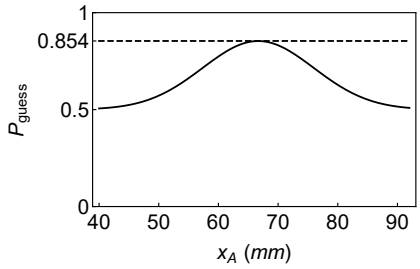

Figure 5.12. HOM peak resulting from the dynamical delayed-choice quantum eraser and the same parameters as in Fig. 5.11. In the H (V) branch of the experimental proposition, P_{guess} is the "revived" P_c (P_b).

"0". And every time they either detect b-photons in their V branches or not, when they ought to, they write down "1". Such a protocol would require at least two ancillas, one for each party, to both increase P_{guess} and let the parties know when to expect a photon(s). Alternatively, one could use nonabsorbing parity detectors to check, whether 0, 1, or 2 photons were present [135]. Such detectors could also be used, at least in theory, to enhance the signal-to-noise ratio in the preceding Subsection, as signal photons would not need to be filtered out.

6 Quantum probing with data processing inequalities

The parameter estimation methods introduced in the previous Chapter were based on sequential measurements under known system-environment coupling. But is it possible to obtain relevant information about some parameter of interest using only *one* point of (interaction) time and an *unknown* system-environment coupling? In this Chapter, we will find out that the answer is *yes*. We begin with a brief introduction to *quantum probing* and *data processing inequalities*, after which we focus on the familiar polarization-frequency interaction model. Finally, we apply our quantum probing protocol in snapshot verification of non-Markovianity.

6.1 Quantum probing and data processing inequalities

In quantum probing, one typically wishes to learn something about a system S without making direct measurements on it [136; 137; 138]; With projective measurements, the state of the system would collapse (see the earlier discussion in Chapter 2). Instead, one can couple the system S with a so-called probe P and measure the latter one. Ideally, the system S gets disturbed only little, and once probed, it still exists. This is in stark contrast to traditional state tomography, where the state of a system can only be reconstructed.

Denoting the initial state of a system S by $\xi(0)$ and the initial state of a probe P by $\rho(0)$, their time-dependent coupling is given by some unitary, $U(t)\rho(0) \otimes \xi(0)U(t)^\dagger$. The state of the probe at some later point of time is then obtained as the usual partial trace, $\rho(t) = \Phi^t\big(\rho(0)\big) = \mathrm{tr}_S[U(t)\rho(0) \otimes \xi(0)U(t)^\dagger]$. With a known coupling, we may be able to say something about $\xi(t)$ after measurements on $\rho(t)$. For example, say we are interested in the standard deviation σ of the frequency distribution of a single photon, which we know to be (sufficiently close to) Gaussian. Then, using the photon's polarization as the probe, and coupling the two in birefringent medium, standard state tomography gives us

$$\sigma = \frac{1}{2\pi|\Delta n|t}\sqrt{\ln\frac{1 - S_3(t)^2}{S_1(t)^2 + S_2(t)^2}}, \tag{6.1}$$

where $S_j(t)$ are time-dependent Stokes parameters. In this example, unfortunately,

the system and probe are carried by the same physical entity, which gets destroyed in each run of standard state tomography.

But what if neither the coupling nor the interaction time are known? Data processing inequalities provide a powerful tool to handle such situations. Consider two system states, ξ_1 and ξ_2, and two probe states, ρ_1 and ρ_2. With ρ_1 interacting with ξ_1 and ρ_2 with ξ_2, it can be shown that [67]

$$\mathcal{F}_\alpha(\rho_1,\rho_2)\mathcal{F}_\alpha(\xi_1,\xi_2) \leq \mathcal{F}_\alpha\big(\Phi_1(\rho_1),\Phi_2(\rho_2)\big) \;\; \forall \alpha \in [1/2,1), \tag{6.2}$$

where $\mathcal{F}_\alpha$ is the so-called α-*fidelity*

$$\mathcal{F}_\alpha(\rho_1,\rho_2) = \mathrm{tr}\Big[\big(\rho_2^{\frac{1-\alpha}{2\alpha}}\rho_1\rho_2^{\frac{1-\alpha}{2\alpha}}\big)^\alpha\Big], \;\; \alpha\in(0,1), \tag{6.3}$$

and Φ_j is a CPTP map induced by ξ_j. With $\alpha = 1/2$, we have $\mathcal{F}_{1/2}(\rho_1,\rho_2) = \sqrt{\mathcal{F}(\rho_1,\rho_2)}$ [see Eq. (4.40)]. We can write similar inequality in terms of the trace distance [68]. Namely,

$$\mathcal{D}_{\mathrm{tr}}\big(\Phi_1(\rho_1),\Phi_2(\rho_2)\big) \leq \mathcal{D}_{\mathrm{tr}}(\rho_1,\rho_2) + \mathcal{D}_{\mathrm{tr}}(\xi_1,\xi_2), \tag{6.4}$$

which reduces to Eq. (3.63) with $\xi_1 = \xi_2$.

Now, the trick is to run a measurement scheme (at least) twice and compare the results using Eq. (6.2) or (6.4). In the first run, we have $\xi_1 = \xi(x,y_1)$. In the second, $\xi_2 = \xi(x,y_2)$. That is, we change some accessible (though not necessarily known) *control parameter* y_j between the runs. Here, x denotes the parameter of interest. Knowing the analytic forms of ξ_j, we may obtain bounds for x by solving $\mathcal{F}_\alpha(\xi_1,\xi_2)$ and $\mathcal{D}_{\mathrm{tr}}(\xi_1,\xi_2)$. With α-fidelity, the α-parameter can be optimized to find the tightest bound(s) as long as it is in the interval $[1/2,1)$. Using the same probe state in both runs ($\rho_1 = \rho_2 =: \rho$), Eqs. (6.2) and (6.4) simplify, as $\mathcal{F}_\alpha(\rho,\rho) = 1$ and $\mathcal{D}_{\mathrm{tr}}(\rho,\rho) = 0$. It is crucial to notice that, although the forms of the system states ξ_j inducing the channels Φ_j are assumed as known, the channels Φ_j themselves *need not be known*. Not knowing them, we pay the price of obtaining only bounds for x instead of exact values.

6.2 Probing of the frequency spectrum

Let us illustrate our probing protocol with two photonic examples. Here, the frequency degree of freedom of a single photon is the system, and the photon's polarization is the probe. In both examples, we use classical frequency states with zero coherences,

$$\xi = \int df |g(f)|^2 |f\rangle\langle f|. \tag{6.5}$$

However, assuming that ξ induces the same channel Φ as the state[1]

$$\xi' = \sum_j p_j \int df df' g_j(f) g_j(f')^* |f\rangle\langle f'|, \tag{6.6}$$

where $\sum_j p_j = 1$ and $\sum_j p_j |g_j(f)|^2 = |g(f)|^2$, our results also hold for ξ' that can be pure. That is, if a probed value of x satisfies the data processing inequalities with frequency states of the form (6.5), it also satisfies them with states of the form (6.6). Furthermore, it can be much easier to solve $\mathcal{F}_\alpha(\xi_1, \xi_2)$ and $\mathcal{D}_{\text{tr}}(\xi_1, \xi_2)$ with the classical states.

Before proceeding with the actual examples, let us prove the (perhaps counter-intuitive) claim about classical states producing tighter bounds than quantum states. Defining the channel Ω with the (uncountable set of) Kraus operators $|f\rangle\langle f|$, we get

$$\Omega(\xi') = \int df |f\rangle\langle f| \sum_j p_j \int df' df'' g_j(f') g_j(f'')^* |f'\rangle\langle f''|f\rangle\langle f| \tag{6.7}$$

$$= \sum_j p_j \int df g_j(f) g_j(f)^* |f\rangle\langle f| \tag{6.8}$$

$$= \int df |g(f)|^2 |f\rangle\langle f|. \tag{6.9}$$

That is, ξ can be obtained from ξ' with a CPTP map. Now, using Eq. (6.2) and equal probe states, we can write

$$\mathcal{F}_\alpha(\xi_1', \xi_2') \leq \mathcal{F}_\alpha\big(\Omega(\xi_1'), \Omega(\xi_2')\big) \tag{6.10}$$

$$= \mathcal{F}_\alpha(\xi_1, \xi_2) \tag{6.11}$$

$$\Leftrightarrow \mathcal{F}_\alpha(\rho_1, \rho_2)\mathcal{F}_\alpha(\xi_1', \xi_2') \leq \mathcal{F}_\alpha(\rho_1, \rho_2)\mathcal{F}_\alpha(\xi_1, \xi_2) \tag{6.12}$$

$$\leq \mathcal{F}_\alpha\big(\Phi_1(\rho_1), \Phi_2(\rho_2)\big). \tag{6.13}$$

In the first row, we used the symmetry of Eq. (6.2); It does not matter whether we have the CPTP map acting on the system or the probe. Similar calculation holds with the trace distance.

6.2.1 Width and distance

Deriving the bounds

Here, we show how to probe the width σ and distance $\Delta\mu := |\mu_1 - \mu_2|$ of two Gaussian frequency distributions $|g_j(f)|^2 = \exp\Big[-\frac{1}{2}\Big(\frac{f-\mu_j}{\sigma}\Big)^2\Big]/\sqrt{2\pi\sigma^2}$, $j = 1, 2$.

[1] This is a reasonable assumption, since partial trace typically ignores coherences.

Associating $|g_j(f)|^2$ with ξ_j, we get

$$\mathcal{F}_\alpha(\xi_1,\xi_2) = \mathrm{tr}\Bigg[\Big(\Big[\int df|g_2(f)|^2|f\rangle\langle f|\Big]^{\frac{1-\alpha}{2\alpha}} \int df'|g_1(f')|^2|f'\rangle\langle f'| \times \Big[\int df''|g_2(f'')|^2|f''\rangle\langle f''|\Big]^{\frac{1-\alpha}{2\alpha}}\Big)^\alpha\Bigg] \tag{6.14}$$

$$= \int df|g_2(f)|^{2(1-\alpha)}|g_1(f)|^{2\alpha} \tag{6.15}$$

$$= e^{-(1-\alpha)\alpha\frac{\Delta\mu^2}{2\sigma^2}}. \tag{6.16}$$

Then, substituting Eq. (6.16) in Eq. (6.2) yields

$$\frac{\Delta\mu}{\sigma} \geq \sqrt{\frac{2}{\alpha(\alpha-1)}\ln\left[\frac{\mathcal{F}_\alpha\big(\Phi_1(\rho_1),\Phi_2(\rho_2)\big)}{\mathcal{F}_\alpha(\rho_1,\rho_2)}\right]}. \tag{6.17}$$

For this inequality to be useful at all, the argument of the logarithm needs to be at most one.

If either the width or distance is known, we can move it to the right-hand side of Eq. (6.17) and estimate the remaining one. In the following experiment, for example, we are only interested in σ, for which we get the inequality

$$\sigma \leq \sqrt{\frac{\alpha(\alpha-1)\Delta\mu^2}{2\ln\left[\mathcal{F}_\alpha\big(\Phi_1(\rho_1),\Phi_2(\rho_2)\big)/\mathcal{F}_\alpha(\rho_1,\rho_2)\right]}}. \tag{6.18}$$

Actually, because the α-fidelity is not symmetric with respect to its inputs, Eq. (6.18) might not give the tightest bound. Defining

$$B_1 := \sqrt{\frac{\alpha(\alpha-1)\Delta\mu^2}{2\ln\left[\mathcal{F}_\alpha\big(\Phi_1(\rho_1),\Phi_2(\rho_2)\big)/\mathcal{F}_\alpha(\rho_1,\rho_2)\right]}}, \tag{6.19}$$

$$B_2 := \sqrt{\frac{\alpha(\alpha-1)\Delta\mu^2}{2\ln\left[\mathcal{F}_\alpha\big(\Phi_2(\rho_2),\Phi_1(\rho_1)\big)/\mathcal{F}_\alpha(\rho_2,\rho_1)\right]}}, \tag{6.20}$$

and $B_{\text{inf}} := \inf\{B_1, B_2\}$, we get $\sigma \leq B_{\text{inf}}$.

Experimental setup

The experimental setup is presented in Fig. 6.1. The photon source (PS) is a type-I BBO crystal, which we pump with a continuous-wave laser of the wavelength 405 nm. The crystal randomly produces photon pairs of the wavelength 810 nm through

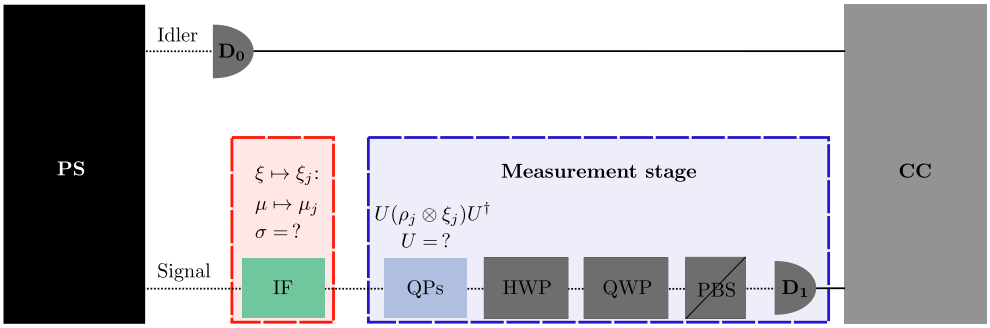

Figure 6.1. Experimental setup of probing σ. Photon pairs are produced in PS. The idler photons go to detector D_0, triggering CC to expect the signal photons. The frequency states ξ_j of the signal photons are produced with an IF modifying μ_j but keeping σ intact. The probe states ρ_j are coupled with ξ_j in QPs, whose total thickness and rotation angles we can control, allowing us to choose between known and unknown coupling. Finally, HWP, QWP, and PBS are used in state tomography.

the SPDC process. The idler photons in the upper branch are registered by the single-photon detector D_0, triggering the coincidence counting electronics (CC) to monitor the single-photon detector D_1 for data collection of the signal photons. The signal photons' polarization is prepared to the initial probe state $\rho_1 = \rho_2 = |+\rangle\langle+|$ by guiding the photons through a polarizer in PS. Then, the signal photons proceed to an IF. Tilting the IF changes its transmission bandwidth and, consequently, the central frequencies μ_j of the frequency spectra, while keeping their standard deviation σ constant. This allows us to control $\Delta\mu$ and prepare the initial frequency states ξ_1 and ξ_2. Note that $\Delta\mu$ needs to be nonzero for our protocol to work. We fixed it as $\Delta\mu = 7.95 \times 10^{11}$ Hz.

The system (frequency) and probe (polarization) are coupled, when the signal photons travel through birefringent quartz plates (QPs). This creates the channels Φ_1 and Φ_2 that change the probe states ρ_1 and ρ_2, respectively. After the quartz plates, we perform standard polarization tomography on the states $\Phi_1(\rho_1)$ and $\Phi_2(\rho_2)$ by passing the signal photons through a combination of HWP, QWP, and PBS. With each measurement basis, we used the data accumulation time of 60 s. We used multiple different thicknesses and orientations of quartz plates, corresponding to different system-probe couplings U.

In what follows, we shall refer to parallel quartz plates as "known coupling". However, we emphasize that the coupling need not be known; We do not use the known forms of Φ_j as in Eq. (6.1). Hence, they might as well be unknown. A *truly* unknown coupling can be implemented with randomly oriented quartz plates.

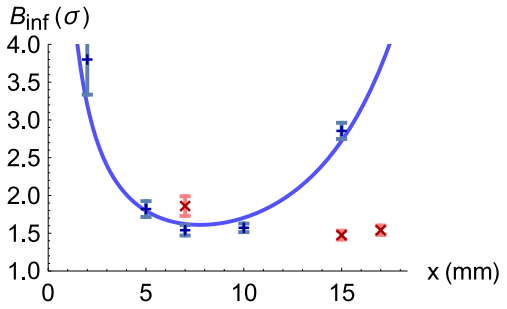

Figure 6.2. Upper bounds of σ as functions of the thickness of quartz, in units of the actual value of σ. Blue crosses correspond to known coupling (with the blue curve being the theoretical prediction), while red slanted crosses correspond to unknown coupling. The error bars were calculated using a similar Monte Carlo method to that given by Eq. (5.23).

Experimental results

The experimental results are shown in Fig. 6.2. The blue crosses are the upper bounds B_{inf} with known coupling, i.e., quartz plates in the same orientation, while the red slanted crosses correspond to (truly) unknown coupling, i.e., randomly rotated quartz plates. The upper bounds are given in units of the actual value of σ, which was determined to be 5.68×10^{11} Hz. At each measurement point, tightest bounds were given by $\alpha \approx 0.999$. We repeated the measurements with the integration time of 10 s, resulting in bounds differing only by 4.19 % from the bounds in Fig. 6.2, on average. This goes to illustrate the robustness of our probing protocol.

Because of the (nearly) identical probe states, $\mathcal{F}_\alpha\big(\Phi_1(\rho_1), \Phi_2(\rho_2)\big)$ is only slightly smaller than $\mathcal{F}_\alpha(\rho_1, \rho_2)$ with short interaction times, and similarly with the other order of the inputs. Hence, the logarithms in Eqs. (6.19) and (6.20) start from close to zero, and the bounds are quite large. With long interaction times, both probe states become fully mixed and $\mathcal{F}_\alpha\big(\Phi_1(\rho_1), \Phi_2(\rho_2)\big) \approx \mathcal{F}_\alpha(\rho_1, \rho_2) \approx 1$. Hence, the logarithms in Eqs. (6.19) and (6.20) are again close to zero, meaning large bounds. At 20 mm of quartz, we obtained $\mathcal{F}_\alpha\big(\Phi_1(\rho_1), \Phi_2(\rho_2)\big) > \mathcal{F}_\alpha(\rho_1, \rho_2)$, so the protocol did not give real-valued bounds.

It is in between that $\mathcal{F}_\alpha\big(\Phi_1(\rho_1), \Phi_2(\rho_2)\big)$ differentiates the most from $\mathcal{F}_\alpha(\rho_1, \rho_2)$. With known coupling, the tightest bound is achieved at 7 mm of quartz. Strikingly, at 15 mm, the unknown coupling gives much tighter bounds than the known coupling, $1.5\sigma < 2.9\sigma$. It would be an interesting task, e.g., for machine learning to find the coupling giving the smallest upper bound.

6.2.2 Convex coefficients

Deriving the bounds

Here, we show how to probe the convex coefficient A of the convex combination $\xi_1 = A\xi_2 + (1-A)\xi_3$, where the frequency distributions of ξ_2 and ξ_3 are Gaussians of the same width but different central frequency, $\mu_2 \neq \mu_3$. This time, by using three probe states and A itself as the control parameter, we obtain both upper and lower bounds for A.

Using the states ξ_1 (unknown A) and ξ_2 ($A = 1$), we get

$$\begin{aligned}
\mathcal{F}_\alpha(\xi_1,\xi_2) &= \mathrm{tr}\Bigg[\Big(\Big[\int df|g_2(f)|^2|f\rangle\langle f|\Big]^{\frac{1-\alpha}{2\alpha}}\Big[A\int df'|g_2(f')|^2|f'\rangle\langle f'| \\
&\quad + (1-A)\int df'|g_3(f')|^2|f'\rangle\langle f'|\Big]\Big[\int df''|g_2(f'')|^2|f''\rangle\langle f''|\Big]^{\frac{1-\alpha}{2\alpha}}\Big)^\alpha\Bigg] \qquad (6.21)\\
&= \mathrm{tr}\Bigg[\Big(A\int df|g_2(f)|^{\frac{2}{\alpha}}|f\rangle\langle f| \\
&\quad + (1-A)\int df|g_2(f)|^{\frac{2(1-\alpha)}{\alpha}}|g_3(f)|^2|f\rangle\langle f|\Big)^\alpha\Bigg] \qquad (6.22)\\
&\geq \mathrm{tr}\Big[A^\alpha\int df|g_2(f)|^2|f\rangle\langle f|\Big] \qquad (6.23)\\
&= A^\alpha \qquad (6.24)\\
\Leftrightarrow A &\leq \Big[\mathcal{F}_\alpha(\xi_1,\xi_2)\Big]^{\frac{1}{\alpha}} \qquad (6.25)\\
&\leq \left[\frac{\mathcal{F}_\alpha\big(\Phi_1(\rho_1),\Phi_2(\rho_2)\big)}{\mathcal{F}_\alpha(\rho_1,\rho_2)}\right]^{\frac{1}{\alpha}}. \qquad (6.26)
\end{aligned}$$

Similar calculation with the states ξ_1 (unknown A) and ξ_3 ($A = 0$) yields

$$A \geq 1 - \left[\frac{\mathcal{F}_\alpha\big(\Phi_1(\rho_1),\Phi_3(\rho_3)\big)}{\mathcal{F}_\alpha(\rho_1,\rho_3)}\right]^{\frac{1}{\alpha}}. \qquad (6.27)$$

Using the trace distance instead, the state pair ξ_1 and ξ_2 gives

$$\begin{aligned}
\mathcal{D}_{\mathrm{tr}}(\xi_1,\xi_2) &= \frac{1}{2}\mathrm{tr}\Big|\int df\Big[(A-1)|g_2(f)|^2 + (1-A)|g_3(f)|^2\Big]|f\rangle\langle f|\Big| \qquad (6.28)\\
&\leq \frac{1-A}{2}\mathrm{tr}\Big[\int df\Big(|g_2(f)|^2 + |g_3(f)|^2\Big)|f\rangle\langle f|\Big] \qquad (6.29)\\
&= 1-A \qquad (6.30)\\
\Leftrightarrow A &\leq 1 - \mathcal{D}_{\mathrm{tr}}(\xi_1,\xi_2) \qquad (6.31)
\end{aligned}$$

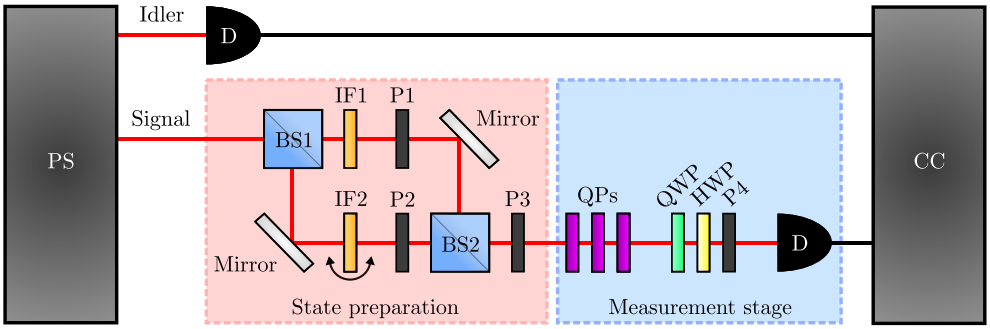

Figure 6.3. Experimental setup of probing A. Photon pairs are produced in PS. The idler photons trigger CC to expect the signal photons. The frequency states of the signal photons are produced with a MZ interferometer, inside of which we can control the distance of the Gaussian peaks with IFs and their heights with the polarizers P1, P2, and P3. The probe states are coupled with the system states in QPs. Finally, HWP, QWP, and P4 are used in state tomography.

$$\leq 1 - \mathcal{D}_{\mathrm{tr}}\big(\Phi_1(\rho_1), \Phi_2(\rho_2)\big) + \mathcal{D}_{\mathrm{tr}}\big(\rho_1, \rho_2\big) \tag{6.32}$$

and the states ξ_1 and ξ_3

$$A \geq \mathcal{D}_{\mathrm{tr}}\big(\Phi_1(\rho_1), \Phi_3(\rho_3)\big) - \mathcal{D}_{\mathrm{tr}}\big(\rho_1, \rho_3\big). \tag{6.33}$$

Combining all the above results, we obtain the following bounds for A:

$$1 - \left[\frac{\mathcal{F}_{\alpha_3}\big(\Phi_1(\rho_1), \Phi_3(\rho_3)\big)}{\mathcal{F}_{\alpha_3}(\rho_1, \rho_3)}\right]^{\frac{1}{\alpha_3}} \leq A \leq \left[\frac{\mathcal{F}_{\alpha_2}\big(\Phi_1(\rho_1), \Phi_2(\rho_2)\big)}{\mathcal{F}_{\alpha_2}(\rho_1, \rho_2)}\right]^{\frac{1}{\alpha_2}}, \tag{6.34}$$

$$\mathcal{D}_{\mathrm{tr}}\big(\Phi_1(\rho_1), \Phi_3(\rho_3)\big) - \mathcal{D}_{\mathrm{tr}}\big(\rho_1, \rho_3\big) \leq A \leq 1 - \mathcal{D}_{\mathrm{tr}}\big(\Phi_1(\rho_1), \Phi_2(\rho_2)\big) + \mathcal{D}_{\mathrm{tr}}\big(\rho_1, \rho_2\big). \tag{6.35}$$

Note that we need not have $\alpha_2 = \alpha_3$. Therefore, the α-parameters in Eq. (6.34) can be optimized independently of each other to find the tightest bounds. Note also, that here we need not know μ_2, μ_3, or σ.

Our protocol can be applied with any number of convex coefficients. With N coefficients, we would have

$$\xi_1 = \sum_{j=2}^{N+1} A_j \xi_j, \tag{6.36}$$

and so we would need $N + 2$ probe states, one for each frequency state appearing in Eq. (6.36).

Experimental setup

The experimental setup is presented in Fig. 6.3. The signal and idler photons are produced as before. Again, all the probe states are approximately $|+\rangle\langle+|$. We choose

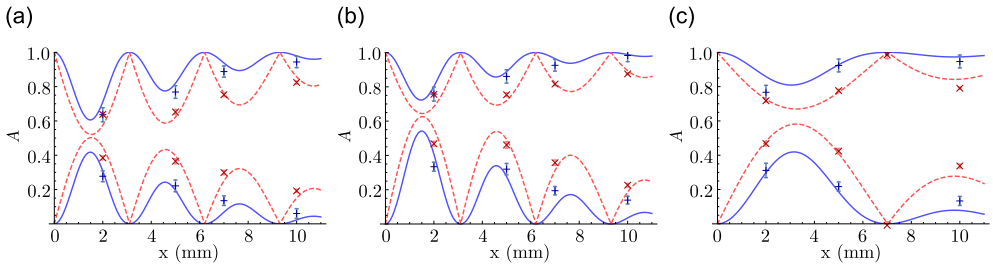

Figure 6.4. Experimental results of probing A. Blue crosses = experimental bounds obtained with α-fidelity [Eq. (6.34)]. Blue curves = theoretical predictions of the α-fidelity bounds. Red, slanted crosses = experimental bounds obtained with trace distance [Eq. (6.35)]. Red, dashed durves = theoretical predictions of the trace-distance bounds. The error bars were calculated with the same Monte Carlo method as previously. (a) $\mu_2 = c/(810\text{ nm})$, $\mu_3 = c/(830\text{ nm})$, and $A = 0.5122$. (b) $\mu_2 = c/(810\text{ nm})$, $\mu_3 = c/(830\text{ nm})$, and $A = 0.6377$. (c) $\mu_2 = c/(810\text{ nm})$, $\mu_3 = c/(820\text{ nm})$, and $A = 0.6377$.

to use $|+\rangle\langle+|$ due to the known interaction being dephasing. The system state ξ_1 is prepared by guiding the signal photons through a MZ interferometer, inside of which we have two IFs and two polarizers (P). The IFs are used to control the central frequencies, while the polarizers—together with the polarizer P3 following the interferometer—are used to control the convex coefficient. ξ_2 is prepared by blocking the lower path, and ξ_3 is prepared by blocking the upper path.

After state preparation, we couple the system (frequency) and probe (polarization) in quartz plates, with identical alignment corresponding to known coupling and random to unknown. Finally, we perform standard polarization tomography and obtain the evolved probe states $\Phi_1(\rho_1)$, $\Phi_2(\rho_2)$, and $\Phi_3(\rho_3)$.

Experimental results

The experimental results are shown in Fig. 6.4. Here, we considered different central frequencies μ_2 and μ_3, convex coefficients A, and both the α-fidelities (blue crosses and solid curves) and trace distances (red, slanted crosses and dashed curves). Clearly, in each case, trace distance gives tighter bounds than α-fidelity. In Figs. 6.4(a) and (b), at 1.5 mm of quartz, the theoretical predictions (curves) leave particularly little room for the convex coefficient. With α-fidelity, the tightest bounds were obtained with $\alpha_2 = \alpha_3 = 1/2$.

In Fig. 6.4, $\Delta\mu := |\mu_2 - \mu_3|$ gives the oscillation frequency of the bounds. As we favor μ_2 over μ_3 by increasing A in Fig. 6.4(b), $\Phi_1(\rho_1)$ approaches $\Phi_2(\rho_2)$, meaning larger $\mathcal{F}_{\alpha_2}\big(\Phi_1(\rho_1), \Phi_2(\rho_2)\big)$ and smaller $\mathcal{D}_{\text{tr}}\big(\Phi_1(\rho_1), \Phi_2(\rho_2)\big)$. Hence, the upper bounds become looser. At the same time, $\Phi_1(\rho_1)$ distances from $\Phi_3(\rho_3)$, and the lower bounds become tighter. Moreover, as we bring the two peaks closer to each other in Fig. 6.4(c), the oscillation frequency $\Delta\mu$ decreases.

We also ran the experiments with randomly rotated quartz plates, but this time the bounds became looser.

6.3 Snapshot verification of non-Markovianity

In Chapter 3, we had the example of a double-peaked Gaussian giving rise to non-monotonic trace-distance dynamics, i.e., non-Markovianity. Here, at last, we define the non-Markovian parameter space of this model. Using the familiar single-photon dephasing model, we have $\kappa_j(t) = e^{i2\pi\mu_j\Delta nt-(2\pi\sigma\Delta nt)^2/2}$ for the Gaussian spectrum centered around μ_j. So, having a double-peaked Gaussian with the weights A and $1-A$, we obtain

$$\kappa_1(t) = A\kappa_2(t) + (1-A)\kappa_3(t) \tag{6.37}$$

$$\begin{aligned}\Rightarrow |\kappa_1(t)| = \Big[&A^2e^{-(2\pi\sigma\Delta nt)^2} + (1-A)^2e^{-(2\pi\sigma\Delta nt)^2} \\ &+ 2A(1-A)\cos(2\pi\Delta\mu\Delta nt)e^{-(2\pi\sigma\Delta nt)^2}\Big]^{\frac{1}{2}}\end{aligned} \tag{6.38}$$

$$= \sqrt{1-2h(A)+2h(A)\cos(2\pi\Delta\mu\Delta nt)}e^{-\frac{1}{2}(2\pi\sigma\Delta nt)^2}, \tag{6.39}$$

where $h(A) := A(1-A)$ and $\Delta\mu := |\mu_2 - \mu_3|$.

Let us proceed by deriving the values of A with which $|\kappa_1(t)|$ increases. In the following, we will also use $\theta(\Delta\mu, \sigma, \Delta nt) := 4\pi\sigma^2\Delta nt - 4\pi\sigma^2\Delta nt\cos(2\pi\Delta\mu\Delta nt) - \Delta\mu\sin(2\pi\Delta\mu\Delta nt)$.

$$\begin{aligned}\frac{\partial}{\partial t}|\kappa_1(t)| = &-\frac{h(A)2\pi\Delta\mu\Delta n\sin(2\pi\Delta\mu\Delta nt)}{\sqrt{1-2h(A)+2h(A)\cos(2\pi\Delta\mu\Delta nt)}}e^{-\frac{1}{2}(2\pi\sigma\Delta nt)^2} \\ &- \sqrt{1-2h(A)+2h(A)\cos(2\pi\Delta\mu\Delta nt)}(2\pi\sigma\Delta n)^2te^{-\frac{1}{2}(2\pi\sigma\Delta nt)^2} > 0\end{aligned} \tag{6.40}$$

$$\begin{aligned}\Leftrightarrow 0 < &-h(A)\Delta\mu\sin(2\pi\Delta\mu|\Delta n|t) \\ &- [1-2h(A)+2h(A)\cos(2\pi\Delta\mu\Delta nt)]2\pi\sigma^2|\Delta n|t\end{aligned} \tag{6.41}$$

$$= h(A)\theta(\Delta\mu, \sigma, |\Delta n|t) - 2\pi\sigma^2|\Delta n|t \tag{6.42}$$

$$\Leftrightarrow \begin{cases} h(A) > \frac{2\pi\sigma^2|\Delta n|t}{\theta(\Delta\mu,\sigma,|\Delta n|t)} \text{ if } \theta(\Delta\mu,\sigma,|\Delta n|t) > 0, \\ h(A) < \frac{2\pi\sigma^2|\Delta n|t}{\theta(\Delta\mu,\sigma|\Delta n|t)} \text{ if } \theta(\Delta\mu,\sigma,|\Delta n|t) < 0. \end{cases} \tag{6.43}$$

The bottom row can be omitted, because with $2\pi\sigma^2|\Delta n|t > 0$, $\theta(\Delta\mu, \sigma, |\Delta n|t) < 0$ would imply that $h(A) < 0$, which is clearly false with $0 \le A \le 1$.

Fitting on the minimum values of A that satisfy (the upper row of) Eq. (6.43) with different values of $\Delta\eta := \Delta\mu/\sigma$, we obtain the following pseudo-Voigt form for the critical convex coefficient,

$$A_{\text{crit}}(\Delta\eta) \approx 0.0885553e^{-0.0870419\Delta\eta^2} + \frac{0.411445}{1+0.0845395\Delta\eta^2}. \tag{6.44}$$

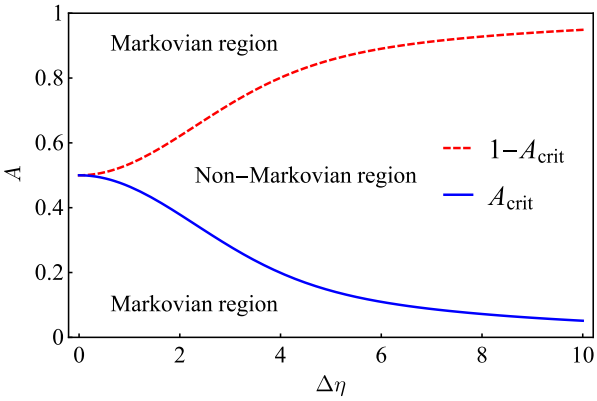

Figure 6.5. Markovian and non-Markovian regions of the double-peaked Gaussian dephasing.

Because of the symmetry of $h(A)$, the maximum values of A satisfying Eq. (6.43) are given by $1 - A_{\text{crit}}(\Delta\eta)$. Hence, if $A_{\text{crit}}(\Delta\eta) \leq A \leq 1 - A_{\text{crit}}(\Delta\eta)$ with a given value of $\Delta\eta$, we know that the dephasing dynamics is non-Markovian. The Markovian and non-Markovian $(\Delta\eta, A)$-regions are illustrated in Fig. 6.5.

Commonly, it would require at least two measurement points to witness increasing magnitude of the decoherence function and verify non-Markovianity. However, in the previous Section we saw how to probe both $\Delta\eta$ and A using only one point of interaction time. If the parameters can be enclosed to one of the regions in Fig. 6.5, we can conclusively say if the probe (polarization) dynamics $\Phi_1(\rho_1)$ is Markovian or non-Markovian.

Plugging the probe states ρ_2, ρ_3, $\Phi_2(\rho_2)$, and $\Phi_3(\rho_3)$ of Subsection 6.2.1 in Eq. (6.17), we get lower bounds for $\Delta\eta$. And plugging these lower bounds in Eq. (6.44), we get tighter critical convex coefficients than their real values. If the probed bounds of A are between these tighter values, they are also between the real values, and the probe dynamics is non-Markovian.

Using the same experimental setup as in Subsection 6.2.1, we get the results presented in Fig. 6.6. This figure is essentially the same as Fig. 6.4, but here we also have the probed values of A_{crit} and $1 - A_{\text{crit}}$. It is interesting to notice that, when probing A_{crit} and $1 - A_{\text{crit}}$, tightest bounds are given by $\alpha \approx 0.999$, while $\alpha_2 = \alpha_3 = 1/2$ is used with A.

In almost all cases, the probed bounds of A are between the tight estimates of A_{crit} and $1 - A_{\text{crit}}$, and we can verify non-Markovianity. In some cases, bounds obtained with α-fidelity fail in this task, but it is only in Fig. 6.6(c), at 7 mm of quartz, that our protocol completely fails. We also ran the experiments with an unknown coupling, ending up on the non-Markovian region using known $\Delta\eta$. With an unknown $\Delta\eta$, we could not say anything conclusive about (non-)Markovianity. It is important to notice that, although the parameters can be probed with an unknown

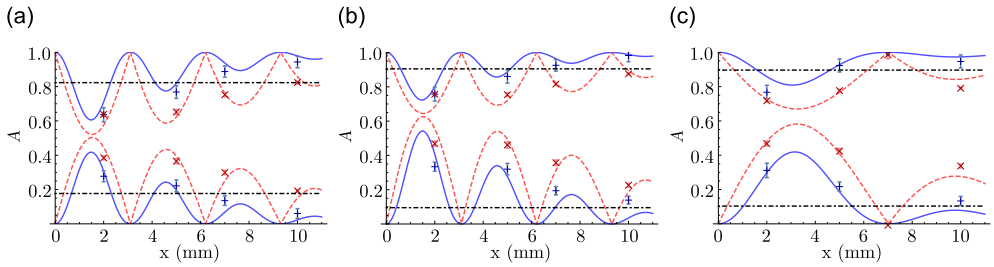

Figure 6.6. Verification of non-Markovianity. The black dash-dotted lines are the probed values of A_{crit}. If the probed bounds of A are inside the probed region $[A_{\text{crit}}, 1 - A_{\text{crit}}]$, the dynamics of the probe state ρ_1 is guaranteed to be non-Markovian. If the upper bound of A is below the *known* A_{crit} or the lower bound of A is above the *known* $1 - A_{\text{crit}}$, the dynamics is Markovian. Otherwise, the result is inconclusive. (a) $\mu_2 = c/(810\text{ nm})$, $\mu_3 = c/(830\text{ nm})$, and $A = 0.5122$. (b) $\mu_2 = c/(810\text{ nm})$, $\mu_3 = c/(830\text{ nm})$, and $A = 0.6377$. (c) $\mu_2 = c/(810\text{ nm})$, $\mu_3 = c/(820\text{ nm})$, and $A = 0.6377$.

coupling, here we are always interested in the *known* coupling's (non-)Markovianity; We are not claiming anything about the unknown coupling's (non-)Markovianity.

In none of the cases of Fig. 6.6 can we place A below the probed A_{crit} or above the probed $1 - A_{\text{crit}}$. And even if we could, *we could not verify Markovianity*; Say, both of the probed bounds of A lied below the probed value of A_{crit}. Now, it would be tempting to call the probe dynamics Markovian. However, the *actual* value of A_{crit} can still lie between the probed bounds—not above them—and hence we cannot really make such a conclusion.

Even if $\Delta\eta$ and A_{crit} were known, it would be challenging to confirm global Markovianity. In fact, with known coupling and equal probe states $\rho_1 = \rho_2 = \rho_3 =: \rho = |+\rangle\langle+|$, our protocol can be shown to fail at this task. To verify Markovianity with α-fidelities, we would need to have either $\mathcal{F}_{\alpha_2}\big(\Phi_1(\rho), \Phi_2(\rho)\big)^{\frac{1}{\alpha_2}} < A_{\text{crit}}$ or $1 - \mathcal{F}_{\alpha_3}\big(\Phi_1(\rho), \Phi_3(\rho)\big)^{\frac{1}{\alpha_3}} > 1 - A_{\text{crit}}$. From Fig. 6.7, we see that neither can be achieved. The blue dots in Fig. 6.7 are the smallest possible upper bounds $\mathcal{F}_{\alpha_2}\big(\Phi_1(\rho), \Phi_2(\rho)\big)^{\frac{1}{\alpha_2}}$—obtained by $\alpha_2 = 1/2$, $A = 0$, and minimizing over time—while the diamonds are the (actual, not probed) critical convex coefficients A_{crit}. The cyan curve is $\frac{1}{2}\min_t\big\{\mathcal{F}_{1/2}\big(\Phi_1(\rho), \Phi_2(\rho)\big)^2\big|_{A=0}\big\}$, which happens to agree excellently with A_{crit}. Thus, we have

$$\mathcal{F}_{\alpha_2}\big(\Phi_1(\rho), \Phi_2(\rho)\big)^{\frac{1}{\alpha_2}} \geq \min_t\big\{\mathcal{F}_{1/2}\big(\Phi_1(\rho), \Phi_2(\rho)\big)^2\big|_{A=0}\big\} \tag{6.45}$$

$$\approx 2A_{\text{crit}} > A_{\text{crit}}. \tag{6.46}$$

Similarly, the red dots in Fig. 6.7 are the largest possible lower bounds $1 - \mathcal{F}_{\alpha_3}\big(\Phi_1(\rho), \Phi_3(\rho)\big)^{\frac{1}{\alpha_3}}$—obtained by $\alpha_3 = 1/2$, $A = 1$, and maximizing over time—while the squares are the (actual, not probed) critical convex coefficients $1 - A_{\text{crit}}$. The pink curve is $\frac{1}{2}\Big[\max_t\big\{1 - \mathcal{F}_{1/2}\big(\Phi_1(\rho), \Phi_3(\rho)\big)^2\big|_{A=1}\big\} + 1\Big]$, which happens to

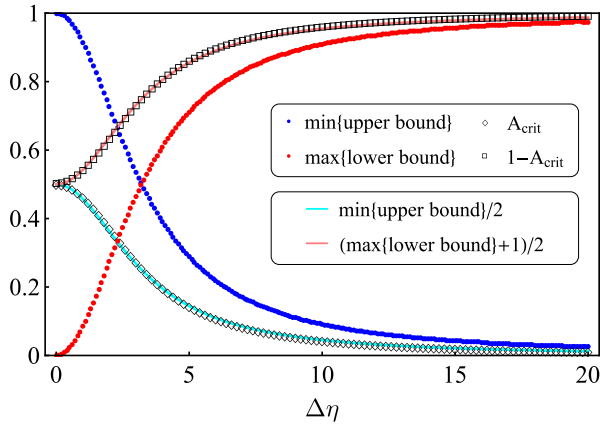

Figure 6.7. The tightest possible bounds of A (blue and red dots), twice as tight "bounds" (cyan and pink curves), and the critical convex coefficients A_{crit} and $1 - A_{\text{crit}}$ (diamonds and squares) as functions of $\Delta\eta$. The bounds were optimized with respect to time, α, and A independently.

agree excellently with $1 - A_{\text{crit}}$. Thus, we have

$$1 - \mathcal{F}_{\alpha_3}\big(\Phi_1(\rho), \Phi_3(\rho)\big)^{\frac{1}{\alpha_3}} \leq \max_t \left\{1 - \mathcal{F}_{1/2}\big(\Phi_1(\rho), \Phi_3(\rho)\big)^2\big|_{A=1}\right\} \tag{6.47}$$

$$\approx 1 - 2A_{\text{crit}} < 1 - A_{\text{crit}}. \tag{6.48}$$

Even the trace distance can be shown to fail at verifying global Markovianity (see Publication **VII**). However, one might succeed in this task by carefully optimizing the initial probe states and the rotation angles of the quartz plates.

Even though it appears to be somewhat difficult to verify global Markovianity with our protocol, with known $\Delta\eta$ it can give Markovian and non-Markovian *intervals*. Clearly, the time intervals during which no A satisfies Eq. (6.43) are Markovian, and we need not probe anything. The non-Markovian time intervals, on the other hand, can be verified by comparing the probed bounds of A with the *time-dependent* coefficients $A_{\text{crit}}(t)$. $A_{\text{crit}}(t)$ can be solved from Eq. (6.43) numerically. For clarity, the minimum values A_{crit} given by Eq. (6.44) tell whether $|\kappa_1(t)|$ can increase at all with given A, while $A_{\text{crit}}(t)$ tells if $|\kappa_1(t)|$ is increasing at t with given A. That is,

$$A \in [A_{\text{crit}}, 1 - A_{\text{crit}}] \Rightarrow \text{global non-Markovianity},$$
$$A \in [A_{\text{crit}}(t), 1 - A_{\text{crit}}(t)] \Rightarrow \text{local non-Markovianity at } t.$$

The time intervals during which A can be placed inside $[A_{\text{crit}}(t), 1 - A_{\text{crit}}(t)]$ with certainty are non-Markovian. In any other situation, we cannot classify the time interval.

We have plotted $A_{\text{crit}}(t)$ in Fig. 6.8(a) with different values of $\Delta\eta$. As one might expect, the bigger the $\Delta\eta$, the more oscillations of $|\kappa_1(t)|$ we can have during the same time span. The black line marks the value of $\Delta\eta$ used in Fig. 6.8(b), where

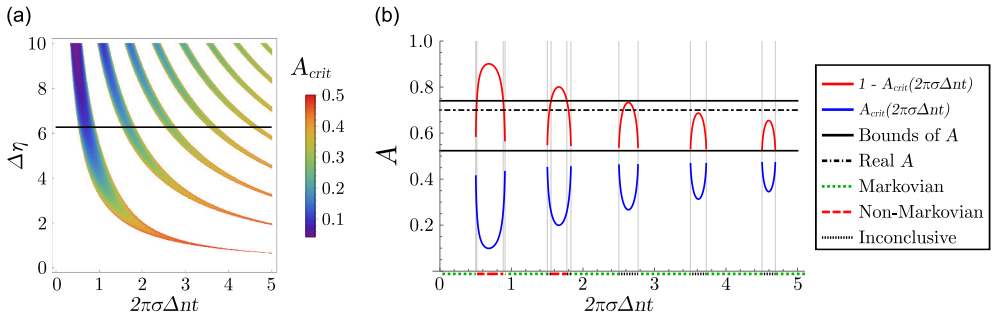

Figure 6.8. Probing Markovian and non-Markovian time intervals. (a) A_{crit} as a function of $\Delta\eta$ and the scaled interaction time $2\pi\sigma\Delta nt$. On the white regions, the probe dynamics is Markovian regardless of the convex coefficient. On the colored regions, the probe dynamics is non-Markovian if $A \in [A_{\text{crit}}(t), 1-A_{\text{crit}}(t)]$. The horizontal line indicates the value of $\Delta\eta$ used in panel (b). (b) Probing results. When the probed bounds of A are in $[A_{\text{crit}}(t), 1 - A_{\text{crit}}(t)]$, we know that the dynamics is non-Markovian. These time intervals are indicated with red dashed lines. When $A_{\text{crit}}(t)$ cannot be determined, we know that the dynamics is Markovian. These time intervals are indicated with green dotted lines. Otherwise, we cannot say if the dynamics is Markovian or non-Markovian (black, vertical lines). $\mu_2 = c/(810\text{ nm})$, $\mu_2 = c/(818\text{ nm})$, and $A = 0.7$.

we have plotted the corresponding $A_{\text{crit}}(t)$, $1 - A_{\text{crit}}(t)$, and the probed bounds of A. The probed bounds were obtained with 5 mm of parallel quartz plates and trace distance, i.e., Eq. (6.35). As in Fig. 6.8(a), there are time intervals with undefined $A_{\text{crit}}(t)$, guaranteeing local Markovianity.

The blue and red solid curves in Fig. 6.8(b) give the non-Markovian regions $[A_{\text{crit}}(t), 1 - A_{\text{crit}}(t)]$, and the black dash-dotted line is the actual value of A in the experiment. The actual value of A is between $A_{\text{crit}}(t)$ and $1 - A_{\text{crit}}(t)$ on three time intervals, during which the probe dynamics is really non-Markovian. Looking at the probed bounds of A instead, given by the black solid lines, we see that both of them are (almost entirely) inside $[A_{\text{crit}}(t), 1-A_{\text{crit}}(t)]$ for the first two non-Markovian intervals. This means that these time intervals can be verified as non-Markovian with our probing method. For the three potentially non-Markovian intervals at $2\pi\sigma\Delta nt \in [2, 5]$, the probed upper bound is above $1 - A_{\text{crit}}(t)$, so the dynamics can be either Markovian or non-Markovian.

Although our probing protocol does not require multiple points of interaction time, it requires multiple measurements at the same interaction time. Future studies show if our protocol can be developed further, using less measurements and assumptions. Could we, for example, relax assumptions on the system state's analytic form? Another interesting prospect would be that concerning entangled ancillas: Could we achieve higher precision with entangled ancillas, as in [139]? Or could we probe the degree of entanglement with our protocol?

7 Conclusions

In this Thesis, we studied various effects of reservoir engineering on decoherence in the linear optical open-system model of polarization (system) interacting with frequency (environment). Although the open-system dynamics in our case is highly controllable—demoting the linear optical model to a simulator—it is the very control in question that allows us to develop new, proof-of-concept methods to manage decoherence, in which there is value too. But perhaps more interestingly, the model lets us study the *benefits* of decoherence.

We began the Thesis in Chapters 2 and 3 with brief introductions to the basics of quantum theory and open quantum systems, respectively. In the rest of the Thesis, we presented the results of the Publications **I**–**VII**.

Chapter 4 was based on Publications **I** and **II**. Here, we focused on the initial polarization-frequency correlations of a biphoton system. Controlling them with SLMs allows us to tailor the dephasing dynamics of polarization to our liking. In particular, we introduced three phase functions responsible for the said correlations. The zigzag and quadratic phases, together with initial frequency correlations and their mixtures, allow us to control the monotonicity of all the four decoherence functions independently of each other. That is, we can select the open-system subspaces experiencing information backflow, i.e., non-Markovian memory effects when using the BLP definition. Hence, we actually go beyond the prior classification of memory effects being only local or nonlocal. As an application, we proposed encoding information to the memory partitions. However, although the number of memory partitions—and hence the information capacity—grows rapidly with the number of qubits, the encoding protocol ought to be generalized and the decoding protocol made more feasible. Perhaps similar snapshot methods to that presented in Chapter 6 or different physical platforms might be of help.

As for the third phase function, we considered the linear, decoherence-reversing function. This function allows us to distribute any number of polarization qubits across dephasing environments with the transmission lengths bounded only by the resolution of SLMs. With proper probability amplitudes, reverse decoherence can also be understood in terms of hybrid entanglement and hidden nonlocality. Here, the initial state of the total system is hybrid-entangled, while the hidden nonlocality is activated later by local dephasing. When applied in noisy quantum teleportation, we achieved high fidelities even without the resource qubits being entangled. How-

ever, there still needs to be hybrid entanglement in the total auxiliary system. The experimental results obtained with a PM fiber imply that reverse decoherence could be used in practical optical fiber networks. It remains to be shown whether decoherence can be reversed with other channels and physical qubits. And what if the channel is completely unknown? In fact, an efficient entanglement-distillation protocol under any local noise was recently proposed in Ref. [135], while rewinding unknown unitary dynamics in the linear optical setting was demonstrated in [140].

In Chapter 5, we increased the environment of polarization by including the photons' path to it. Here, from the point of view of the open-system dynamics following what we call "open system interferometers" in Publications **III**–**V**, reservoir engineering essentially means controlling the prior durations of dephasing and free evolution, as well as choosing whether to measure the photons' path or not. We analyzed in great detail the MZ and HOM interferometers. In all cases, it was found that the path difference can be compensated with dephasing appearing after the interferometers—either partially (single-qubit case) or completely (certain two-qubit cases). Consequently, the path difference (and initial frequency correlations in the two-qubit case) can be estimated by monitoring the open-system dynamics. Importantly, this works outside the interferometric regions, and with the open system HOM interferometer due to the photodetector's dead time. Here, only the optimal case was considered, while in reality the weights of the c- and b-photons might not be that. Future research should formalize the theory of dead-time filtering more rigorously and test it experimentally. Perhaps the real weights could be probed with the probing protocol of Chapter 6. With the open system HOM interferometer, also a new kind of delayed-choice quantum eraser was proposed. The dynamical delayed-choice quantum eraser is based on the c- and b-photons undergoing dephasing differently, which raises the question: What other differences are there between the two types of photons?

With the open system MZ interferometer, we also considered parameter estimation in the interferometric region. Here, we analyzed the memory effects' sensitivity with respect to the path difference. The simulations show that, by monitoring pathwise dephasing, one can detect orders of magnitude smaller changes in the path difference than by comparing pathwise photon counts. With a small enough number of independent measurements and little "real" noise, we should even be able to break the QCRB. Finally, with the open system MZ interferometer, we also discussed non-Markovianity in the less studied CPTNI case. Here, losses are taken into account.

As the two quite simple interferometers considered in this Thesis already produce rich features of open-system dynamics that can be used in various tasks, it would be very interesting to extend the research to other interferometers (e.g., the *Sagnac interferometer* [141]) and initial states (e.g., the GHZ state). Other directions of future research include the generalization of the collision model with alternating continuous-time and discrete-time dynamics. Here, we only considered the first one or two collisions. In the generalized case, also more than one of the photons' paths

could be blocked. Furthermore, future studies show if open system interferometers can help with the problems of LOQC, e.g., by granting more control over the photonic logic gates.

Finally, in Chapter 6, we considered quantum probing with an unknown system-probe coupling. In the probing protocol, reservoir engineering shows as us changing some accessible control parameter. Evaluating the initial and evolved probe states' α-fidelities or trace distances corresponding to the different values of the control parameter, we can deduce something about a system of interest. In the two photonic examples originally demonstrated in Publications **VI** and **VII**, polarization and frequency played the roles of probe and system, respectively. First, we probed the width of a Gaussian spectrum with the control parameter being the spectrum's central frequency. Then, we probed the convex coefficient of a double-peaked Gaussian spectrum with the control parameter being the convex coefficient itself. As an application of the two examples, we showed how to verify the global non-Markovianity and Markovian/non-Markovian time intervals of the probe dynamics at a single, unknown point of interaction time.

Some questions regarding our probing protocol were left open. First, how could the bounds be optimized? Could we, for example, use more than one control parameter? Could some other measure result in tighter bounds than α-fidelity and trace distance? Could the bounds—whenever we get both a lower and an upper bound—even be equal? Furthermore, as we only considered the single-qubit case, increasing the number of qubits would be a natural next step. Could entanglement, for example, provide tighter bounds? Or conversely, could we probe the degree of entanglement? Finally, could we drop the assumption on the system's probability distribution?

Throughout this Thesis, we only considered dephasing with respect to the z-axis, i.e., the decay of coherences in the computational basis. While different dephasing directions are handled similarly locally, it would be very interesting to see how they combine nonlocally and what role initial correlations have in such cases. It would then be quite straightforward to generalize these results, as opposed to some of the very specific methods of decoherence control presented in this Thesis. The photonic model could also be expanded by still taking other degrees of freedom into account, e.g., orbital angular momentum (OAM). Finally, we hope this Thesis motivates the study of quantum processes as information carriers. To clarify, we do not mean the states going through the processes, but the overarching processes themselves. Future research topics in this field include, e.g., dynamical counterparts of the Holevo's theorem and QCRB. In the second task, a good starting point might be process positive operator-valued measures (PPOVMs [142]).

Bibliography

[1] J. Matson. What is quantum mechanics good for? *Scientific American*, 2010.

[2] A. Abbott. Quantum computers to explore precision oncology. *Nat. Biotechnol.*, 39(1324), 2021.

[3] E. Romero, R. Augulis, V. I. Novoderezhkin, M. Ferretti, J. Thieme, D. Zigmantas, and R. van Grondelle. Quantum coherence in photosynthesis for efficient solar-energy conversion. *Nat. Phys.*, 10(676), 2014.

[4] F. Arute *et al.* Quantum supremacy using a programmable superconducting processor. *Nature*, 574(505), 2019.

[5] W. H. Zurek. Decoherence, einselection, and the quantum origins of the classical. *Rev. Mod. Phys.*, 75(715), 2003.

[6] H.-P. Breuer and F. Petruccione. *The Theory of Open Quantum Systems*. Oxford University Press, Oxford, 2007.

[7] Á. Rivas and S. F. Huelga. *Open Quantum Systems: An Introduction*. Springer, Heidelberg, 2012.

[8] S. Banerjee. *Open Quantum Systems: Dynamics of Nonclassical Evolution*. Springer, Singapore, 2018.

[9] D. Suter and G. A. Álvarez. *Colloquium*: Protecting quantum information against environmental noise. *Rev. Mod. Phys.*, 88(041001), 2016.

[10] Y. Dong, Y. Zheng, S. Li, C.-C. Li, X.-D. Chen, G.-C. Guo, and F.-W. Sun. Non-Markovianity-assisted high-fidelity Deutsch–Jozsa algorithm in diamond. *npj Quantum Inf.*, 4(3), 2018.

[11] Q. Yao, J. Zhang, X.-F. Yi, L. You, and W. Zhang. Uniaxial dynamical decoupling for an open quantum system. *Phys. Rev. Lett.*, 122(010408), 2019.

[12] A. M. Souza. Process tomography of robust dynamical decoupling with superconducting qubits. *Quantum Inf. Process.*, 20(237), 2021.

[13] P. Kwiat, A. Berglund, J. Altepeter, and A. White. Experimental verification of decoherence-free subspaces. *Science*, 290(5491), 2000.

[14] J. B. Altepeter, P. G. Hadley, S. M. Wendelken, A. J. Berglund, and P. G. Kwiat. Experimental investigation of a two-qubit decoherence-free subspace. *Phys. Rev. Lett.*, 92(147901), 2004.

[15] D. A. Lidar. Review of decoherence-free subspaces, noiseless subsystems, and dynamical decoupling. *Adv. Chem. Phys.*, 154(295), 2014.

[16] K. Sinha, P. Meystre, E. A. Goldschmidt, F. K. Fatemi, S. L. Rolston, and P. Solano. Non-Markovian collective emission from macroscopically separated emitters. *Phys. Rev. Lett.*, 124 (043603), 2020.

[17] A. Carmele, N. Nemet, V. Canela, and S. Parkins. Pronounced non-Markovian features in multiply excited, multiple emitter waveguide QED: Retardation induced anomalous population trapping. *Phys. Rev. Res.*, 2(013238), 2020.

[18] S. Lorenzo, S. Longhi, A. Cabot, R. Zambrini, and G. L. Giorgi. Intermittent decoherence blockade in a chiral ring environment. *Sci. Rep.*, 11(12834), 2021.

[19] Y. Peng and H. Fan. Achieving the Heisenberg limit under general Markovian noise using quantum error correction without ancilla. *Quantum Inf. Process.*, 19(266), 2020.

[20] A. E. Seedhouse, T. Tanttu, R. C. C. Leon, R. Zhao, K. Y. Tan, B. Hensen, F. E. Hudson, K. M. Itoh, J. Yoneda, C. H. Yang, A. Morello, A. Laucht, S. N. Coppersmith, A. Saraiva, and

A. S. Dzurak. Pauli blockade in silicon quantum dots with spin-orbit control. *PRX Quantum*, 2 (010303), 2021.

[21] P. Parrado-Rodríguez, C. Ryan-Anderson, A. Bermudez, and M. Müller. Crosstalk suppression for fault-tolerant quantum error correction with trapped ions. *Quantum*, 5(487), 2021.

[22] D. Ebler, S. Salek, and G. Chiribella. Enhanced communication with the assistance of indefinite causal order. *Phys. Rev. Lett.*, 120(120502), 2018.

[23] Y. Guo, X.-M. Hu, Z.-B. Hou, H. Cao, J.-M. Cui, B.-H. Liu, Y.-F. Huang, C.-F. Li, G.-C. Guo, and G. Chiribella. Experimental transmission of quantum information using a superposition of causal orders. *Phys. Rev. Lett.*, 124(030502), 2020.

[24] B. J. Dalton, S. M. Barnett, and B. M. Garraway. Theory of pseudomodes in quantum optical processes. *Phys. Rev. A*, 64(053813), 2001.

[25] Y. Maleki and B. Ahansaz. Maximal-steered-coherence protection by quantum reservoir engineering. *Phys. Rev. A*, 102(020402(R)), 2020.

[26] R. Stárek, M. Mičuda, I. Straka, M. Nováková, M. Dušek, M. Ježek, J. Fiurášek, and R. Filip. Experimental quantum decoherence control by dark states of the environment. *New J. Phys.*, 22 (093058), 2020.

[27] W. Wu and Z.-Z. Zhang. Controllable dynamics of a dissipative two-level system. *Sci. Rep.*, 11 (7188), 2021.

[28] H. Lyyra. *Controlling dynamics of open quantum systems*. University of Turku, Department of Physics and Astronomy, 2019.

[29] H.-P. Breuer, E.-M. Laine, J. Piilo, and B. Vacchini. *Colloquium*: Non-Markovian dynamics in open quantum systems. *Rev. Mod. Phys.*, 88(021002), 2016.

[30] I. de Vega and D. Alonso. Dynamics of non-Markovian open quantum systems. *Rev. Mod. Phys.*, 89(015001), 2017.

[31] L. Li, M. J. W. Hall, and H. M. Wiseman. Concepts of quantum non-Markovianity: A hierarchy. *Phys. Rep.*, 759(1), 2018.

[32] C.-F. Li, G.-C. Guo, and J. Piilo. Non-Markovian quantum dynamics: What does it mean? *Europhys. Lett.*, 127(5), 2019.

[33] C.-F. Li, G.-C. Guo, and J. Piilo. Non-Markovian quantum dynamics: What is it good for? *Europhys. Lett.*, 128(3), 2019.

[34] J.-S. Xu, C.-F. Li, X.-Y. Xu, C.-H. Shi, X.-B. Zou, and G.-C. Guo. Experimental characterization of entanglement dynamics in noisy channels. *Phys. Rev. Lett.*, 103(240502), 2009.

[35] X.-Y. Xu, J.-S. Xu, C.-F. Li, and G.-C. Guo. Measurement-induced quantum entanglement recovery. *Phys. Rev. A*, 82(022324), 2010.

[36] J.-S. Xu, C.-F. Li, C.-J. Zhang, X.-Y. Xu, Y.-S. Zhang, and G.-C. Guo. Experimental investigation of the non-Markovian dynamics of classical and quantum correlations. *Phys. Rev. A*, 82 (042328), 2010.

[37] J.-S. Xu, X.-Y. Xu, C.-F. Li, C.-J. Zhang, X.-B. Zou, and G.-C. Guo. Experimental investigation of classical and quantum correlations under decoherence. *Nat. Commun.*, 1(7), 2010.

[38] A. Shaham and H. S. Eisenberg. Realizing controllable depolarization in photonic quantum-information channels. *Phys. Rev. A*, 83(022303), 2011.

[39] A. Shaham and H. S. Eisenberg. Realizing a variable isotropic depolarizer. *Opt. Lett.*, 37(13), 2012.

[40] E.-M. Laine, H.-P. Breuer, J. Piilo, C.-F. Li, and G.-C. Guo. Nonlocal memory effects in the dynamics of open quantum systems. *Phys. Rev. Lett.*, 108(210402), 2012.

[41] B.-H. Liu, D.-Y. Cao, Y.-F. Huang, C.-F. Li, G.-C. Guo, E.-M. Laine, H.-P. Breuer, and J. Piilo. Photonic realization of nonlocal memory effects and non-Markovian quantum probes. *Sci. Rep.*, 3(1781), 2013.

[42] A. Shaham and H. S. Eisenberg. Effect of decoherence on the contextual and nonlocal properties of a biphoton. *Phys. Rev. A*, 91(022123), 2015.

[43] S. Hamedani Raja, G. Karpat, E.-M. Laine, S. Maniscalco, J. Piilo, C.-F. Li, and G.-C. Guo. Remote polarization-entanglement generation by local dephasing and frequency up-conversion. *Phys. Rev. A*, 96(013844), 2017.

[44] S. Hamedani Raja, K. P. Athulya, A. Shaji, and J. Piilo. Photonic dephasing dynamics and the role of initial correlations. *Phys. Rev. A*, 101(042127), 2020.

[45] G. M. Palma, K.-A. Suominen, and A. K. Ekert. Quantum computers and dissipation. *Proc. Roy. Soc. Lond. A*, 452(567), 1996.

[46] B.-H. Liu, L. Li, Y.-F. Huang, C.-F. Li, G.-C. Guo, E.-M. Laine, H.-P. Breuer, and J. Piilo. Experimental control of the transition from Markovian to non-Markovian dynamics of open quantum systems. *Nat. Phys.*, 7(931), 2011.

[47] Z.-D. Liu, H. Lyyra, Y.-N. Sun, B.-H. Liu, C.-F. Li, G.-C. Guo, S. Maniscalco, and J. Piilo. Experimental implementation of fully controlled dephasing dynamics and synthetic spectral densities. *Nat. Commun.*, 9(3453), 2018.

[48] E.-M. Laine, H.-P. Breuer, and J. Piilo. Nonlocal memory effects allow perfect teleportation with mixed states. *Sci. Rep.*, 4(4620), 2014.

[49] Z.-D. Liu, Y.-N. Sun, B.-H. Liu, C.-F. Li, G.-C. Guo, S. Hamedani Raja, H. Lyyra, and J. Piilo. Experimental realization of high-fidelity teleportation via a non-Markovian open quantum system. *Phys. Rev. A*, 102(062208), 2020.

[50] B.-H. Liu, X.-M. Hu, Y.-F. Huang, C.-F. Li, G.-C. Guo, A. Karlsson, E.-M. Laine, S. Maniscalco, C. Macchiavello, and J. Piilo. Efficient superdense coding in the presence of non-Markovian noise. *Europhys. Lett.*, 114(10005), 2016.

[51] A. Karlsson, H. Lyyra, E.-M. Laine, S. Maniscalco, and J. Piilo. Non-Markovian dynamics in two-qubit dephasing channels with an application to superdense coding. *Phys. Rev. A*, 93 (032135), 2016.

[52] A. Salles, F. de Melo, M. P. Almeida, M. Hor-Meyll, S. P. Walborn, P. H. Souto Ribeiro, and L. Davidovich. Experimental investigation of the dynamics of entanglement: Sudden death, complementarity, and continuous monitoring of the environment. *Phys. Rev. A*, 78(022322), 2008.

[53] A. Chiuri, C. Greganti, L. Mazzola, M. Paternostro, and P. Mataloni. Linear optics simulation of quantum non-Markovian dynamics. *Sci. Rep.*, 2(968), 2012.

[54] F. F. Fanchini, G. Karpat, B. Çakmak, L. K. Castelano, G. H. Aguilar, O. Jiménez Farías, S. P. Walborn, P. H. S. Ribeiro, and M. C. de Oliveira. Non-Markovianity through accessible information. *Phys. Rev. Lett.*, 112(210402), 2014.

[55] S. Cialdi, M. A. C. Rossi, C. Benedetti, B. Vacchini, D. Tamascelli, S. Olivares, and M. G. A. Paris. All-optical quantum simulator of qubit noisy channels. *Appl. Phys. Lett.*, 110(081107), 2017.

[56] S. A. Uriri, F. Wudarski, I. Sinayskiy, F. Petruccione, and M. S. Tame. Experimental investigation of Markovian and non-Markovian channel addition. *Phys. Rev. A*, 101(052107), 2020.

[57] N. K. Bernardes, A. R. R. Carvalho, C. H. Monken, and M. F. Santos. Environmental correlations and Markovian to non-Markovian transitions in collisional models. *Phys. Rev. A*, 90(032111), 2014.

[58] J. Jin, V. Giovannetti, R. Fazio, F. Sciarrino, P. Mataloni, A. Crespi, and R. Osellame. All-optical non-Markovian stroboscopic quantum simulator. *Phys. Rev. A*, 91(012122), 2015.

[59] Á. Cuevas, A. Geraldi, C. Liorni, L. D. Bonavena, A. De Pasquale, F. Sciarrino, V. Giovannetti, and P. Mataloni. All-optical implementation of collision-based evolutions of open quantum systems. *Sci. Rep.*, 9(3205), 2019.

[60] L. Zehnder. Ein neuer interferenzrefraktor. *Z. Instrumkde*, 11(275), 1891.

[61] L. Mach. Ueber einen interferenzrefraktor. *Z. Instrumkde*, 12(89), 1892.

[62] S. Ataman, A. Preda, and R. Ionicioiu. Phase sensitivity of a Mach-Zehnder interferometer with single-intensity and difference-intensity detection. *Phys. Rev. A*, 98(043856), 2018.

[63] C. K. Hong, Z. Y. Ou, and L. Mandel. Measurement of subpicosecond time intervals between two photons by interference. *Phys. Rev. Lett.*, 59(2044), 1987.

[64] F. Bouchard, A. Sit, Y. Zhang, R. Fickler, F. M. Miatto, Y. Yao, F. Sciarrino, and E. Karimi. Two-photon interference: the Hong-Ou-Mandel effect. *Rep. Prog. Phys.*, 84(012402), 2020.

[65] C. Helstrom. Minimum mean-squared error of estimates in quantum statistics. *Phys. Lett. A*, 25 (101), 1967.

[66] M. G. A. Paris. Quantum estimation for quantum technology. *Int. J. Quantum Inf.*, 7(125), 2009.

[67] M. Tukiainen, H. Lyyra, G. Sarbicki, and S. Maniscalco. Fidelity of dynamical maps. *Phys. Rev. A*, 95(052102), 2017.

[68] M. Tukiainen. *Implementability of Observables, Channels and Instruments in Quantum Theory of Measurements*. University of Turku, Department of Physics and Astronomy, 2017.

[69] T. Heinosaari and M. Ziman. *The Mathematical Language of Quantum Theory*. Cambridge University Press, Cambridge, 2012.

[70] M. Nielsen and I. Chuang. *Quantum Computation and Quantum Information*. Cambridge University Press, Cambridge, 2000.

[71] C. H. Bennett and G. Brassard. Quantum cryptography: Public key distribution and coin tossing. *Proc. IEEE Int. Conf. on Computers, Systems, and Signal Processing*, 175(8), 1984.

[72] V. Giovannetti, S. Lloyd, and L. Maccone. Advances in quantum metrology. *Nat. Photon.*, 5 (222), 2011.

[73] C. H. Bennett, G. Brassard, C. Crépeau, R. Jozsa, A. Peres, and W. K. Wootters. Teleporting an unknown quantum state via dual classical and Einstein-Podolsky-Rosen channels. *Phys. Rev. Lett.*, 70(1895), 1993.

[74] P. Rungta, V. Bužek, C. M. Caves, M. Hillery, and G. J. Milburn. Universal state inversion and concurrence in arbitrary dimensions. *Phys. Rev. A*, 64(042315), 2001.

[75] C. H. Bennett, G. Brassard, and N. D. Mermin. Quantum cryptography without Bell's theorem. *Phys. Rev. Lett.*, 68(557), 1992.

[76] C. A. Fuchs and A. Peres. Quantum-state disturbance versus information gain: Uncertainty relations for quantum information. *Phys. Rev. A*, 53(2038), 1996.

[77] L. Maccone. Information-disturbance tradeoff in quantum measurements. *Phys. Rev. A*, 73 (042307), 2006.

[78] J. von Neumann. *Mathematical Foundations of Quantum Mechanics*. Princeton University Press, Princeton, 1955.

[79] J.-P. Pellonpää, K. Ylinen, P. Busch, and P. J. Lahti. *Quantum Measurement*. Springer, Switzerland, 2016.

[80] H. P. Stapp. The Copenhagen interpretation. *J. Mind Behav.*, 18(2–3), 1997.

[81] J. Söderholm, G. Björk, A. B. Klimov, L. L. Sánchez-Soto, and G. Leuchs. Quantum polarization characterization and tomography. *New J. Phys.*, 14(115014), 2012.

[82] K. Srinivasan and G. Raghavan. Stokes vector and its relationship to discrete Wigner functions of multiqubit states. *Phys. Lett. A*, 380(33), 2016.

[83] P. G. Kwiat, K. Mattle, H. Weinfurter, A. Zeilinger, A. V. Sergienko, and Y. Shih. New high-intensity source of polarization-entangled photon pairs. *Phys. Rev. Lett.*, 75(4337), 1995.

[84] N. Gisin, G. Ribordy, W. Tittel, and H. Zbinden. Quantum cryptography. *Rev. Mod. Phys.*, 74 (145), 2002.

[85] L. Susskind and A. Friedman. *Quantum Mechanics: The Theoretical Minimum*. Penguin Books, London, 2015.

[86] M.-D. Choi. Completely positive linear maps on complex matrices. *Lin. Alg. Appl.*, 10(285), 1975.

[87] P. T. Cochrane, G. J. Milburn, and W. J. Munro. Macroscopically distinct quantum-superposition states as a bosonic code for amplitude damping. *Phys. Rev. A*, 59(2631), 1999.

[88] K. M. Fonseca Romero and R. Lo Franco. Simple non-Markovian microscopic models for the depolarizing channel of a single qubit. *Phys. Scr.*, 86(6), 2012.

[89] K. Kraus, A. Böhm, J. D. Dollard, and W. H. Wootters. *States, Effects and Operations: Fundamental Notions of Quantum Theory*. Springer Berlin, Heidelberg, 1983.

[90] H. T. Quan, Z. Song, X. F. Liu, P. Zanardi, and C. P. Sun. Decay of Loschmidt echo enhanced by quantum criticality. *Phys. Rev. Lett.*, 96(140604), 2006.

[91] X. Fan, T. Takagahara, J. E. Cunningham, and H. Wang. Pure dephasing induced by exciton–phonon interactions in narrow GaAs quantum wells. *Solid State Commun.*, 108(857), 1998.

[92] Ł. Cywiński, R. M. Lutchyn, C. P. Nave, and S. Das Sarma. How to enhance dephasing time in superconducting qubits. *Phys. Rev. B*, 77(174509), 2008.

[93] I. Pikovski, M. Zych, F. Costa, and Č. Brukner. Universal decoherence due to gravitational time dilation. *Nat. Phys.*, 11(668), 2015.

[94] M. Bramberger and I. de Vega. Dephasing dynamics of an impurity coupled to an anharmonic environment. *Phys. Rev. A*, 101(012101), 2020.

[95] F. Caleffi, M. Capone, I. de Vega, and A. Recati. Impurity dephasing in a Bose–Hubbard model. *New J. Phys.*, 23(033018), 2021.

[96] W. Sellmeier. Ueber die durch die aetherschwingungen erregten mitschwingungen der körpertheilchen und deren rückwirkung auf die ersteren, besonders zur erklärung der dispersion und ihrer anomalien (II. theil). *Ann. Phys. Chem.*, 223(11), 1872.

[97] G. Ghosh. Dispersion-equation coefficients for the refractive index and birefringence of calcite and quartz crystals. *Opt. Commun.*, 163(95), 1999.

[98] D. M. Greenberger, M. A. Horne, and A. Zeilinger. Going beyond Bell's theorem. *In: "Bell's Theorem, Quantum Theory, and Conceptions of the Universe", M. Kafatos (Ed.), Kluwer, Dordrecht*, 1989.

[99] R.-B. Jin, T. Saito, and R. Shimizu. Time-frequency duality of biphotons for quantum optical synthesis. *Phys. Rev. Appl.*, 10(034011), 2018.

[100] G. A. Paz-Silva, M. J. W. Hall, and H. M. Wiseman. Dynamics of initially correlated open quantum systems: Theory and applications. *Phys. Rev. A*, 100(042120), 2019.

[101] P. Kok, W. J. Munro, K. Nemoto, T. C. Ralph, J. P. Dowling, and G. J. Milburn. Linear optical quantum computing with photonic qubits. *Rev. Mod. Phys.*, 79(135), 2007.

[102] Á. Rivas, S. F. Huelga, and M. B. Plenio. Quantum non-Markovianity: characterization, quantification and detection. *Rep. Prog. Phys.*, 77(094001), 2014.

[103] H.-P. Breuer, E.-M. Laine, and J. Piilo. Measure for the degree of non-Markovian behavior of quantum processes in open systems. *Phys. Rev. Lett.*, 103(210401), 2009.

[104] N. Megier, D. Chruściński, J. Piilo, and W. T. Strunz. Eternal non-Markovianity: from random unitary to Markov chain realisations. *Sci. Rep.*, 7(6379), 2017.

[105] J. Teittinen, H. Lyyra, B. Sokolov, and S. Maniscalco. Revealing memory effects in phase-covariant quantum master equations. *New J. Phys.*, 20(073012), 2018.

[106] F. A. Pollock, C. Rodríguez-Rosario, T. Frauenheim, M. Paternostro, and K. Modi. Operational Markov condition for quantum processes. *Phys. Rev. Lett.*, 120(040405), 2018.

[107] A. A. Budini. Quantum non-Markovian processes break conditional past-future independence. *Phys. Rev. Lett.*, 121(240401), 2018.

[108] S. Milz, M. S. Kim, F. A. Pollock, and K. Modi. Completely positive divisibility does not mean Markovianity. *Phys. Rev. Lett.*, 123(040401), 2019.

[109] A. A. Budini. Conditional past-future correlation induced by non-Markovian dephasing reservoirs. *Phys. Rev. A*, 99(052125), 2019.

[110] S. Yu, A. A. Budini, Y.-T. Wang, Z.-J. Ke, Y. Meng, W. Liu, Z.-P. Li, Q. Li, Z.-H. Liu, J.-S. Xu, J.-S. Tang, C.-F. Li, and G.-C. Guo. Experimental observation of conditional past-future correlations. *Phys. Rev. A*, 100(050301(R)), 2019.

[111] T. de Lima Silva, S. P. Walborn, M. F. Santos, G. H. Aguilar, and A. A. Budini. Detection of quantum non-Markovianity close to the Born-Markov approximation. *Phys. Rev. A*, 101 (042120), 2020.

[112] M. J. W. Hall, J. D. Cresser, L. Li, and E. Andersson. Canonical form of master equations and characterization of non-Markovianity. *Phys. Rev. A*, 89(042120), 2014.

[113] S. Utagi, R. Srikanth, and S. Banerjee. Ping-pong quantum key distribution with trusted noise: non-Markovian advantage. *Quantum Inf. Process.*, 19(366), 2020.

[114] T. S. Humble and W. P. Grice. Spectral effects in quantum teleportation. *Phys. Rev. A*, 75 (022307), 2007.

[115] T. S. Humble and W. P. Grice. Effects of spectral entanglement in polarization-entanglement swapping and type-I fusion gates. *Phys. Rev. A*, 77(022312), 2008.

[116] G.-Y. Xiang, Z.-B. Hou, C.-F. Li, G.-C. Guo, H.-P. Breuer, E.-M. Laine, and J. Piilo. Entanglement distribution in optical fibers assisted by nonlocal memory effects. *Europhys. Lett.*, 107 (54006), 2014.

[117] F. Laudenbach, H. Hübel, M. Hentschel, P. Walther, and A. Poppe. Modelling parametric down-conversion yielding spectrally pure photon pairs. *Opt. Express*, 24(2712), 2016.

[118] V. Giovannetti, L. Maccone, J. H. Shapiro, and F. N. C. Wong. Generating entangled two-photon states with coincident frequencies. *Phys. Rev. Lett.*, 88(183602), 2002.

[119] K. Huang, H. Le Jeannic, O. Morin, T. Darras, G. Guccione, A. Cavaillès, and J. Laurat. Engineering optical hybrid entanglement between discrete- and continuous-variable states. *New J. Phys.*, 21(083033), 2019.

[120] H. Atmanspacher. Cartesian cut, Heisenberg cut, and the concept of complexity. *World Futures*, 49(333), 1997.

[121] T. Yu and J. H. Eberly. Evolution from entanglement to decoherence of bipartite mixed "X" states. *Quantum Inf. Comput.*, 7(459), 2007.

[122] A. Imamoglu. Stochastic wave-function approach to non-Markovian systems. *Phys. Rev. A*, 50 (3650), 1994.

[123] R. Martinazzo, B. Vacchini, K. H. Hughes, and I. Burghardt. Communication: Universal Markovian reduction of Brownian particle dynamics. *J. Chem. Phys.*, 134(011101), 2011.

[124] S. Popescu. Bell's inequalities and density matrices: Revealing "hidden" nonlocality. *Phys. Rev. Lett.*, 74(2619), 1995.

[125] N. Gisin. Hidden quantum nonlocality revealed by local filters. *Phys. Lett. A*, 210(151), 1996.

[126] P. G. Kwiat, S. Barraza-Lopez, A. Stefanov, and N. Gisin. Experimental entanglement distillation and 'hidden' non-locality. *Nature*, 409(1014), 2001.

[127] J.-Y. Li, X.-X. Fang, T. Zhang, G. N. M. Tabia, H. Lu, and Y.-C. Liang. Activating hidden teleportation power: Theory and experiment. *Phys. Rev. Res.*, 3(023045), 2021.

[128] R. Jozsa. Fidelity for mixed quantum states. *J. Mod. Opt.*, 41(2315), 1994.

[129] S. Massar and S. Popescu. Optimal extraction of information from finite quantum ensembles. *Phys. Rev. Lett.*, 74(1259), 1995.

[130] L. Seveso, M. A. C. Rossi, and M. G. A. Paris. Quantum metrology beyond the quantum Cramér-Rao theorem. *Phys. Rev. A*, 95(012111), 2017.

[131] R.-B. Jin, G.-Q. Chen, H. Jing, C. Ren, P. Zhao, R. Shimizu, and P.-X. Lu. Monotonic quantum-to-classical transition enabled by positively correlated biphotons. *Phys. Rev. A*, 95(062341), 2017.

[132] W. Tittel and G. Weihs. Photonic entanglement for fundamental tests and quantum communication. *Quantum Inf. Comput.*, 1(3), 2001.

[133] P. G. Kwiat, A. M. Steinberg, and R. Y. Chiao. Observation of a "quantum eraser": A revival of coherence in a two-photon interference experiment. *Phys. Rev. A*, 45(7729), 1992.

[134] S. M. Barnett. *Quantum Information*. Oxford University Press, Oxford, 2009.

[135] M. Piccolini, V. Giovannetti, and R. Lo Franco. Asymptotically-deterministic robust preparation of maximally entangled bosonic states. *arXiv:2303.11484 [quant-ph]*, 2023.

[136] M. Bruderer and D. Jaksch. Probing BEC phase fluctuations with atomic quantum dots. *New J. Phys.*, 8(87), 2006.

[137] P. Haikka, S. McEndoo, and S. Maniscalco. Non-Markovian probes in ultracold gases. *Phys. Rev. A*, 87(012127), 2013.

[138] R. Dorner, S. R. Clark, L. Heaney, R. Fazio, J. Goold, and V. Vedral. Extracting quantum work statistics and fluctuation theorems by single-qubit interferometry. *Phys. Rev. Lett.*, 110(230601), 2013.

[139] D. Girolami, A. M. Souza, V. Giovannetti, T. Tufarelli, J. G. Filgueiras, R. S. Sarthour, D. O. Soares-Pinto, I. S. Oliveira, and G. Adesso. Quantum discord determines the interferometric power of quantum states. *Phys. Rev. Lett.*, 112(210401), 2014.

[140] P. Schiansky, T. Strömberg, D. Trillo, V. Saggio, B. Dive, M. Navascués, and P. Walther. Demonstration of universal time-reversal for qubit processes. *Optica*, 10(200), 2023.

[141] G. Sagnac. L'éther lumineux démontré par l'effet du vent relatif d'éther dans un interféromètre en rotation uniforme. *Comptes Rendus*, 157(708), 1913.

[142] M. Ziman. Process positive-operator-valued measure: A mathematical framework for the description of process tomography experiments. *Phys. Rev. A*, 77(062112), 2008.

TURUN
YLIOPISTO
UNIVERSITY
OF TURKU

Painosalama Oy, Turku, Finland 2023

ISBN 978-951-29-9281-2 (PRINT)
ISBN 978-951-29-9282-9 (PDF)
ISSN 0082-7002 (PRINT)
ISSN 2343-3175 (ONLINE)